Quantum Mechanical Studies of the Early Actinide Compounds

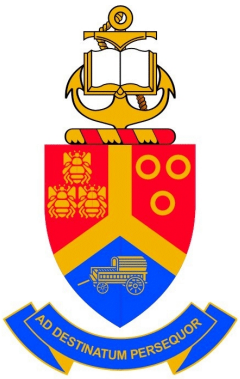

by

Kingsley Onyebuchi Obodo

Submitted in partial fulfilment of the requirements
for the degree
PhilosophiæDoctor (PhD)
in the Department of Physics
Faculty of Natural and Agricultural Sciences
University of Pretoria

Supervisor: Prof. Nithaya Chetty

February 17, 2014

UNIVERSITEIT VAN PRETORIA
UNIVERSITY OF PRETORIA
YUNIBESITHI YA PRETORIA

UNIVERSITY OF PRETORIA

DECLARATION OF ORIGINALTY

This document must be signed and submitted with every essay, report, project, assignment, dissertation and/or thesis.

Full names of student: Obodo, Kingsley Onyebuchi

Student number: s11285266

Declaration

1. I understand what plagiarism is and am aware of the University's policy in this regard.
2. I declare that this thesis is my own original work. Where other people's work has been used (either from a printed source, Internet or any other source), this has been properly acknowledged and referenced in accordance with departmental requirements.
3. I have not used work previously produced by another student or any other person to hand in as my own.
4. I have not allowed, and will not allow, anyone to copy my work with the intention of passing it off as his or her own.

SIGNATURE STUDENT:.....

DATE:.....

Abstract

This study involves the investigation of the early actinide systems using *ab initio* techniques based on density functional theory (DFT). It was motivated by: (i) the incomplete description of these systems using conventional DFT because they are strongly correlated, (ii) the usefulness of these systems in nuclear energy generation, (iii) the complexity that arises in experimentally studying these systems due to their inherent radioactive nature and (iv) their limited availability.

The results obtained from this study are divided into two broad sections. The first comprises chapters 3 and 4 while the second comprises chapters 5 and 6. Thorium based compounds are studied in chapters 3 and 4. In the first section, the Hubbard U parameter is not necessary to accurately describe the electronic, elastic and mechanical properties of these systems. In the second, the inclusion of the Hubbard U parameter is shown to be paramount for the accurate description of most compounds considered.

Chapter 3 presents the electronic, structural and bonding character of thorium based nitrides. We obtained the result that Th_2N_2NH, which is crystallographically equivalent to metallic Th_2N_3, is insulating. Chapter 4 demonstrates that the formation of a meta-stable thorium-titanium based alloy is plausible and also further information on bonding, electronic and elastic properties of the determined meta-stable alloy is provided. This has provided important new knowledge about these bulk systems.

In Chapter 5 the DFT + U based study on Pa and its oxides is presented. The electronic, structural and bonding character of these systems was studied. We found that PaO_2 is a Mott-Hubbard insulator with an indirect band gap of 3.48 eV within the generalized gradient approximation GGA + U. Chapter 6 discusses various actinide nitrides. We explored the electronic properties, elastic properties, lattice dynamics and the energetics of the various compounds using GGA + U. Also, we

investigated the effect of the Hubbard U parameter and magnetic configuration on these systems.

The use of the DFT + U based method provides a rapid way to study strongly correlated systems, while other methods such as Hybrid functional, GW, DMFT+DFT, etc. are highly intensive, computationally speaking. Finally, the results obtained with the inclusion of this *ad hoc* parameter give a very good description of these systems.

I would like to dedicate this thesis to my family for all they have done, provided and put up with to help me achieve this extraordinary milestone in my life.

Acknowledgements

I would like to acknowledge the University of Pretoria for funding, members of the computational and theoretical physics group at the department of Physics for useful discussions, my supervisor for his guidance, and my friends and loved ones for their general support. Lastly, I am grateful to my family for their unwavering support and prayers.

Contents

List of Figures

List of Tables

Acronyms

AE all-electron. 21, 23

BOA Born-Oppenheimer Approximation. 8, 30

BZ Brillouin zone. 19, 24, 25

DFT Density Functional Theory. 2, 4, 5, 7, 11, 13, 20, 39, 45, 119, 120

DFT+U DFT plus the Hubbard *U* Correction. 5, 7, 34, 119–122

FFT fast Fourier transform. 17

GGA Generalized Gradient Approximation. 3, 4, 16, 17, 32

GGA+U GGA plus the Hubbard *U* Correction. 4

HF Hartree-Fock approximation. 9–11

KS Kohn-Sham. 13–15, 17–19, 24, 27, 34

LDA+U LDA plus the Hubbard *U* Correction. 4, 34–36, 38, 39

LSDA Local Spin Density Approximation. 4, 15–17, 32, 35

MP Methfessel-Paxton. 25, 26

OPW Orthogonalized Plane Wave. 20, 22

PAW projector augmented wave. 21–23, 39

PBE Perdew-Burke-Ernzerhof. 3, 4

SCF Self-Consistent Field. 18

XC exchange-correlation. 14–17, 32

Chapter 1

Introduction

1.1 Actinide systems

The actinides can be divided into two sub-series: the early (Th-Pu) and the late (Am-Lr).[1] This is based on their position in the series and the different characteristics exhibited. The early actinides comprise the elements Thorium (Th 90), Protactinium (Pa 91), Uranium (U 92), Neptunium (Np 93) and Plutonium (Pu 94).

One of the major aspects of the importance of actinide compounds are their potential application in advanced fuel materials for fast breeder reactors. In particular, actinide nitrides are considered important as a source for nuclear fuel material in the proposed Generation IV nuclear power plants (future fast neutron fission reactors).[2;3;4;5;6;7;8;9;10] Also, actinide compounds find a use as target materials to transmute plutonium and minor actinides in fast reactor cores and in accelerator driven systems. The high density of the nitride fuel creates more excess neutrons and has a higher potential to transmute the long-lived fission products. If one considers the breeding ratio, appropriate thermophysical properties, high thermal conductivity, high melting point and fuel density, chemical compatibility with the Na coolant, and reprocessing feasibility, actinide nitrides appear to be a compromise between oxide and metal fuels.

The understanding of the early actinide compounds from both scientific and technological points of view is a very complex and challenging area of research.[11;12;13;14;15;16;17] The theoretical description of the early actinide compounds presents a considerable challenge due to the onset of 5*f*-electron localization phenomena. They contain a partially filled 5*f*-orbital that is spatially localized around the nucleus. The large number of electrons per atom in these strongly correlated compounds leads to various exotic properties such as half-metallicity,

metal-insulator transition, Mott insulators, high-Tc, heavy Fermion materials, etc. Noteworthy is a parabolic decrease of the volume as a function of the atomic number, which shows a similar trend to that of the transition metals. For the early actinides, this behavior is attributed to the nature of electron-electron interactions in the 5*f* compounds. However, for the transition metals, this behavior is attributed to the 3*d* electrons. Hence, the actinides are sometimes referred to as a form of the 5*f* transition series.[18]

The crossover of localization/delocalization influences the phase diagram of actinide compounds immensely. This can be seen in the difference between the electronic and magnetic properties of Uranium and Berkelium compounds.[19] The *f*-electron contribution to the chemical bonding character can be greatly influenced by a minimal change in the external or chemical pressure of the system. This results in a wide array of characteristics for the alloys and compounds of a given actinide element. It was suggested by Hill[11] that the actinide-actinide bond distance determines the extent of magnetic order through the control of the *f* - *f* overlap in actinide compounds. Various studies have shown that actinide compounds do not necessarily follow the systematics based solely on *f*-band formation. The *f*-*d* and *f*-*p* hybridizations are equally important in describing the electronic and magnetic properties of these compounds.

Electronic correlation, which is not considered in traditional density functional approximations or Hartree-Fock theory, treats the systems as non-interacting entities, which is the essential feature that defines these systems. To give a qualitative description of the early actinides (particularly Pa to Pu), going beyond standard Density Functional Theory (DFT) or Hartree-Fock theory, is consequently essential. Several methods such as the DFT + U,[20;21;22;23;24] SIC, GW, etc. as well as simplified model Hamiltonians (e.g Hubbard-like models) have been proposed to account for these.

This study focuses on the actinide compounds formed by these elements with nitrogen, oxygen and titanium.

1.2 Aims and objectives

This study is divided into two parts. The first comprises chapters 3 and 4, which focus on the Thorium based compounds. This part shows that such compounds do not need inclusion of the Hubbard U parameter for a proper description of these systems, in spite of their being early actinides. In the second section, which comprises chapters 5 and 6, the importance of the Hubbard U parameter is underscored for the proper description of these systems.

1.2.1 Thorium based alloys

The first part of this study demonstrates that the structural, elastic, and mechanical properties and the formation energy of the actinide compounds without the 5*f* electrons can be accurately determined without the inclusion of the Hubbard *U* parameter. This part is divided into two chapters.

Firstly, using a DFT approach within the Perdew-Burke-Ernzerhof (PBE) Generalized Gradient Approximation (GGA) [GGA (PBE)] implemented in the VASP codes, we investigate the structural, elastic and electronic properties of Th_3N_4, Th_2N_3 and $Th_2N_2(NH)$. The calculated structural properties of the nitrides are in good agreement with experimental data. We observed that all the Th-N based compounds considered are energetically favorable and elastically stable. We found that Th_3N_4 is semiconducting with a band gap of 1.59 eV, which compares well with the experimental band gap of 1.7 eV, while Th_2N_3 is metallic. $Th_2N_2(NH)$, which is crystallographically equivalent to Th_2N_3 is insulating with a band gap of 2.12 eV. This is due to the -(NH) group that results in the shifting of the energy bands consequently opening up a gap at the Fermi-level. We observe that all the investigated Th-N based compounds are predominantly ionic.[25]

Secondly, using a quantum chemical method, we investigate the dearth of ordered alloys involving thorium and titanium. Based on the fact that both these elements are known to alloy very readily with various other elements, for example with oxygen, nitrogen and carbon current experimental data suggests that Th and Ti do not alloy very readily with each other. This study explored the possibility of the formation of a stoichiometry compound involving these elements by considering a variety of ordered alloys of ThTi based compounds. By probing the energetics, electronic, phonon and elastic properties of these systems, we confirm the scarcity of ordered alloys involving Th and Ti, since for a variety of reasons many of the systems that we considered were found to be unfavorable. However, our investigations resulted in one plausible ordered structure: We propose $ThTi_3$ in the Cr_3Si structure as a metastable ordered alloy.[26]

1.2.2 Effect of Hubbard *U* parameter

The second part of this study highlights the importance of the Hubbard *U* parameter for the proper determination of the structural, elastic, and mechanical properties and energetics of formation for the various actinide compounds with 5*f* electrons. This part is divided into two chapters.

Firstly, the electronic structure and properties of protactinium and its oxides (PaO and PaO_2) were studied within the framework of the Local Spin Density Approximation (LSDA), GGA (PBE), LDA plus the Hubbard U Correction (LDA+U) and GGA plus the Hubbard U Correction (GGA+U) implementations of DFT. The dependence of selected observables of these materials on the effective U parameter has been investigated in detail. The examined properties include lattice constants, bulk moduli, effect of charge density distributions, the hybridization of the 5*f* orbital and the energy of formation for PaO and PaO_2. The LSDA yields better agreement with experiments for the bulk modulus than the GGA for Pa, while GGA results in better lattice parameters. We observed that PaO is metallic while PaO_2 is a Mott-Hubbard insulator[27] (materials that should conduct electricity under conventional band theories, but are insulators when measured). This is consistent with observations for the other actinide oxides.[28] We discovered that GGA and LSDA incorrectly give metallic behavior for PaO_2. The GGA+U calculated indirect band gap of 3.48 eV reported for PaO_2 is a prediction and should stimulate further studies of this material.[29] Other oxides involving uranium, neptunium and plutonium were not explored because they have been studied previously within the DFT+ U approach.[30;31;32;33;9]

Secondly, we present a detailed comparative study of the electronic and mechanical properties of the early actinide mononitrides and dinitrides within the framework of the GGA (PBE) and GGA+U implementations of DFT with the inclusion of spin-orbit coupling. The dependence of selected observables of these materials on the effective U-parameter is investigated in detail. The properties include the lattice constant, bulk modulus, charge density distribution, hybridization of the atomic orbitals, energy of formation and the lattice dynamics. The inclusion of the Hubbard U parameter results in a proper description of the 5*f* electrons, and is subsequently used in the determination of the structural and electronic properties of these compounds. The mononitrides and dinitrides of the early actinides are metallic except for UN_2, which is a semiconductor. These actinide nitrides are non-magnetic with the exception of UN, NpN, PuN, NpN_2 and PuN_2: these are magnetic systems with orbital-dependent magnetic moments oriented in the z-axis. We observed that ThN_2 is elastically unstable to isotropic pressure. We discovered that UN_2 is thermodynamically unstable, but may be stabilized by N vacancy formation.[34;6;10]

1.3 Thesis structure

The structure of the thesis is described below:

- Chapter 1 presents a brief and general introduction. Some properties of the actinide compounds and the motivation behind the studies are highlighted. In-depth introductions and further motivations behind these studies are presented in the subsequent sections on individual systems considered.
- In Chapter 2, the theoretical formulation used to develop and implement DFT as a practical tool in the study of many-body systems is presented. Also, a brief overview on the need for an additional parameter, the onsite Hubbard correction term U for certain systems, is given. Methods and algorithms implemented to make the calculation practical for large systems are presented. Furthermore, the basic theory on the elasticity and lattice dynamics needed to ascertain structural strength and stability is covered.
- Chapter 3 presents the studies on the various stoichiometries of Th-Ti based compounds. A detailed study on Th-Ti based alloys is carried out to evaluate their stability and feasibility.
- In Chapter 4 the studies on the Th-N based compounds are presented. We explored the electronic properties, elastic properties and the energetics of the various compounds.
- Chapter 5 presents the studies on Pa and its oxides. We explored the electronic properties, elastic properties, lattice dynamics and the energetics of the various compounds. Also, we investigated the effect of the Hubbard U parameter and magnetic configuration on these systems.
- Chapter 6 contains the studies on various actinide nitrides. We explored the electronic properties, elastic properties, lattice dynamics and the energetics of the various compounds. In addition, we investigated the effect of the Hubbard U parameter and magnetic configuration on these systems.
- In Chapter 7, a the general conclusion is drawn.

In the next chapter, the theoretical framework is introduced, with emphasis placed on DFT and DFT plus the Hubbard U Correction (DFT+U).

Chapter 2

Theoretical Framework

First, the methodology used in the study of physical and electronic properties of real materials is introduced. This involves determining the solution of the Schrödinger equation using *ab initio* based methods. In this study, total energy of any given system, which is a many body problem, is obtained using DFT. DFT using quantum mechanical based concepts, which relies on the notion that the physical properties (equilibrium lattice constants, bulk moduli, phonons, piezoelectric constants, phase transition pressures and temperature, etc.) and the electronic properties (band structure, density of states, valence charge density distribution, etc.) of any given system can be accurately determined provided the charge density and ionic framework is known. Subsequently, the algorithms implemented within the broad theory of DFT for the determination of the total energy is presented. Next, the theory behind the calculation of the elastic properties and the lattice dynamics are provided. Lastly, we discuss the basic background of DFT+U approximation, which is relevant in capturing the physics of strongly correlated systems.

2.1 Many-Body Problem

Any given material can be described as a quantum mechanical system that is composed of atoms and consists of a positive core (referred to as the ion) surrounded by a cloud of electrons. Neglecting relativistic effects, this quantum mechanical system is described by solving the many-body fully-interacting Schrödinger equation:[35]

$$\hat{H}\Psi = E\,\Psi$$
$$\left[\hat{T}_I + \hat{T}_e + \hat{V}_{II} + \hat{V}_{ee} + \hat{V}_{eI}\right]\Psi(\{\mathbf{r}_i, \sigma_i\}) = E\Psi(\{\mathbf{r}_i, \sigma_i\}) \tag{2.1}$$

where Ψ is the many-body wavefunction dependent on both the ionic and electronic degrees of freedom ($\mathbf{R}_\alpha$ and $\mathbf{r}_i, \sigma_i$).

The ionic (I) and electronic (e) kinetic energy terms are given below as:

$$\hat{T}_I = \sum_{\alpha=1}^{N} -\frac{\hbar^2}{2M_\alpha}\nabla_\alpha^2 \tag{2.2}$$

$$\hat{T}_e = \sum_{i=1}^{n} -\frac{\hbar^2}{2m}\nabla_i^2. \tag{2.3}$$

The potential energy terms describing the various interactions are given by:

$$\hat{V}_{II} = \frac{1}{2}\sum_{\alpha\neq\beta}\frac{e^2\,Z_\alpha Z_\beta}{|\mathbf{R}_\alpha - \mathbf{R}_\beta|}\,, \tag{2.4}$$

where $\hat{V}_{II}$ is the potential energy due to ion-ion interactions

$$\hat{V}_{ee} = \frac{1}{2}\sum_{i\neq j}\frac{e^2}{|\mathbf{r}_i - \mathbf{r}_j|}\,, \tag{2.5}$$

where $\hat{V}_{ee}$ is the potential energy due to electron-electron interactions, and

$$\hat{V}_{eI} = -\sum_{\alpha=1}^{N}\sum_{i=1}^{n}\frac{e^2 Z_\alpha}{|\mathbf{R}_\alpha - \mathbf{r}_i|} \tag{2.6}$$

where $\hat{V}_{eI}$ is the potential energy due to electron-ion interactions.

To solve equation 2.1, the ionic and electronic degree of freedom is partially decoupled using the concept of Born-Oppenheimer Approximation (BOA), which is also referred to as the adiabatic approximation. This approximation assumes that the faster moving electrons become the stationary ground state for a given instantaneous configuration of the slowly varying nuclei, which arises due to the massive mass difference between the electrons and nuclei, and hence, results in the simplification of the many-body problem.[36] The many-body wavefunction is a product of electronic and ionic wavefunctions with the electronic Schrödinger equation given by:

$$[\hat{T}_e + \hat{V}_{ee} + \hat{V}_{eI}]\Psi_e(\{\mathbf{r}_i, \sigma_i\}, \{\mathbf{R}_\alpha\}) = E_e(\mathbf{R}_\alpha)\, \Psi_e(\{\mathbf{r}_i, \sigma_i\}, \{\mathbf{R}_\alpha\}). \tag{2.7}$$

The electronic wavefunction has a parametric dependence on the fixed ionic configuration but not on their velocities

$$\Psi(\{\mathbf{R}_\alpha\}, \{\mathbf{r}_i, \sigma_i\}) = \Psi_I(\{\mathbf{R}_\alpha\})\, \Psi_e(\{\mathbf{r}_i, \sigma_i\}, \{\mathbf{R}_\alpha\}). \tag{2.8}$$

Therefore, the electronic energy obtained is an effective interaction potential that varies with the ionic configurations in the ionic Schrödinger equation given by:

$$[\hat{T}_I + \hat{V}_{II} + E_e(\mathbf{R}_\alpha)]\Psi_I(\mathbf{R}_\alpha) = E_I\, \Psi_I(\mathbf{R}_\alpha). \tag{2.9}$$

It is now imperative to find the ground state wavefunction that minimizes the following Hamiltonian for the electronic system

$$\begin{aligned} [\hat{T}_e + \hat{V}_{int} + \hat{V}_{ext}]\Psi(\mathbf{r}_i, \sigma_i) &= E\, \Psi(\mathbf{r}_i, \sigma_i) \\ E = \langle \Psi|\hat{H}|\Psi\rangle = \langle \hat{T}\rangle + \langle \hat{V}_{int}\rangle &+ \int d^3\mathbf{r}\, V_{ext}(\mathbf{r})\, n(\mathbf{r}) \end{aligned} \tag{2.10}$$

where $\hat{V}_{ee} = \hat{V}_{int}$ is the potential from electron-electron interaction, $\hat{V}_{eI} = \hat{V}_{ext}$ is the potential from electron-ions interaction and $n(\mathbf{r})$ is the electronic density.

The major challenge in solving the electronic Schrödinger equation is that of determining the electron-electron interaction potential. Various approaches have been formulated that incorporate this interaction to make the problem more manageable. The Hartree-Fock approximation (HF)[37;38] is the simplest approach, which accounts for the anti-symmetric nature of many-electron wavefunction called Pauli correlation by using a *Slater determinant*[39] that minimizes the Hamiltonian of a fully interacting system.[40]

$$\Psi_e(\{\mathbf{r}_i, \sigma_i\}) = \Phi = \frac{1}{\sqrt{N}} \begin{vmatrix} \Phi_1(\mathbf{r}_1, \sigma_1) & \Phi_2(\mathbf{r}_1, \sigma_1) & \Phi_3(\mathbf{r}_1, \sigma_1) & \dots & \Phi_1(\mathbf{r}_1, \sigma_1) \\ \Phi_1(\mathbf{r}_2, \sigma_2) & \Phi_2(\mathbf{r}_2, \sigma_2) & \Phi_3(\mathbf{r}_2, \sigma_2) & \dots & \Phi_N(\mathbf{r}_2, \sigma_2) \\ \Phi_1(\mathbf{r}_3, \sigma_3) & \Phi_2(\mathbf{r}_3, \sigma_3) & \Phi_3(\mathbf{r}_3, \sigma_3) & \dots & \Phi_N(\mathbf{r}_3, \sigma_3) \\ \vdots & \vdots & \vdots & \ddots & \\ \Phi_1(\mathbf{r}_N, \sigma_N) & \dots & \dots & & \Phi_N(\mathbf{r}_N, \sigma_N) \end{vmatrix} \tag{2.11}$$

$$\Phi_i(\mathbf{r}_j, \sigma_j) = \Psi_i^\sigma(\mathbf{r}_j)\alpha_i(\sigma_j)$$

where each single particle spin-orbital $\Phi_i(\mathbf{r}_j, \sigma_j)$ can be decoupled into its position $\Psi_i^{\sigma}(\mathbf{r}_j)$ and spin variable $\alpha_i(\sigma_j)$ components.

The expectation value of the many-body electronic Schrödinger equation (spin independent) of equation 2.7 using the wavefunction (equation 2.11) in Hartree atomic units (where $\hbar = m_e = e = 4\pi/\varepsilon_0 = 1$) is given by:[40]

$$\begin{aligned} E_{HF} = \langle \Phi \left| \hat{H} \right| \Phi \rangle = \sum_{i,\sigma} \int d^3\mathbf{r}\, \Psi_i^{\sigma *}(\mathbf{r}) [-\frac{1}{2}\nabla^2 + V_{eI}]\, \Psi_i^{\sigma}(\mathbf{r}) + E_{II} \\ + \frac{1}{2} \sum_{i,j,\sigma_i,\sigma_j} \int d^3\mathbf{r}\, d\mathbf{r}'\, \Psi_i^{\sigma_i *}(\mathbf{r})\, \Psi_j^{\sigma_j *}(\mathbf{r}') \frac{1}{|\mathbf{r} - \mathbf{r}'|}\, \Psi_i^{\sigma_i}(\mathbf{r}')\, \Psi_j^{\sigma_j}(\mathbf{r}) \\ - \frac{1}{2} \sum_{i,j,\sigma} \int d^3\mathbf{r}\, d\mathbf{r}'\, \Psi_i^{\sigma *}(\mathbf{r})\, \Psi_j^{\sigma *}(\mathbf{r}') \frac{1}{|\mathbf{r} - \mathbf{r}'|}\, \Psi_j^{\sigma}(\mathbf{r}')\, \Psi_i^{\sigma}(\mathbf{r}). \end{aligned} \tag{2.12}$$

The first term in equation 2.12 is the single-body expectation value, the second term describes the classical interaction between the nuclei, the third term gives the direct exchange interactions and the fourth term accounts for the exchange interactions among electrons. The fictitious self-interactions in the direct and exchange terms also known as the self-interaction terms are included but cancel each other out. Including these interactions and summing over all orbitals results in the electron density, while the direct term is the Hartree energy given by:

$$E_H = \frac{1}{2} \int d^3\mathbf{r}\, d\mathbf{r}'\, \frac{n(\mathbf{r})\, n(\mathbf{r}')}{|\mathbf{r} - \mathbf{r}'|} \tag{2.13}$$

where the classical charge density of the self-interacting energy with density $n(\mathbf{r})$ is used to treat E_H.

The exchange energy term comprises of two effects: from the self-term and Pauli exclusion. This effects must be deducted to cancel out the spurious self-term included in the direct Coulomb Hartree energy. The exchange energy leads to lowering of the energy as a result of each electron interacting with its positive exchange hole. This is the difference between the total energy of the interacting many-body system of density $n(\mathbf{r})$ and the HF system with anti-symmetric uncorrelated electrons given below as:

$$E_x = E - E_{HF} = [\langle \hat{V}_{int} \rangle - E_H]_{HF}. \tag{2.14}$$

The minimization of equation 2.12 with respect to all the degrees of freedom using the many-body wavefunction in the form of equation 2.11 gives the single-electron HF equations as presented below

$$[-\frac{1}{2}\nabla^2 + V_{el}(\mathbf{r}) + V_H(\mathbf{r}) + V_x^{i,\sigma}(\mathbf{r})]\, \Psi_i^{\sigma}(\mathbf{r}) = \epsilon_i^{\sigma}\, \Psi_i^{\sigma}(\mathbf{r})$$

$$V_H(\mathbf{r}) = \sum_{j,\sigma_j} \int d^3\mathbf{r}'\, \Psi_j^{\sigma_j *}(\mathbf{r}')\, \Psi_j^{\sigma_j}(\mathbf{r}')\, \frac{1}{|\mathbf{r}-\mathbf{r}'|} = \int d^3\mathbf{r}' \frac{n(\mathbf{r}')}{|\mathbf{r}-\mathbf{r}'|} \tag{2.15}$$

$$V_x^{i,\sigma}(\mathbf{r}) = -\left[\sum_j \int d^3\mathbf{r}'\, \Psi_j^{\sigma *}(\mathbf{r}')\, \Psi_i^{\sigma}(\mathbf{r}')\, \frac{1}{|\mathbf{r}-\mathbf{r}'|}\right] \frac{\Psi_j^{\sigma *}(\mathbf{r}')}{\Psi_i^{\sigma *}(\mathbf{r}')}.$$

The Hartree potential V_H accounts for the electric fields of the other electrons and they act as a smooth background electron density $n(\mathbf{r})$ to the single electron. The exchange potential V_x incorporates the Pauli exclusion principle for all the electrons and eliminates the self-interaction terms in V_H.

The solution to the many-body problem using HF is intractable except for very small systems and specialized cases. Another way to solve the many-body problem, which is currently the most popular method, entails changing from N internal degrees of freedom to a single quantity: the ground state electron density using Density Functional Theory (DFT). Note that, DFT is an exact formalism and Hartree-Fock approach is forever an approximation.

2.2 Density Functional Theory

The two theorems by Hohenberg and Kohn [41] in 1964 laid the foundation for DFT and can be stated (as presented Richard Martin's book [40]) as follows:

Theorem 1 For any system of interacting particles in an external potential $V_{ext}(\mathbf{r})$, the potential $V_{ext}(\mathbf{r})$ is determined uniquely, except for a constant, by the ground state particle density $n_0(\mathbf{r})$.

Corollary I: Since the Hamiltonian is thus fully determined, except for a constant shift of the energy, it follows that the many-body wavefunctions for all states (ground and excited) are

determined. *Therefore all properties of the system are completely determined given only the ground stated density* $n_0(\boldsymbol{r})$.

Theorem 2 A *universal functional* for the energy E[n] in terms of the density $n_{(\mathbf{r})}$ can be defined, valid for any external potential $V_{ext(\mathbf{r})}$. For any particular $V_{ext(\mathbf{r})}$, the exact ground state energy of the system is the global minimum value of this functional, and the density $n_{(\mathbf{r})}$ that minimizes the functional is the exact ground state density $n_0(\mathbf{r})$.

Corollary II: The functional E[n] alone is sufficient to determine the exact ground state energy and density. In general, excited states of the electrons must be determined by other means.

Using a *reductio ad absurdum* Theorem 1 is proved as follows:

Given two different $\mathrm{V}^{(1)}_{ext}(\mathbf{r})$, $\mathrm{V}^{(2)}_{ext}(\mathbf{r})$ with the same ground state density $n_0(\mathbf{r})$ but different Hamiltonians $\hat{H}^{(1)}$ and $\hat{H}^{(2)}$ and ground state wavefunction $\Psi^{(1)}$ and $\Psi^{(2)}$, it follows using the Rayleigh Ritz variational principle, that:

$$E^{(1)} = \langle \Psi^{(1)} | \hat{H}^{(1)} | \Psi^{(1)} \rangle < \langle \Psi^{(2)} | \hat{H}^{(1)} | \Psi^{(2)} \rangle. \tag{2.16}$$

Hence

$$\begin{aligned} E^{(1)} &< \langle \Psi^{(2)} | \hat{H}^{(2)} | \Psi^{(2)} \rangle + \langle \Psi^{(2)} | \hat{H}^{(1)} - \hat{H}^{(2)} | \Psi^{(2)} \rangle \\ &< E^{(2)} + \int d^3\mathbf{r} [V^{(1)}_{ext}(\mathbf{r}) - V^{(2)}_{ext}(\mathbf{r})]\, n_0(\mathbf{r}). \end{aligned} \tag{2.17}$$

Similarly, considering $E^{(2)}$ results in

$$\begin{aligned} E^{(2)} &< \langle \Psi^{(1)} | \hat{H}^{(1)} | \Psi^{(1)} \rangle + \langle \Psi^{(1)} | \hat{H}^{(2)} - \hat{H}^{(1)} | \Psi^{(1)} \rangle \\ &< E^{(1)} + \int d^3\mathbf{r} [V^{(2)}_{ext}(\mathbf{r}) - V^{(1)}_{ext}(\mathbf{r})]\, n_0(\mathbf{r}). \end{aligned} \tag{2.18}$$

Addition of equation 2.17 and equation 2.18 results in the contradictory inequality

$$E^{(1)} + E^{(2)} < E^{(1)} + E^{(2)}, \tag{2.19}$$

hence the same ground state density cannot yield two external potentials that differ by more than a constant. Therefore the external potential $\mathrm{V}_{ext}(\mathbf{r})$ is uniquely determined to within a constant by the ground state density $n_0(\mathbf{r})$, for a system of interacting particles.

Provided the functional of the density is properly defined, theorem 2 is proved as follows

$$\begin{aligned} E_{HK}[n] &= T[n] + E_{int}[n] + \int d^3\mathbf{r}\, V_{ext}\, n(\mathbf{r}) + E_{II} \\ &\equiv F_{HK}[n] + \int d^3\mathbf{r}\, V_{ext}\, n(\mathbf{r}) + E_{II} \end{aligned} \tag{2.20}$$

where $F_{HK}[n] = T[n] + E_{int}[n]$ represents all internal energies, kinetic and potential energy; while E_{II} represents the interaction energy of the nuclei.

For a system having a ground state density $n^{(1)}(\mathbf{r})$ with wavefunction $\Psi^{(1)}$, which corresponds to an external potential $V^{(1)}$, and a different density $n^{(2)}(\mathbf{r})$, which corresponds to a wavefunction $\Psi^{(2)}$, then

$$\begin{aligned} E^{(1)} &= E[n^{(1)}] = \langle \Psi^{(1)} | \hat{H}^{(1)} | \Psi^{(1)} \rangle \\ E^{(2)} &= E[n^{(2)}] = \langle \Psi^{(2)} | \hat{H}^{(1)} | \Psi^{(2)} \rangle > E^{(1)} \end{aligned} \tag{2.21}$$

Therefore the evaluated ground state density $n^{(1)}(\mathbf{r})$ is indeed a global minimum of the Hohenberg-Kohn energy functional. Also, the exact ground state density and energy can be obtained by minimizing the total energy of a given system with respect to changes in the density function $n(\mathbf{r})$ provided the functional $F_{HK}[n]$ is known.

The brilliance of DFT is finding the solution to the density $n(\mathbf{r})$ in 3-dimension that minimizes the functional $E[n(\mathbf{r})]$ rather than the solution of the N-body problem in equation 2.7. In the current form of equation 2.20, the solution is intractable and general properties of the system cannot be deduced from the density since the exact form of the universal energy functional is unknown.[40]

2.3 Kohn-Sham equations

Kohn and Sham[42] in 1965 transformed the problem of the fully interacting system to a non-interacting *auxiliary* system which has the same ground state density, leading to the practicality of DFT.

This electronic ground state density is defined as

$$n(\mathbf{r}) = \sum_{\sigma} n^{\sigma}(\mathbf{r}) = \sum_{\sigma} \sum_{i}^{N^{\sigma}} \left| \Psi_i^{\sigma}(\mathbf{r}) \right|^2 , \tag{2.22}$$

where $\sigma =\uparrow$ or $\downarrow$ spin for all Kohn-Sham (KS) electron orbitals $\Psi_i^\sigma(\mathbf{r})$.

The energy functional for the auxiliary system has the form [43]

$$E_{KS}[n] = T_s[n] + E_H[n] + \int d^3\mathbf{r}\, V_{ext}(\mathbf{r})\, n(\mathbf{r}) + E_{xc}[n]$$

$$with\, T_s[n] = \sum_\sigma \sum_i^{N^\sigma} \langle \Psi_i^\sigma | \hat{T} | \Psi_i^\sigma \rangle \tag{2.23}$$

$$E_H = \frac{1}{2} \int d^3\mathbf{r}\, d\mathbf{r}'\, \frac{n(\mathbf{r})\, n(\mathbf{r}')}{|\mathbf{r} - \mathbf{r}'|}$$

where the Hartree energy is as presented in equation 2.13.

The auxiliary KS energy functional has the same ground state energy as the fully interacting energy functional, which is solvable. The exchange-correlation (XC) energy E_{xc} contains all the difficult many-body terms missing and some corrections related to the kinetic energy, going from a fully interacting system to the auxiliary KS non-interacting system, allowing the KS equation to be an exact formulation. [40]

$$E_{xc}[n] = E[n] - E_H[n] \tag{2.24}$$

Using the KS variational equation, [40]

$$\frac{\delta E_{KS}}{\delta \Psi_i^{\sigma *}(\mathbf{r})} = \frac{\delta T_S}{\delta \Psi_i^{\sigma *}(\mathbf{r})} + \left[\frac{\delta E_{ext}}{\delta n^\sigma(\mathbf{r})} + \frac{\delta E_H}{\delta n^\sigma(\mathbf{r})} + \frac{\delta E_{xc}}{\delta n^\sigma(\mathbf{r})} \right] \frac{\delta n^\sigma(\mathbf{r})}{\delta \Psi_i^{\sigma *}(\mathbf{r})} = 0 \tag{2.25}$$

depending on the constraints of orbital orthonormalization

$$\langle \Psi_i^\sigma | \Psi_j^{\sigma'} \rangle = \delta_{i,j} \delta_{\sigma,\sigma'}. \tag{2.26}$$

This results in the KS equations

$$\left[-\frac{1}{2}\nabla^2 + V_{ext} + V_H + V_{xc}^{\sigma}\right] \Psi_i^{\sigma} = \varepsilon_i^{\sigma}\, \Psi_i^{\sigma}$$

$$V_{ext}(\mathbf{r}) = \frac{\delta\, E_{ext}}{\delta\, n^{\sigma}(\mathbf{r})}$$

$$V_H(\mathbf{r}) = \frac{\delta\, E_H}{\delta\, n^{\sigma}(\mathbf{r})} = \int d^3\mathbf{r}'\, \frac{n(\mathbf{r})}{|\mathbf{r} - \mathbf{r}'|} \tag{2.27}$$

$$V_{xc}^{\sigma}(\mathbf{r}) = \frac{\delta\, E_{xc}}{\delta\, n^{\sigma}(\mathbf{r})}$$

The crucial term in the KS approach is the XC energy. The exact form of the XC is unknown, with the exception of the free electron gas. Therefore, there is a need for approximations to carry out practical calculations.

2.3.1 Local Spin Density Approximation

The first approximation to account for the E_{xc} is the LSDA. In this approximation, the general inhomogeneous electronic system is considered as a local homogeneous electron gas.[42] The XC energy density at each point $\mathbf{r}$ is the same as homogenous electron gas with the same density.

$$\begin{aligned} E_{xc}^{LS\,DA}[n^{\uparrow}, n^{\downarrow}] &= \int d^3\mathbf{r}\, n(\mathbf{r})\, \varepsilon_{xc}^{hom}(n^{\uparrow}(\mathbf{r}), n^{\downarrow}(\mathbf{r})) \\ &= \int d^3\mathbf{r}\, n(\mathbf{r})\, \left(\varepsilon_x^{hom}(n^{\uparrow}(\mathbf{r}), n^{\downarrow}(\mathbf{r})\right) + \varepsilon_c^{hom}(n^{\uparrow}(\mathbf{r}), n^{\downarrow}(\mathbf{r}))) \end{aligned} \tag{2.28}$$

The formulation of LSDA can be in terms of $n^{\uparrow}$ and $n^{\downarrow}$, or $n(\mathbf{r})$ and the fractional spin polarization parameter $\xi(\mathbf{r})$

$$\xi = \frac{n^{\uparrow} - n^{\downarrow}}{n}. \tag{2.29}$$

$E_{xc}^{LS\,DA}$ is generated using highly accurate results from the Quantum Monte-Carlo simulation established by Ceperley and Alder[44] and parameterized by Perdew and Zunger[45] that has a simple analytical form.

The LSDA potential undergoes an asymptotic decay having an exponential form, whereas the true XC potential decays in a Coulombic manner much slower. This leads to various deficiencies in the LSDA potential such as: (i) Inability to support a Rydberg series and to bind with high energy states. A consequence of that is very high HOMO energy, which gives inaccurate ionization potential based on Koopman's theorem. (ii) Also, erroneous predication of species as being unstable as a result of poor description of electron-rich species such as anions because often these do not bind to an additional electron.[40]

In spite of the above-mentioned drawbacks, LSDA has proven to be successful,[46;40] even though it relies on the assumption that the electron density is slowly varying. The reasons are that the XC hole obeys all the sum rules and does not require a detailed shape for the hole. Also, there is error cancellation in the exchange and correlation energy. The success of LSDA has led to its extensive use and the motivation for improved XC functionals (like the GGA).

2.3.2 Generalized Gradient Approximation

The GGA tries to remedy the deficiency of the LSDA, by taking into account the gradient of the electron density. This involves inclusion of the subsequent term in the derivative expansion of the electron density,

$$\begin{aligned} E_{xc}^{GGA}[n^{\uparrow}, n^{\downarrow}] &= \int d^3\mathbf{r}\, \epsilon_{xc}(n^{\uparrow}, n^{\downarrow}, |\nabla n^{\uparrow}|, |\nabla n^{\downarrow}|, \ldots) \\ &\equiv \int d^3\mathbf{r}\, \epsilon_x^{hom}(n) F_{xc}(n^{\uparrow}, n^{\downarrow}, |\nabla n^{\uparrow}|, |\nabla n^{\downarrow}|, \ldots) \end{aligned} \tag{2.30}$$

where ϵ_x^{hom} gives the exchange energy of the unpolarized gas and F_{xc} is a dimensionless quantity.

Symbolically GGA is presented as follows:

$$E_{xc}^{GGA} = E_{xc}^{GGA}(n(\mathbf{r}), \nabla n(\mathbf{r})) \tag{2.31}$$

where $\nabla n(\mathbf{r})$ is the gradient of the density as a function of position.

GGA offers significant improvement in the treatment of molecules compared to LSDA. It leads to improvement in the total energies, atomization energies, energy barriers and structural

energy differences. However, GGA tends to expand and soften bonds, sometimes overcorrecting the LSDA prediction. Generally, GGA is more suitable for inhomogeneity in density than LSDA.[47] Among the numerous available GGA XC functionals there are three widely used forms of the these: Beck (B88) [48], Perdew and Wang (PW91)[49] and Perdew, Burke, and Enzerhof (PBE)[47]. Moreover, various forms of PBE (revPBE, PBEsol[50], rPBE, etc.) have been developed to deal with different kinds of systems (surfaces, closed packed systems, defects, etc).

2.4 Algorithms used in the implementation of the Kohn-Sham equation

The various algorithms implemented in practice to obtain the converged total energy of any given system are presented. These algorithms solve the KS equations employing different techniques like:

1. Using localized atomic orbitals to study atom-like features typically used in chemistry.
2. Using the augmented plane wave (APW), Green's functions Korringa-Kohn-Rostoker (KKR)[51;52] and the muffin-tin orbital (MTO) methods, etc., which implements the atomic sphere methods.
3. Using the plane wave grid approach that implements fast Fourier transform (FFT) to determine the solution of the KS equations.

The plane wave grid approach as implemented in the VASP code is used in this study.

2.4.1 Plane wave formalism

In practice, crystalline solids have a finite number of atoms and a very large number of electrons. Based on the periodicity of the system, the large number of one-electron wavefunctions is reduced to approximately half the electron number in the unit cell of the crystal by application of Bloch's theorem.[53] For any periodic system, the KS potential is a periodic function given as:

$$V_{KS}(r+R) = V_{KS}(r);\ \forall R \in \textbf{Bravias Lattice}. \tag{2.32}$$

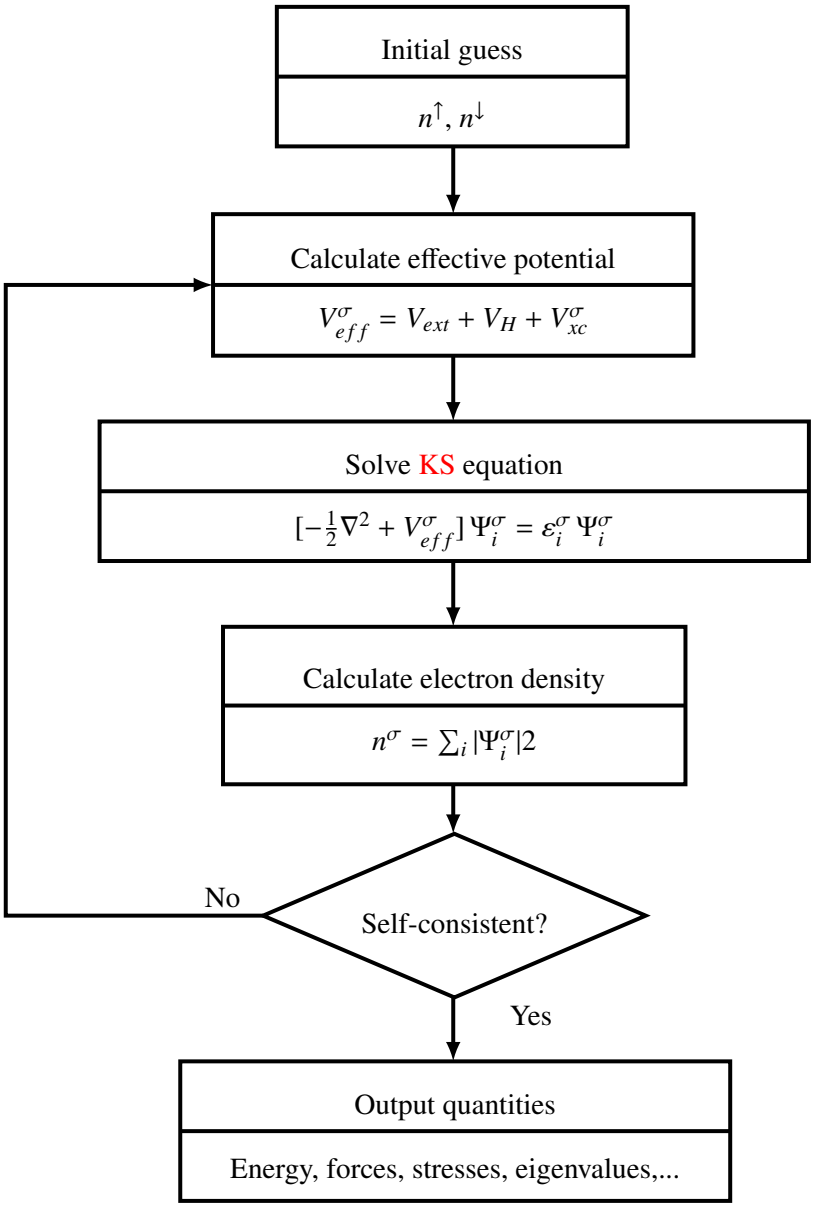

Figure 2.1: Schematic representation of the Self-Consistent Field (SCF) procedure to solve the KS equations.[54]

Applying the Bloch theorem shows that the wavefunction of an electron in a periodic potential is a product of the plane wave $e^{ik.r}$ and the cell periodic function $u_i(\mathbf{r})$:

$$u_i(\mathbf{r}) = \sum_{\mathbf{G}} c_{i,\mathbf{G}}\ e^{i\mathbf{G}.r}$$
$$\psi_i(\mathbf{r}) = e^{ik.r} u_i(\mathbf{r}) = \sum_{\mathbf{G}} c_{i,\mathbf{k}+\mathbf{G}}\ e^{i\mathbf{k}+\mathbf{G}.r} \tag{2.33}$$

Where, the electronic wavefunction is the sum of the plane waves at each **k**-point within the first Brillouin zone (BZ) and $c_{i,\mathbf{k}+\mathbf{G}}$ are the coefficients of the planes waves. Substituting equation 2.33 into equation 2.23 allows the KS equations to be expressed in the reciprocal space[53]

$$\sum_{\mathbf{G}'} \left(\frac{\hbar^2}{2m} |\mathbf{k}+\mathbf{G}|^2 \delta_{\mathbf{G}\mathbf{G}'} + V_{ion}(\mathbf{G}-\mathbf{G}') + V_H(\mathbf{G}-\mathbf{G}') + V_{xc}(\mathbf{G}-\mathbf{G}') \right) c_{i,\mathbf{k}+\mathbf{G}'} = \epsilon_i c_{i,\mathbf{k}+\mathbf{G}'}. \tag{2.34}$$

Therefore, using Bloch's theorem, the infinite solution of equation 2.23 can be determined, where the electronic wavefunction is represented as an expansion of plane waves that involves the convergence of a single parameter, the energy cut-off E_{cut} (which originates from the kinetic energy term). The kinetic energy term is diagonal, and the various potentials in equation 2.23 are described in terms of their Fourier transforms.[53] The use of fast Fourier transforms allows for translation between real and reciprocal space, significantly improving the efficiency of plane waves calculations. In equation 2.34, the kinetic energy term is the diagonal components and the potentials are given in terms of their Fourier components.

For practical calculation, we define the kinetic energy cut-off as shown in equation 2.35, which limits the maximum length of the G vectors leading to a finite Hamiltonian matrix.

$$E_{cut} = \frac{\hbar^2}{2m} |\mathbf{k}+G|^2. \tag{2.35}$$

The truncation of the plane waves expansion that results in the kinetic energy term being less than the cut-off energy might introduce errors in the computed total energy of some systems. Hence, an increase in the E_{cut} would lead to reduction of the error in the total energy.

The flowchart in Fig. 2.1 summarizes the KS equations derived in section 2.3 and expanded in equation 2.34. This shows how an actual calculation can be performed to determine the

ground state energy, forces, stresses, etc. A numerical procedure is implemented in DFT codes to successively update the n and V_{eff} until self-consistency is achieved.

2.4.2 Pseudopotential

In the pseudopotential approximation, the numerous plane waves in the tightly bound core electrons are replaced with an effective potential acting on the valence electrons.[55;56;57;58;59]. This approach was developed largely from the Orthogonalized Plane Wave (OPW) method introduced by Herring,[60] where the expansion of the valence wavefunctions in a set of plane waves is orthogonalized to all of the core wavefunctions. The orthogonality of the wavefunctions is because they are eigenstates of a Hermitian operator. It effectively reduces the computational time required for convergence of the total energy of the system.

In Fig. 2.2, the pseudo wavefunction oscillates less than the original wavefunction; hence, needs fewer plane waves to describe compared to the original plane wavefunctions. The pseudo wavefunction is applicable to a large number of systems, which is a smooth function within the core region.[61]

Several methods exist for pseudopotentials generation; therefore they are not unique. However, they must satisfy the following criteria:

1. The pseudo wavefunctions and the atomic wavefunctions must produce the same core charge (both should agree beyond a chosen core radius R_c).

2. The pseudo-electron and the atomic eigenvalues must be the same for a chosen atomic reference configuration.

3. Logarithmic derivatives of the two wavefunctions at R_c must be norm-conserving (should agree).

4. The integrated charge inside the R_c must be norm-conserving.

5. The *first energy derivative* of the logarithmic derivatives must agree at Rc for both wavefunctions.

As a result of points 1 and 2, the pseudo atom and the ionic core will yield the same scattering properties while a smooth pseudo-electron wavefunction is guaranteed from point 3. From point 4, the correct charge inside the core is guaranteed, and point 5 guarantees an adequate description of an ion in a quantum system for a given pseudopotential. The choice of the R_{cut}

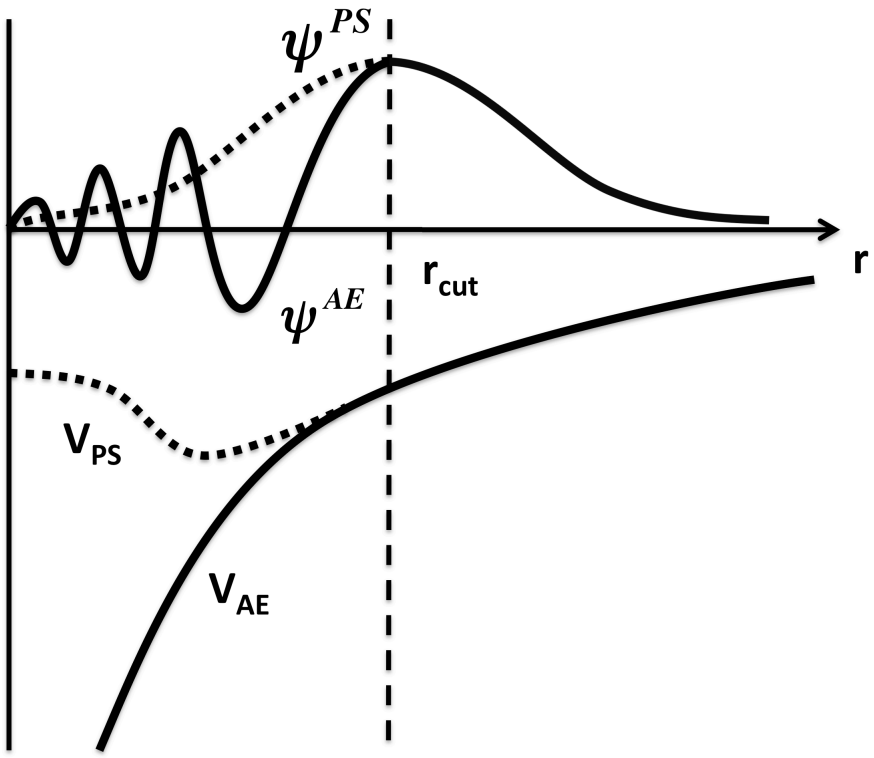

Figure 2.2: Schematic representation of the pseudopotential method, where the all-electron (solid lines) and pseudo-electron (dashed lines) potentials and their corresponding wave functions. They both agree at the designated radius r_{cut} .

ensures adequate description of the wavefunction close to the atom but large enough to give smooth wavefunctions.

Various pseudopotentials have been developed such as: the norm-conserving pseudopotential (the norm of each pseudo-wavefunction is identical to the all-electron (AE) wavefunction outside the cutoff radius), the ultrasoft pseudopotential (reducing the basis-set size by relaxing the constraint imposed by the norm-conserving), etc. A closely related technique is the projector augmented wave (PAW) method (this leads to greater computational efficiency, which takes into account concepts from the pseudopotential and linear augmented-plane-wave methods).

2.4.3 Projector augmented wave method

The PAW[62;63;64] method reformulates the OPW method, leading to marked improvement in the norm conserving[65] and ultrasoft[66] pseudopotential methods. This approach is adaptable to modern methods for total energy, force, and stress calculations leading to high computational efficiency and accuracy. However, complexity can arise in its implementation. This approach maintains the full core wavefunctions and uses the pseudopotential operators.

The PAW method maps the physical all electron (AE) valence wavefunctions $\psi_j^v(\mathbf{r})$ onto a smooth pseudo wavefunctions $\tilde{\psi}_i^v(\mathbf{r})$, which is similar to the OPW and the augmented plane wave (APW) formulation.[40] Also, a linear combination of $\psi^v = \tau\tilde{\psi}^v$ links the set of all-electron valence functions to their smooth pseudo wavefunction. The transformation is taken to be unity $\tau = 1$ except when a sphere is centered on the nucleus, $\tau = \mathbf{1} + \tau_0$. In PAW formulation, the Dirac notation is adopted. The expansion of the smooth wavefunction within the sphere (superscript v and subscript i, j are neglected for simplicity) is given as

$$|\tilde{\psi}\rangle = \sum_m c_m |\tilde{\psi}_m\rangle \tag{2.36}$$

and the corresponding all electron wavefunction

$$|\psi\rangle = \sum_m c_m |\psi_m\rangle. \tag{2.37}$$

The full wavefunction in all space is given as

$$|\psi\rangle = |\tilde{\psi}\rangle + \sum_m c_m \{|\psi_m\rangle - |\tilde{\psi}_m\rangle\}. \tag{2.38}$$

The coefficients c_m represent the projection in each sphere, for a linear transformation τ

$$c_m = \langle \tilde{p}_m | \tilde{\psi}\rangle. \tag{2.39}$$

Provided that for some set of the projection operators $\tilde{p}$ the biorthogonality condition is satisfied,[40]

$$\langle \tilde{p}_m | \tilde{\psi}'_m\rangle = \delta_{mm'} \tag{2.40}$$

it follows that one-center expansion

$$\sum_m |\tilde{\psi}_m\rangle\langle\tilde{p}_m|\tilde{\psi}\rangle$$
$$\tilde{\psi}_m = \tilde{\psi}_m \tag{2.41}$$

of the smooth function is unchanged.

The transformation operator τ unlike the pseudopotential involves the full AE wavefunction

$$\tau = \mathbf{1} + \sum_m \{|\psi_m\rangle - |\tilde{\psi}_m\rangle\}\langle|\tilde{p}_m|. \tag{2.42}$$

The PAW equations can be written in the form of equation 2.42. The variation of the parameters leads to more response from the smooth wavefunction compared to the AE wavefunction. Therefore the expectation value of the smooth function is given as follows[40]

$$\tilde{A} = \tau^\dagger \hat{A}\tau = \hat{A} + \sum_{m,m'} \{\langle\psi_m|\hat{A}|\psi_{m'}\rangle - \langle\tilde{\psi}_m|\hat{A}|\tilde{\psi}_{m'}\rangle\}\langle|\tilde{p}_m|, \tag{2.43}$$

The charge density and total energy of a given system can be evaluated from the operator in equation 2.43. The density is divided into the smooth charge density $\tilde{n}(\mathbf{r})$ evaluated on a regular Fourier grid and the outer centre charge densities $n^1(\mathbf{r})$ and $\tilde{n}^1(\mathbf{r})$ evaluated in the angular momentum on the radial grid, given by:

$$n(\mathbf{r}) = \tilde{n}(\mathbf{r}) + n^1(\mathbf{r}) - \tilde{n}^1(\mathbf{r}). \tag{2.44}$$

The smooth and outer charge density components can be expressed in terms of the eigenstates labeled i with occupation f_i, where

$$\tilde{n}(\mathbf{r}) = \sum_i f_i |\tilde{\psi}_i(\mathbf{r})|^2, \tag{2.45}$$
$$\tag{2.46}$$
$$n^1(\mathbf{r}) = \sum_i f_i \sum_{mm'} \langle\tilde{\psi}_i|\tilde{\psi}_m\rangle\psi^*_m(\mathbf{r})\psi_{m'}(\mathbf{r})\langle\tilde{\psi}_{m'}|\tilde{\psi}_i\rangle, \tag{2.47}$$

and the last term given as

$$\tilde{n}^1(\mathbf{r}) = \sum_i f_i \sum_{mm'} \langle\tilde{\psi}_i|\tilde{\psi}_m\rangle\tilde{\psi}^*_m(\mathbf{r})\tilde{\psi}_{m'}(\mathbf{r})\langle\tilde{\psi}_{m'}|\tilde{\psi}_i\rangle, \tag{2.48}$$

where the outer centre charge densities $n^1(\mathbf{r})$ and $\tilde{n}^1(\mathbf{r})$ are localized around each atom and the integrals evaluated in the spherical coordinates. The VASP[67] code in this thesis implements this method, along with other codes such as ABINIT,[68] Quantum Espresso,[69] etc.

2.4.4 Brillouin zone integration

The total energy for a given system can be determined if the KS eigenvalues are known. The eigenvalues are self-consistent solutions of the **k**-dependent Hamiltonian.[70] The first BZ can be mapped out by a continuous set of **k**-points throughout the reciprocal space. To carry out a numerical calculation for the total energy, the integral over the first BZ is converted into a summation over discrete points in **k**-space. The **k**-points represent the position in the first BZ where the electronic states are calculated in a solid system. The choice of the k-points should maximize accuracy and minimize the number of **k**-points set because for each new **k**-point a self-consistent KS calculation will be carried out. Errors in the self-consistent calculation can be minimized by using a dense set of **k**-points in the BZ (metallic systems need more **k**-points because of difficulty in calculating the Fermi surface).

2.4.4.1 Linear tetrahedron method

Lehmann[71] developed the linear tetrahedron method, which is largely used to evaluate integrals in the BZ. This was further improved by Bloch *et al.*[72] In this approach, the irreducible wedge of the BZ is divided into equal volume tetrahedra, with the matrix element and the energy eigenvalues evaluated at each vertex.

In this study, this method is used for the BZ integration due to its simplicity. But some problems might arise due to the negligence of the second-order band information leading to difficulties in band crossing and bad representation of the van Hove singularities.[73]

2.4.4.2 Special k-points

In this study, the special **k**-points are used to determine the choice of points needed to sample the BZ. They are well suited for the plane wave representation of the Hamiltonian and lead to simple and accurate calculations. This approach uses the ”mean value point” developed by Baldereschi[74] that integrates a function averaged over the entire BZ, which was extended by Chadi[75], while later a more systematic approach was devised by Monkhorst and Pack[76;77]

$$F(r) = \frac{\Omega}{2\pi^3} \int_{BZ} f(k) d^3k \tag{2.49}$$

where Ω is the volume of the unit cell, $f(k)$ is the Fourier transformation of F(r) and the function provides a complete representation of the lattice symmetry. The Fourier transform is given in terms of $A_m(k)$:

$$f(k) = f_o + \sum_{m=1} A_m(k) \tag{2.50}$$

where the transformation expression $A_m(k) = \sum e^{ik.r}$ and m is any given integer. $A_m(k)$ is a real function and is associated with any given shell of the lattice. Using this scheme, the integral in equation 2.49 yields an approximate value that is exact when $A_m(k) = 0$.

The Monkhorst and Pack generated set of points using this scheme provides an unbiased approach for choosing the set of **k**-points required to sample the BZ in fractional co-ordinates. Monkhorst and Pack-points are also referred to as **k**-mesh. They present the generated points in a rectangular grid (k_x, k_y, k_z). Larger **k**-mesh leads to finer and more accurate sampling but uses up increased computational time. The **k**-mesh is determined by the crystal lattice (simple cubic, body centered cubic, face centered cubic, etc.), and therefore takes advantage of the space group symmetry operations to reduce computed points by determining equivalent points. $A_m(k)$ in equation 2.50 is satisfied by the choice points for the lattice vectors (represented by the infinite set of nearest-neighbor shells).

2.4.4.3 Fermi level smearing

The basic difference between an insulator and a metal is the presence of a band gap which is determined by the location of the Fermi level in the systems. In terms of BZ integration,[78] insulators play a smooth function with the density of state easily going to zero, while metals have unoccupied states close to the Fermi level; hence the necessity to smear the bands to obtain a smooth integrated function which is more tractable. There are various kinds of smearing schemes, such as, Methfessel-Paxton (MP), Gaussain, Fermi-Dirac and Marzari-Vanderbilt smearing.[78] The MP smearing is used in this study because of the systems investigated and its simplicity.

The MP smearing scheme expands the delta-function in the form of *Hermite functions* (which are the product of Hermite polynomials and Gaussians) then integrates it.

$$\delta(x) \approx D_N = \sum_{n}^{N} A_n H_{2n} e^{-x^2} \tag{2.51}$$

where A_n are suitable coefficients. They use Hermite polynomials of even order only since the delta function is even. The delta function is obtained by integrating D_N in the following way

$$\delta(x) \approx S_N = 1 - \int_{-\infty}^{x} D_N(t)dt \tag{2.52}$$

Using recursion properties of Hermite functions, we arrive at

$$\begin{aligned} S_N &= S_0 x + \sum_{n}^{N} A_n H_{2n-1} e^{-x^2} \\ S_0 &= \frac{1}{2}(1 - erf(x)) \end{aligned} \tag{2.53}$$

where S_0 corresponds to the Fermi-Dirac smearing whereas the other terms serve to correct errors introduced. MP smearing results in good zero temperature energies using large smearing widths, but has a downside, which is the presence of negative occupation values that might be problematic in visualizing the density of states. The proposed Marzari-Vanderbilt approach addresses the negative occupancies by estimating the delta-function with a Gaussian multiplied by a first order polynomial term.

2.4.5 Atomic relaxations

To study the atoms in different coordination, a self-consistent total energy calculation is required. The forces acting on the atoms needs to be determined in order to update the atomic positions (geometric optimization) and then determine the dynamic evolution of the system. These forces can be obtained using the Hellmann-Feynman theorem.

2.4.5.1 Hellmann-Feynman theorem

The Hellmann-Feynman theorem[79;80] (also referred to as the force theorem)[40] proposes that the force on the atoms is given by[40]

$$\mathbf{F}_I = \frac{\partial E_{Tot}}{\partial \mathbf{R}_I} = -\{\frac{\partial}{\partial \mathbf{R}_I}\langle\psi_i|H|\psi_i\rangle + \frac{\partial E_{ion}}{\partial \mathbf{R}_I}\}, \tag{2.54}$$

where $\mathbf{R}_I$ represents the atomic positions. If the wavefunction ψ_i is an eigenstate of a given Hamiltonian H, then

$$\frac{\partial}{\partial \mathbf{R}_I}\langle\psi_i|H|\psi_i\rangle = \langle\psi_i|\frac{\partial H}{\partial \mathbf{R}_I}|\psi_i\rangle. \tag{2.55}$$

Based on the fact that the energy is an extremal with respect to all feasible changes of the wavefunction at the true ground state solution (using equation 2.55), the force will be

$$\mathbf{F}_I = -\{\langle\psi_i|\frac{\partial}{\partial\mathbf{R}_I}H|\psi_i\rangle + \frac{\partial E_{ion}}{\partial\mathbf{R}_I}\}. \tag{2.56}$$

From equation 2.56, the partial derivative of the KS energy functional with respect to the atomic positions gives the force on the atoms provided each wavefunction ψ_i is an eigenstate of H. However, to avoid incurring errors that arise from the use of unconverted wavefunctions, the Hellmann-Feynman theorem should only be implemented once the wavefunctions are close to self-consistency because the force (unlike the energy) is not a variational quantity.

In equation 2.54, an additional term called the *Pulay force* can arise from taking the partial derivative of the basis set with respect to their atomic positions. Using a plane-waves basis, the *Pulay force* vanishes because the derivate reduces to zero, which is one of the numerous advantages of this basis set compared to any other localized basis set approach.

The Broyden-Fletcher-Goldfarb-Shanno (BFGS) algorithm,[81] also known as the *quasi-Newton* or the *variable metric* method, implements the Hellmann-Feynman theorem for the convergence of the total energy with respect to the atomic positions. This approach is based on the fact that the energy surface around the minimum is quadratic, and therefore, can be determined from the second derivative of the energy, which is a Hessian matrix. But the Hessian matrix is unknown, so an approximation is made, using a progressive improvement of the trial matrix as the atoms move. The BFGS method is used in this study because it leads to a rapid convergence of the total energy.

2.5 Elastic Properties

The elastic constants characterize the elastic behavior of a given material. They describe its reaction to an applied stress. The relationship between stress and strain is not trivial in a general anisotropic material. Stress and strain comprise three tensile and shear components respectively, resulting in six components in total. The stiffness tensor of elasticity subscripts obey the added condition that[82] $ijkl = klij$, since the strain tensor is symmetric.

Theoretically and experimentally the knowledge of elastic constants leads to the understanding of the elastic properties of any given system. The elastic constants of a given crystal can be determined by using a strain matrix "**e**" to shift the Bravais lattice vector **R = a,b,c**,

leading to the deformation of the unit cell, therefore, changing the unstrained Bravais lattice vector to $\mathbf{R}' = \mathbf{a}', \mathbf{b}', \mathbf{c}'$

$$\mathbf{R}' = \mathbf{R}\begin{pmatrix} \mathbf{1}+\mathbf{e}_{xx} & \frac{1}{2}\mathbf{e}_{xy} & \frac{1}{2}\mathbf{e}_{xy} \\ \frac{1}{2}\mathbf{e}_{yx} & \mathbf{1}+\mathbf{e}_{yy} & \frac{1}{2}\mathbf{e}_{yz} \\ \frac{1}{2}\mathbf{e}_{zx} & \frac{1}{2}\mathbf{e}_{zy} & \mathbf{1}+\mathbf{e}_{zz} \end{pmatrix}. \tag{2.57}$$

The total energy of the crystal changes in accordance with the deformation equation[78]

$$\begin{aligned} E_{tot} &= E_0 + \frac{1}{2} V_0 C_{ij} e_i e_j \\ U &= \frac{(E_{tot} - E_0)}{V_0} = \frac{1}{2}\sum_{i=1}^{6}\sum_{j=1}^{6} C_{ij} e_i e_j \end{aligned} \tag{2.58}$$

where E_0 is the total energy of the undisturbed lattice, V_0 is the equilibrium volume of the undisturbed cell and the C_{ij} are the elements of the elastic constant matrix. Based on the symmetry of the unit cell, the stiffness tensor (elastic constants) contains a maximum of 21 unique elements[78] as shown in Table 2.1.

Table 2.1: Number of unique elastic constants for unit cells of different symmetry

Crystal system	Elastic constant
Triclinic	21
Monoclinic	13
Orthorhombic	9
Tetragonal	6 or 7
Rhombohedral	6 or 7
Hexagonal	5
Cubic	3

[1]

A detailed description of the symmetry of stress, strain and elastic constants is furnished by Nye.[83] The *ab initio* elastic constants are determined by carefully choosing the applied deformation (strain) and the resulting stress. This method is less computationally intensive because structural optimization is not required.

[1] This table was copied from the Medea manual[78]

As stated earlier, from the elastic constants, the elastic properties of all crystal classes can be determined. The bulk modulus of a given material is the ratio of the change in pressure to the fractional volume compression.

The bulk modulus (upper bound) from the Voigt approach:

$$K_{Voigt} = \frac{1}{9}(c_{11} + c_{22} + c_{33}) + \frac{2}{9}(c_{12} + c_{23} + c_{13}) \tag{2.59}$$

The shear modulus (upper bound) from the Voigt approach:

$$G_{Voigt} = \frac{1}{15}(c_{11} + c_{22} + c_{33}) - \frac{1}{15}(c_{12} + c_{23} + c_{31}) + \frac{1}{5}(c_{44} + c_{55} + c_{66}) \tag{2.60}$$

Given that S_{ijkl} is the compliance matrix (i.e. the inverse matrix to C), the bulk modulus (lower bound) from the Reuss approach:

$$1/K_{Reuss} = (s_{11} + s_{22} + s_{33}) + 2(s_{12} + s_{23} + s_{13}) \tag{2.61}$$

The shear modulus (lower bound) from the Reuss approach:

$$15/G_{Reuss} = 4(s_{11} + s_{22} + s_{33}) - 4(s_{12} + s_{23} - s_{13}) + 3(s_{44} + s_{55}) + s_{66} \tag{2.62}$$

In real (polycrystalline) materials, the stiffness matrix takes into account orientational disorder. This can be estimated if the system is assumed to be made up of crystallites rather than grain boundaries.[84] Using that approach, Hill proposed that the true modulus is an arithmetic mean of two extremes, which are the Voigt (lower bounds) and Reuss (upper bounds) moduli.[85]

$$\begin{aligned} G_{Hill} &= \frac{1}{2}\left[G_{Voigt} + G_{Reuss}\right] \\ K_{Hill} &= \frac{1}{2}\left[K_{Voigt} + K_{Reuss}\right] \end{aligned} \tag{2.63}$$

where G and K are the shear and bulk moduli respectively.

Subsequently, the Poisson's ratio (α) and Young's modulus (Y) can be determined from G and K

$$\begin{aligned} \alpha &= \frac{1}{2}\left[\frac{K - \frac{2}{3}G}{K + \frac{1}{3}G}\right] \\ Y &= \frac{9K}{1 + \frac{3B}{G}} \end{aligned} \tag{2.64}$$

Correspondingly, the Debye temperature which measures the hardness or stiffness of a material is proportioned to the mean sound velocity, and is given as[84]

$$\theta_D = \frac{\hbar}{k_B}\left(\frac{6\pi q}{V_0}\right)^{1/3} v_m, \tag{2.65}$$

where h/k_B have the usual definition as in quantum mechanics, q is the number of atoms in the system, and V_0 is the equilibrium volume of the unit cell. And, the mean v_m sound velocity is given by

$$v_m = \left(\frac{1}{3}\left(\frac{2}{{v_s}^3} + \frac{1}{{v_l}^3}\right)\right)^{-1/3}, \tag{2.66}$$

where the transverse v_s and longitudinal v_l sound velocity are defined by

$$\begin{aligned} v_s &= \sqrt{G/\rho} \\ v_l &= \sqrt{\left(K + \frac{4}{3}G\right)/\rho} \end{aligned} \tag{2.67}$$

with ρ as the density.

2.6 Lattice Dynamics

From BOA, the dependence of electronic energies on the motion of the nuclei is neglected. Therefore, the equations of motion for the ions are determined by the total energy E($\mathbf{R}$) of the system, which has a parametric dependence on the fixed positions of the ions' $\mathbf{R}$.[40]

To give a complete quantum description of the ions from the Schrödinger equation is very difficult[86] but treating the ions classically, reduces the problem to that of a coupled classical equation of motion for each ionic position $\mathbf{R}_I(t)$

$$M_I \frac{\partial^2 \mathbf{R}_I}{\partial_t} = \mathbf{F}_I(\mathbf{R}) = \frac{\partial}{\partial_t} E(\mathbf{R}), \tag{2.68}$$

where R_I are the coordinates and M_I is the mass of the ions I, $R \equiv \{R_I\}$ shows the set of all ionic coordinates, and $E(\mathbf{R})$ is the ground state total energy, which is also referred to as the *Born-Oppenheimer energy surface*.

The energy is expanded in terms of the powers of displacements and external perturbation for stable solid systems at average temperature. At equilibrium position $\{\mathbf{R}^0\} = \mathbf{R}^0$, the zero-force on each ion is

$$\mathbf{F}_I(\mathbf{R}^0) = 0. \tag{2.69}$$

At the quantum-zero point motion, the higher power of displacements gives the thermal vibrations and response to perturbations,[40]

$$C_{I,\alpha;J,\beta} = \frac{\partial^2 E(\mathbf{R})}{\partial \mathbf{R}_{I,\alpha} \partial \mathbf{R}_{J,\beta}}, C_{I,\alpha;J,\beta;K,\gamma} = \frac{\partial^2 E(\mathbf{R})}{\partial \mathbf{R}_{I,\alpha} \partial \mathbf{R}_{J,\beta} \partial \mathbf{R}_{K,\gamma}}, \ldots, \tag{2.70}$$

where $\alpha, \beta, \ldots,$ represent Cartesian components.

Using the *harmonic approximation*[87], the displacements describe the vibrational modes at frequency ω

$$\mathbf{u}_I(t) = \mathbf{R}_I(t) - \mathbf{R}_I^0 \equiv \mathbf{u}_I e^{i\omega t}. \tag{2.71}$$

Then, for a given I, equation 2.68 becomes

$$-\omega^2 M_I u_{I\alpha} = -\sum_{j\beta} C_{I,\alpha;J,\beta} u_{J\beta}. \tag{2.72}$$

The classical equation provides the complete solution for all vibrational states, which is the set of independent oscillators having individual vibrational frequency ω

$$det \left| \frac{1}{\sqrt{M_I M_J}} C_{I,\alpha;J,\beta} - \omega^2 \right| = 0. \tag{2.73}$$

where the dependence upon the masses M_I, M_J is given in a symmetric form.

Since the atomic displacement eigenvectors in a crystal obey the Bloch theorem (equation 2.33) the vibrations are grouped by $\mathbf{k}$ with the displacements $\mathbf{u}_s(\mathbf{T_n}) \equiv \mathbf{R}_s(\mathbf{T_n}) - \mathbf{R}_s^0(\mathbf{T_n})$ of atom $s = 1, S$ in the cell $\mathbf{T_n}$ given by

$$\mathbf{u}_s(\mathbf{T_n}) = e^{ik.\mathbf{T_n}} \mathbf{u}_s(\mathbf{k}). \tag{2.74}$$

Putting equation 2.74 into equation 2.73 results in the decoupling of the equations at different $\mathbf{k}$, with frequencies $\omega_{i\mathbf{k}}, i = 1, 3S$ called dispersion curves, which are solutions of the $3S \times 3S$ determinants equation

$$det \left| \frac{1}{\sqrt{M_s M_s'}} C_{s,\alpha;s',\alpha'}(\mathbf{k}) - \omega_{i\mathbf{k}}^2 \right| = 0, \tag{2.75}$$

where the reduced force constant matrix for wave vector $\mathbf{k}$ is presented as

$$C_{s,\alpha;s',\alpha'}(\mathbf{k}) = \sum_{\mathbf{T_n}} e^{ik.\mathbf{T_n}} \frac{\partial^2 E(\mathbf{R})}{\partial \mathbf{R}_{s,\alpha}(0) \partial \mathbf{R}_{s',\alpha'}}(\mathbf{T_n}) = \frac{\partial^2 E(\mathbf{R})}{\partial \mathbf{u}_{s,\alpha}(\mathbf{k}) \partial \mathbf{u}_{s',\alpha'}}(\mathbf{k}). \tag{2.76}$$

Quantization can be easily included as usual for the harmonic oscillators because the vibrations are independent: phonons are the quantized states of each oscillator with energy $\hbar\omega_{i\mathbf{k}}$.

To calculate the phonons *ab initio*, three approaches have been developed: (i) the direct method which hinges on calculating the total energy changes or forces for atoms displaced slightly from their equilibrium position,[59](ii) using a perturbative expansion of atoms around their equilibrium position for analytical calculation of the force constant matrix,[88] (iii) the Fourier transform of the atomic velocity autocorrelation function calculated from a molecular dynamics trajectory.[78;89]

The major challenge for the third approach is equilibrating at reasonable simulating times; the second approach requires specialized codes and significant implementation efforts, while the first approach requires no specialized codes but makes use of a supercell for a small unit cell. The first approach is used in this thesis to determine the phonon frequencies, and an adequate interaction range is used to ensure accuracy.

2.7 DFT+U

LSDA/GGA XC functionals fail in properly describing the electronic structure and the conduction properties for highly localized and strongly interacting systems such as: in transition metal oxides and rare-earth metal compounds. They tend to over-delocalize electrons, and hence do not properly account for the onsite Coulomb repulsion. Self-interaction is a problem because the electrons can see their own potential. Also, the solution from LSDA/GGA is mean-field, hence the absence of correlation among the electrons. Some correlation phenomena exhibited by the *d* and *f* compounds include metal-insulator transitions, Mott insulators, heavy Fermion behavior, high-temperature superconductivity, etc. GGA functionals can lead to slight improvement over LSDA in some cases for the physical properties of non homogeneous systems, such as transition metal compounds and rare-earth metal compounds, mainly in description of there binding energies, magnetic and structural properties, e.g, UO_2, NiO, MnO, etc.[33;90;91] For most strongly correlated systems LSDA (or GGA) gives a reasonable description of the crystal structure and magnetic properties, but fails dramatically in the description of the conduction properties, while sometimes resulting in totally wrong structural properties (δ-Pu).[18]

The poor description of the electronic structure of correlated systems can be analyzed from a simple band structure calculation for a given system (such as a simple metal). If the band structure is calculated for the valence states with a stepwise increase in interatomic distances,

the width of energy bands around the Fermi level will diminish, leading to an insulating system at infinite interatomic distance. This leads to extremely localized charge density distribution around the atoms which hinders conduction of states around and crossing the Fermi level.[92;93]

To solve this paradoxical situation, the Hamiltonian of the many-body electron system is presented in terms of second quantization[94;93],

$$\begin{aligned} \hat{H} &= \hat{H}_0 + \hat{V}_{ee} \\ \hat{H}_0 &= \int d^3r\, a^\dagger_\sigma(\mathbf{r}) \left[\frac{\hat{\mathbf{p}}^2}{2m} + V_{ext}(\mathbf{r}) \right] a_\sigma(\mathbf{r}) \\ \hat{V}_{ee} &= \frac{1}{2} \int d^3r d^3r' V_{ee}(\mathbf{r}-\mathbf{r}') a^\dagger_\sigma(\mathbf{r}) a^\dagger_{\sigma'}(\mathbf{r}') a_{\sigma'}(\mathbf{r}') a_{\sigma'}(\mathbf{r}) \end{aligned} \tag{2.77}$$

where the localized basis states are:

$$a_\sigma(\mathbf{r}) = \sum_i \psi_{\mathbf{R}_i}(\mathbf{r}) a_{i\sigma} \quad a^\dagger_\sigma(\mathbf{r}) = \sum_i \psi^*_{\mathbf{R}_i}(\mathbf{r}) a^\dagger_{i\sigma}. \tag{2.78}$$

The Hamiltonian of the electronic system is:

$$\begin{aligned} \hat{H} &= \sum_{ii'} a^\dagger_{i\sigma} t_{ii'} a_{i'\sigma} + \sum_{ii'jj'} U_{ii'jj'} a^\dagger_{i\sigma} a^\dagger_{i'\sigma'} a_{j'\sigma'} a_{j\sigma} \\ t_{ii'} &= \int d^3r \psi^*_{\mathbf{R}_i}(\mathbf{r}) \left[\frac{\hat{\mathbf{p}}^2}{2m} + V(\mathbf{r}) \right] \psi^*_{\mathbf{R}'_i}(\mathbf{r}) \\ U_{ii'jj'} &= \frac{1}{2} \int d^3r d^3r' \psi^*_{\mathbf{R}_i}(\mathbf{r}) \psi_{\mathbf{R}_j}(\mathbf{r}) V(\mathbf{r}-\mathbf{r}') \psi^*_{\mathbf{R}_{i'}}(\mathbf{r}') \psi_{\mathbf{R}_{j'}}(\mathbf{r}'). \end{aligned} \tag{2.79}$$

The subsequent equation gives the "simplified Hubbard model". The $U_{ii'jj'}$ matrix elements are largest when $i = j$ and $i' = j'$

$$\hat{H} = \sum_{ii'} a^\dagger_{i\sigma} t_{ii'} a_{i'\sigma} + \sum_{ii'} U_{ii'ii'} a^\dagger_{i\sigma} a^\dagger_{i'\sigma'} a_{i'\sigma'} a_{i\sigma}. \tag{2.80}$$

If only $i = i'$ is most important then $\sigma \neq \sigma'$, and the Hamiltonian, becomes,

$$\begin{aligned} \hat{H} &= \textstyle\sum_{ii'} a^\dagger_{i\sigma} t_{ii'} a_{i'\sigma} + U \sum_i a^\dagger_{i\sigma} a^\dagger_{i,-\sigma} a_{i,-\sigma} a_{i\sigma} \\ &= \textstyle\sum_{ii'} a^\dagger_{i\sigma} t_{ii'} a_{i'\sigma} + U \sum_i a^\dagger_{i\sigma} a_{i\sigma} a^\dagger_{i,-\sigma} a_{i,-\sigma} \\ &= \textstyle\sum_{ii'} a^\dagger_{i\sigma} t_{ii'} a_{i'\sigma} + U \sum_i \hat{n}_{i\uparrow} \hat{n}_{i\downarrow}. \end{aligned} \tag{2.81}$$

The Hubbard model in a more concise form is

$$\hat{H}_0 = -t \sum_{<ij>} a^{\dagger}_{i\sigma} a_{j\sigma} + U \sum_{i} \hat{n}_{i\uparrow} \hat{n}_{i\downarrow}. \tag{2.82}$$

From equation 2.82, the total energy is minimized by two competing factors: the kinetic term and the Coulomb term. In simple metals, electron-electron scattering is weak with particles spending vanishingly small amount of time in the ionic regions, whereas in the strongly correlated systems (typically systems with partially filled *d* or *f* orbitals), the electron-electron scattering has a strong Coulomb repulsion due to the relatively large amount of time the electrons spend within the ionic regions. If the kinetic energy is dominant (in simple metals besides the nuclei attractions), the total energy is minimized by delocalization of the Bloch states resulting in metallic behavior. On the other hand, if the Coulomb term is dominant (in systems with partially filled *d* or *f* orbitals), the total energy is minimized by the localized states which are linear combinations of all **k**-states (Wannier states); hence the systems become insulating (Mott-Hubbard type).[93]

Therefore, band structure analysis gives an improper description of a correlated system. This is because it uses the KS DFT that is a one-body problem to account for a many-body problem. Also, the exchange correlation as previously stated is made primary for homogenous electron gas, and hence does not properly describe correlated systems. Therefore, theoretical treatment of correlated systems is carried out using model Hamiltonians (explicitly taking into account the behavior of the system in regimes with different competing factors) or the introduction of an additional parameter using hints from many-body formalism in first principle DFT calculation to account for onsite Coulomb repulsion, referred to as the DFT+U.[95;23;24;96;29]

The DFT+U method (henceforth referred to as LDA+U) takes into account the orbital dependence of the Coulomb and exchange interactions which is absent in the LDA. The main notion is to divide the electrons into two subsystems:[92;93]

- localized states (*d* or *f*) which accounts for the onsite Coulomb interaction term in a model Hamiltonian

$$\sum_{ii'} U_{ii'ii'} a^{\dagger}_{i\sigma} a^{\dagger}_{i'\sigma'} a_{i'\sigma'} a_{i\sigma} \Longrightarrow \frac{U}{2} \sum_{i \neq j} n_i n_j. \tag{2.83}$$

- delocalized states (*s* or *d*) which can be described by the orbital-independent one-electron potential.

The new energy functional which is the generalized LDA+U is given as

$$E^{LDA+U}[n] = E^{LDA}[n] + E^{U}[n_i^\sigma] - E^{dc}[n_i^\sigma] \tag{2.84}$$

where $E^U[n_i^\sigma]$ is the Hubbard term and $E^{dc}[n_i^\sigma]$ is the "double counting" term, which removes the energy contribution of orbitals already present in the LSDA functional included in the Hubbard term. The double counting term is a mean-field value of the Hubbard term in line with DFT representation. Hence $E^{dc}[n_i^\sigma]$ is $UN(N-1)/2$, where $N = \sum n_i$.

Therefore, the $E^{LDA+U}[n]$ functional is

$$E^{LDA+U}[n] = E^{LDA}[n] + \frac{U}{2}\sum_{i\neq j} n_i n_j - UN\frac{(N-1)}{2}. \tag{2.85}$$

The orbital eigenvalues or energies ϵ_i are obtained by taking the derivative of equation 2.85 with respect to the occupation number of that orbital n_i:

$$\begin{aligned} \epsilon_i = \frac{\partial E^{LDA+U}}{\partial n_i} &= \epsilon_i^{LDA} + U\sum_{j\neq i} n_j - \tfrac{U(N-1)}{2} - \tfrac{UN}{2} \\ &= \epsilon_i^{LDA} + U(N-n_i) - UN + \tfrac{U}{2} \\ &= \epsilon_i^{LDA} + U(\tfrac{1}{2} - n_i). \end{aligned} \tag{2.86}$$

For the occupied orbital ($n_i = 1$), the LSDA orbital energy is shifted by $-U/2$ and for the unoccupied orbitals ($n_i = 0$) by $+U/2$, as presented in equation 2.86. A similar expression is obtained for the LDA+U potential which is $V_i(\mathbf{r}) = V_{LDA}(\mathbf{r}) + U(\frac{1}{2} - n_i)$. The $V_i(\mathbf{r})$ formulation makes the Hubbard potential repulsive for less than a half filled orbital and attractive for more than a half filled orbital, encouraging localization on a particular site. This results in upper and lower Hubbard bands with the energy difference being equivalent to the Coulomb parameter U. This will qualitatively yield the correct physics of Mott-Hubbard insulators.[94;93] But, in order to obtain a quantitively accurate computational scheme, the direct and exchange Coulomb interaction inside a partially filled *d* or *f* orbital needs to be accounted for.

2.7.1 Rotationally-invariant formulation

The LDA+U formulation in equation 2.86 depends on the choice of the localized basis set because the atomic orbital is not rotationally invariant. Liechtenstein et al.[21] introduced a

formulation of LDA+U independent of the choice of basis set, where Hubbard on-site correlation functional E^U and the mean field double counting term E^{dc} have a generic expression obtained from the HF method to solve the orbital dependency. The E^U term is evaluated starting from equation 2.79, where the indices i, i', j, j' represents the different m orbitals of a given I subspace.[21]

$$\hat{E}^U[\{n\}] = \sum_{I,mm'm''m'''} U_{mm''m'm'''} a^\dagger_{m\sigma} a^\dagger_{m''\sigma'} a_{m'''\sigma'} a_{m'\sigma} \tag{2.87}$$

The matrix element associated with U is:

$$\begin{aligned} U_{mm''m'm'''} &= \tfrac{1}{2} \int d^3r d^3r' \psi^*_m(\mathbf{r}) \psi_{m'}(\mathbf{r}) V(\mathbf{r}-\mathbf{r}') \psi^*_{m''}(\mathbf{r}') \psi_{m'''}(\mathbf{r}') \\ &= \tfrac{1}{2} \langle m, m'' | V_{ee} | m', m''' \rangle \end{aligned} \tag{2.88}$$

If $\sigma \neq \sigma'$, we obtain

$$a^\dagger_{m\sigma} a^\dagger_{m''-\sigma} a_{m'''-\sigma} a_{m'\sigma} = a^\dagger_{m\sigma} a_{m'\sigma} a^\dagger_{m''-\sigma} a_{m'''-\sigma} = n^\sigma_{mm'} n^{-\sigma}_{m''m'''}. \tag{2.89}$$

and if $\sigma = \sigma'$, there are two possibilities:

$$\begin{aligned} a^\dagger_{m\sigma} a^\dagger_{m''\sigma} a_{m'''\sigma} a_{m'\sigma} &= a^\dagger_{m\sigma} a_{m'\sigma} a^\dagger_{m''\sigma} a_{m'''\sigma} = n^\sigma_{mm'} n^\sigma_{m''m'''} \\ a^\dagger_{m\sigma} a^\dagger_{m''\sigma} a_{m'''\sigma} a_{m'\sigma} &= a^\dagger_{m\sigma} a_{m'''\sigma} a_{m'\sigma} a^\dagger_{m''\sigma} = -n^\sigma_{mm'''} n^\sigma_{m''m'}. \end{aligned} \tag{2.90}$$

Putting together the Hubbard E^U term gives:

$$\begin{aligned} \hat{E}^U[\{n\}] = \frac{1}{2} \sum_{\{m\},\sigma} \{ &\langle m, m'' | V_{ee} | m' m''' \rangle n^\sigma_{mm'} n^{-\sigma}_{m''m'''} \\ &+ (\langle m, m'' | V_{ee} | m' m''' \rangle - \langle m, m'' | V_{ee} | m''' m' \rangle) n^\sigma_{mm'} n^{-\sigma}_{m''m'''} \} \end{aligned} \tag{2.91}$$

where V_{ee} accounts for the screened Coulomb electron-electron interactions. The E^{dc} term accounts for double counting but in the absence of orbital polarizations equation 2.84 gives the original E^{LSDA}. The double counting term is given by

$$E^{dc}[\{n\}] = \frac{1}{2} UN(N-1) - \frac{1}{2} J[N^\uparrow - (N^\uparrow - 1) + N^\downarrow (N^\downarrow - 1)] \tag{2.92}$$

where $N = N^{\uparrow} + N^{\downarrow}$, U and J are screened Coulomb and exchange terms.[97;95] The expression in equation 2.92 is referred to as the full localized limit (FLL). Czyzyk and Sawatzky [98] proposed another approach called around mean field expression for the E^{dc} term which is slightly different compared to the FLL.

In equations 2.91 and 2.92, the invariance stems from transformation of the interaction parameters as quadruplets of localized wave functions and the functional's dependence on the trace of the occupation matrices respectively.[92;93] While the V_{ee} integral accounts for the Coulomb electron-electron interaction of the localized basis (e.g. d or f), we can compute these quantities from the expansion of the Coulomb potential ($2/|r - r'|$) in terms of spherical harmonics:

$$\langle m, m''|V_{ee}|m'm'''\rangle = \int d^3r d^3r' R^*_{lm}(r)Y^*_{lm}R_{lm'}(r)Y^*_{lm'}V(r-r')R^*_{lm''}(r)Y^*_{lm''}R^*_{lm'''}(r)Y^*_{lm'''} \quad (2.93)$$

and $V(r - r')$ is

$$V(r-r') = \frac{1}{\epsilon(r-r')} = \frac{1}{\epsilon}\sum_{l=0}^{\infty}\frac{4\pi}{2l+1}\frac{r_<^l}{r_>^{l+1}}\sum_{m=-l}^{+l}Y_{lm}(r)Y^*_{lm}(r'). \quad (2.94)$$

Then

$$\langle m, m''|V_{ee}|m'm'''\rangle = \sum_k a_k(m, m'', m', m''')F^k \quad (2.95)$$

where $0 \leq k \leq 2l$ (l is the angular moment of the localized manifold; $-l \leq m \leq l$) and the a_k factors can be obtained as products of Clebsh-Gordan coefficients:

$$a_k(m, m'', m', m''') = \frac{4\pi}{2k+1}\sum_{q=-k}^{k}\langle l_m|Y_{kq}|lm'\rangle\langle l''_m|Y^*_{kq}|lm'''\rangle. \quad (2.96)$$

where $\langle l_m|Y_{l'm}|lm'\rangle$ are the Gaunt coefficients.

The V_{ee} integral contains the same angular dependence present in the HF electronic interactions, but they are calculated using a different approach that takes account of screening. In describing the d electrons, the Slater integrals F^0, F^2 and F^4 are needed, which are linked to the Coulomb and Stoner parameters U and J as shown below:

$$U = \frac{1}{(2l+1)^2}\sum_{m,m'}\langle m,m'|V_{ee}|m,m'\rangle = F^0$$
$$J = \frac{1}{(2l)(2l+1)}\sum_{m\neq m'}\langle m,m'|V_{ee}|m,m'\rangle = \frac{F^2+F^4}{14}. \tag{2.97}$$

where m and m' account for electronic orbitals with the identical l. For systems with f electrons, J can be expressed as $J = (286F^2 + 195F^4 + 250F^6)/6435$, which includes F^6.

2.7.2 A simplifier formulation

The most complete formulation of the LDA+U scheme is given in section 2.7.1 that is based on the multi-band Hubbard model. A simpler expression of the E^U has been formulated by Dudarev *et al.* [99] where only the lower order Slater integrals F^0 are retained and $F^2 = F^4 = J = 0$. This implies neglecting the non-sphericity of the electronic interactions ($a_0(m,m',m'',m''') = \delta_{m,m'}\delta_{m'',m'''}$), along with the coupling difference between the parallel spin and anti-parallel spin electrons (captured by J the exchange interaction). The energy functional can be obtained from recalculation of equations 2.91 and 2.92 from which we derive: [92;93]

$$\begin{aligned} E_U[\{n^{I\sigma}_{mm'}\}] &= E_{Hub}\left[\{n^I_{mm'}\}\right] - E_{dc}[\{n^I_{mm'}\}\Big] \\ &= \sum_I \frac{U^I}{2}\left[(n^I)^2 - \sum_\sigma Tr[(\mathbf{n}^{I^\sigma})^2\right] - \sum_I \frac{U^I}{2}n^I(n^I-1) \\ &= \sum_{I,\sigma}\frac{U^I}{2}Tr\left[(\mathbf{n}^{I^\sigma})(1-\mathbf{n}^{I^\sigma})\right]. \end{aligned} \tag{2.98}$$

The rotational invariance obtained in equations 2.91 and 2.92 is preserved in the simplified functional given in equation 2.98. This is because the "+U" functional depends on the trace of the occupation matrices and its products but the formal resemblance to the Hartree-Fock energy functional is missing. Therefore, only the U^I interaction parameter is necessary to account for the corrective functional. The simplified version of the Hubbard correction has been used in numerous studies and proved to be successful with similar results to the fully rotational invariant Hubbard correction. In some cases the Hund's rule coupling J is essential to determine the correct ground state of the system, for example in systems characterized by non-collinear magnetization, correlation effects in multi-band metals and heavy Fermion systems. For a detailed

discussion on the theoretical formulation of LDA+U, strengths, limitations and comparison with other corrective techniques see Reference 93.[93]

2.8 Software code

All calculations in this study were done within the framework of DFT as implemented in the VASP codes. The PAW method was used for the non-magnetic, spin-polarized and spin-orbit calculations. Elastic constants were obtained using the method of least-squares fit as implemented in the VASP/MedeA-MT module. Phonon dispersions were obtained using the direct method as implemented in the VASP/MedeA-PHONON module.

This concludes the overview of the theoretical framework. The next chapter presents the results of the *ab initio* studies on Th-N based alloys.

Chapter 3

Ab initio studies of Th_3N_4, Th_2N_3 and $Th_2N_2(NH)$

This section to be submitted for publication as[25] "Obodo, K. O., and Chetty, N. (2013). *Ab initio studies* of Th_3N_4, Th_2N_3 and $Th_2N_2(NH)$."

Ab initio studies of Th_3N_4, Th_2N_3 and $Th_2N_2(NH)$

K. O. Obodo[a], N. Chetty[a,b]

[a] *Physics Department, University of Pretoria, Pretoria 0002, South Africa*
[b] *National Institute for Theoretical Physics,Johannesburg, 2000, South Africa*

Abstract

Using density functional theory within the Perdew-Burke-Ernzerhof generalized gradient approximation [GGA (PBE)] implemented in the VASP codes, we investigate the structural, elastic and electronic properties of Th_3N_4, Th_2N_3 and $Th_2N_2(NH)$. The calculated structural properties of these thorium-based nitrides are in good agreement with experimental data. We observe that all the Th-N based compounds that we considered are energetically favorable and elastically stable. We find that Th_3N_4 is semiconducting with a band gap of 1.59 eV, which compares well with the experimental band gap of 1.7 eV and we find Th_2N_3 to be metallic. $Th_2N_2(NH)$, which is crystallographically equivalent to Th_2N_3, is insulating with a band gap of 2.12 eV. This is due to the -(NH) group that effects a shifting of the energy bands that results in the opening of a gap at the Fermi-level. The Th-N based compounds that we considered are predominantly ionic.

Keywords: A. Thorium nitride; C. Density functional theory; D. Electronic and structural properties

1. Introduction

Thorium-nitride (Th-N) based compounds are of great interest in the field of physics, chemistry and material science[1, 2, 3, 4] because of their properties such as high melting points, high metal density, high thermal conductivity, low creep rate, good corrosion resistance, etc. [5] For instance, these materials are used in nuclear reactor systems, in the breeder reactors where it is incorporated into the mixed actinide nitride fuels and in subcritical accelerator driven systems.

There have been several theoretical studies using first principles approaches and experimental studies of thorium mononitride. [6, 7, 8, 9, 10] To the best of our knowledge, a detailed theoretical analysis of the following Th-N based compounds within density functional theory (DFT) approach is absent: $Th_2N_2(NH)$, Th_2N_3 and Th_3N_4. The $Th_2N_2(NH)$ compound is known to be isomorphous to Th_2N_3 (also referred to as a sesquninitride). [11] $Th_2N_2(NH)$ and Th_2N_3 crystalizes in the La_2O_3-type hexagonal structure with space group $P3\bar{m}1$, whereas Th_3N_4 belongs to the *R-3m* space group. We have shown in our previous studies that standard density functional approximation without the inclusion of Hubbard *U* parameter gives an accurate description of the electronic, structural and elastic properties of thorium based systems. [5, 12]

Email addresses: kingsley.obodo@up.ac.za (K. O. Obodo), nithaya.chetty@up.ac.za (N. Chetty)

Recently, Silva *et al.* [11] experimentally synthesized $Th_2N_2(NH)$ by heating ThNF and $LiNH_2$. These workers characterized $Th_2N_2(NH)$ using x-ray diffraction (XRD), and the Rietveld analysis to determine the crystal structure along with DFT approach to elucidate the crystal chemistry. Also, from Fourier transform infrared spectroscopy (FTIR) and high-resolution transmission electron microscopic (HRTEM) images, they confirm the presence of -NH group due to the lattice fringe disruptions observed in nanoparticle areas of the nitride species.

In this letter, we use *ab initio* techniques to determine the structural, elastic, and electronic properties and the energy of formation for $Th_2N_2(NH)$, Th_2N_3 and Th_3N_4. Subsequently, by analysing the valence charge density distribution, we examine the compounds to investigate their bonding character. These systems are found to be non-magnetic (NM). The inclusion of spin-polarization (SP) or spin-orbit coupling (SOC) did not result in any changes to the structural, elastic and electronic properties. Hence, all the results presented are for the non-magnetic (NM) case.

2. Theory

We perform *ab initio* calculations on the Th-N based compounds using density functional theory [13] as implemented in the VASP code. [14] We use the Perdew-Burke-Ernzerhof (PBE) [15] exchange-correlation functional for the generalized gradient approximation (GGA). A kinetic energy cutoff of 550 eV is chosen to ensure adequately converged total energies for the compounds under consideration. A **k**-point spacing of 0.2 Å for the Monkhorst-Pack [16] grid is used to sample the Brillouin zone (BZ), and a Methfessel-Paxton smearing [17] width of 0.2 eV is used to integrate the bands at the Fermi level. The density of states function (DOS) is calculated using the tetrahedron integration method with Blöchl corrections. [18]

A method using the least-squares fit, [19] as implemented in the MedeA-MT module, is used to obtain the elastic constants. This method uses the tetrahedron method for the Brillouin zone integrations. The elastic properties are calculated from the Hill value, which is a geometric mean of the Voigt and Reuss values. The Hill values are used in the estimation of longitudinal (v_l), shear (v_s) and mean (v_m) sound velocities, and the Debye temperatures. [20]

The energy of formation for each compound is computed by taking the difference between the total energy of the Th-N based compounds and the sum of the energies of its constituents in their respective bulk elemental forms, and nitrogen in its diatomic gaseous form.

3. Results and Discussion

The crystal structures for Th_2N_3, $Th_2N_2(NH)$ and Th_3N_4 are presented in Fig. 1. The experimentally determined structures are fully optimized geometrically using highly converged parameters. A full description of the structural parameters for Th_2N_3, $Th_2N_2(NH)$ and Th_3N_4 is given in Ref 11, 21, 2.

In Table 1, we present the calculated lattice parameters (a_0 and c), c/a_0 and the energy of formation for $Th_2N_2(NH)$, Th_2N_3 and Th_3N_4. The calculated lattice parameters compare well with the given experimental data. The calculated bond distances for Th-N(1) and Th-N(2) are 2.922 Å and 2.373 Å respectively for $Th_2N_2(NH)$. This result is in good agreement with the XRD measurement [11] where the bond distances for Th-N(1) and Th-N(2) are 2.696 Å and 2.34 Å respectively.

The energy of formation for the Th-N based compounds considered is negative as presented in Table 3. This implies that the formation of these compounds is energetically favorable with

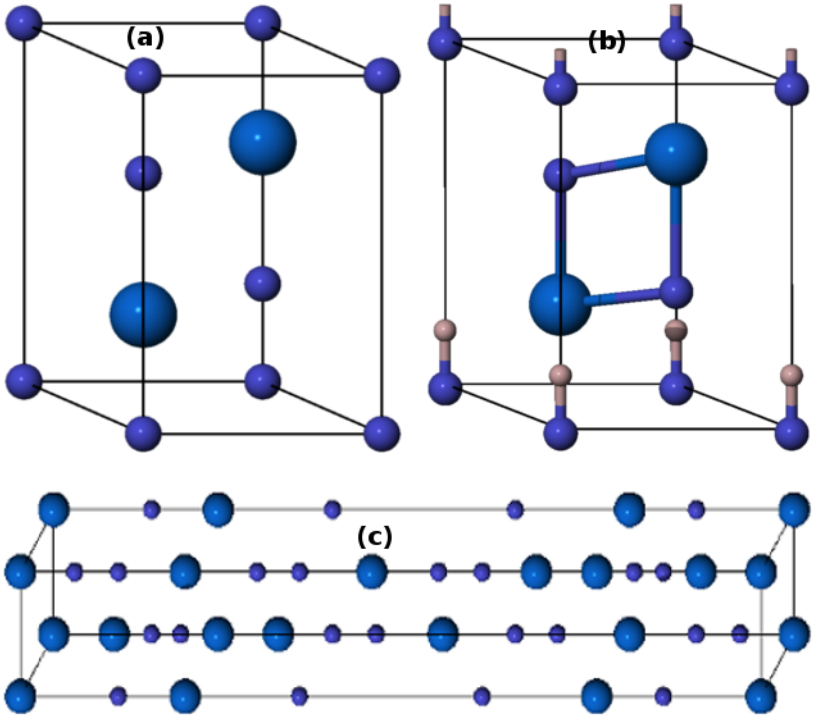

Figure 1: (Color online) The optimized structures for (a) Th_2N_3 (b) $Th_2N_2(NH)$ (c) Th_3N_4; where the blue atoms represents Th atoms, the purple atoms represents N atoms and the brown atoms represents the oxygen atoms.

respect to the elements in their standard state. We find that Th_3N_4 is the most energetically favorable nitride among those compounds considered.

Table 1: The calculated and experimental [21, 22] lattice constants, a (Å) and c (Å), c/a and the energy of formation (eV) per formula unit for the Th-N based compounds.

Compound	Method	a	c	c/a	E_f
Th_3N_4	GGA	3.882	27.452	7.072	-11.380
	Exp	3.873	27.385	7.072	-
Th_2N_3	GGA	3.913	6.161	1.575	-6.890
	Exp	3.875	6.175	1.594	-
$Th_2N_2(NH)$	GGA	4.021	6.165	1.533	-5.254
	Exp	3.886	6.185	1.592	-

The elastic properties of thorium-nitride based systems considered are calculated for the NM phase. The elastic constants (c_{ij}) obtained are shown in Table 2. The elastic stability is related to sum rules. Therefore, negative elastic constants does not necessary signify elastic instability.

Table 3 shows the calculated elastic properties of various ordered alloys of Th-N based compounds in the NM phase. They are elastically stable with positive bulk, shear and Young's

Table 2: Elastic constants Cijs (values in GPa).

Compounds	c_{11}	c_{12}	c_{13}	c_{14}	c_{33}	c_{44}
Th_3N_4	275.94	163.80	89.30	31.68	170.77	79.15
Th_2N_3	237.67	143.77	96.15	31.73	196.55	73.26
$Th_2N_2(NH)$	223.39	157.18	82.32	-18.94	109.24	92.50

moduli, positive shear velocity (obtained from the shear sound velocity) and positive longitudinal velocity (obtained from the longitudinal sound velocity). [23] The calculated bulk modulus for Th_3N_4, Th_2N_3 and $Th_2N_2(NH)$ are 147.92 GPa, 147.10 GPa and 121.51 GPa respectively. The mean velocity v_m calculated from shear (transverse) velocity v_s and longitudinal velocity v_l is used to determine the Debye temperature. The Debye temperature (θ_D) for the Th-N based nitrides is calculated to determine the stiffness of the system. The θ_D for the Th_3N_4 is highest at 311.6 K, which indicates that Th_3N_4 is stiffer compared to the other compounds considered.

Table 3: The bulk, shear and Young's moduli (Hill values in GPa), acoustic velocities (ms^{-1}), and Debye temperature (K)

Compounds	B	Shear	Young's	v_s	v_l	v_m	θ_D
Th_3N_4	147.92	60.54	159.73	2406	4677	2695	311.6
Th_2N_3	147.10	52.34	140.07	2256	4593	2533	297.2
$Th_2N_2(NH)$	121.51	44.64	118.94	2140	4309	2401	293.9

In Fig. 2, we present the computed total density of states (DOS) for the Th-N based compounds, together with projections on the thorium p, d, f, and nitrogen $2p$ states. Figure 2a and 2c show that Th_3N_4 and $Th_2N_2(NH)$ are insulating with a band gap of 1.59 eV and 2.12 eV respectively. The top of the valence band for Th_3N_4 and $Th_2N_2(NH)$ is determined mainly by the N-$2p$ states. The bottom of the conduction band shows significant hybridization of the thorium d and f states with the nitrogen $2p$ states in $Th_2N_2(NH)$ compound. For Th_3N_4, the bottom of the conduction band is determined mainly by the hybridization of the thorium d and f states. Gouder *et al.* [3], experimentally obtained a band gap of about 1.7 eV for Th_3N_4 using photoelectron spectroscopy studies. This agrees well with our theoretically predicted band gap. On the other hand, Figure 2b shows that Th_2N_3 is metallic. This metallicity is determined mainly by the N-$2p$ states. The insulating properties of $Th_2N_2(NH)$, which is crystallographically similar to metallic Th_2N_3 is attributed to the shifting of the valence band due to the presence of the -(NH) group. It is worth noting that these Th-N based compounds all show significant hybridization of the thorium p, d and f states with the nitrogen $2p$ states.

In order to elucidate the bonding characteristic for all the compounds considered, we present their valence charge density distribution plots in Figure 3. The charge density distribution is computed in the (110) plane. The scale in Figure 3 is such that blue is devoid of electrons and red has a high concentration of electrons. In general, we observe charge accumulation around N and charge depletion around the Th atoms. This suggests that there is charge transfer from thorium to nitrogen, indicating that the Th-N chemical bonds are primarily ionic in character. This is expected since the N atom is more electronegative than the metal actinide atom. Moreover, we observe in Figure 3 a slight charge accumulation between the atomic spheres compared to the rest of the interstitial regions.

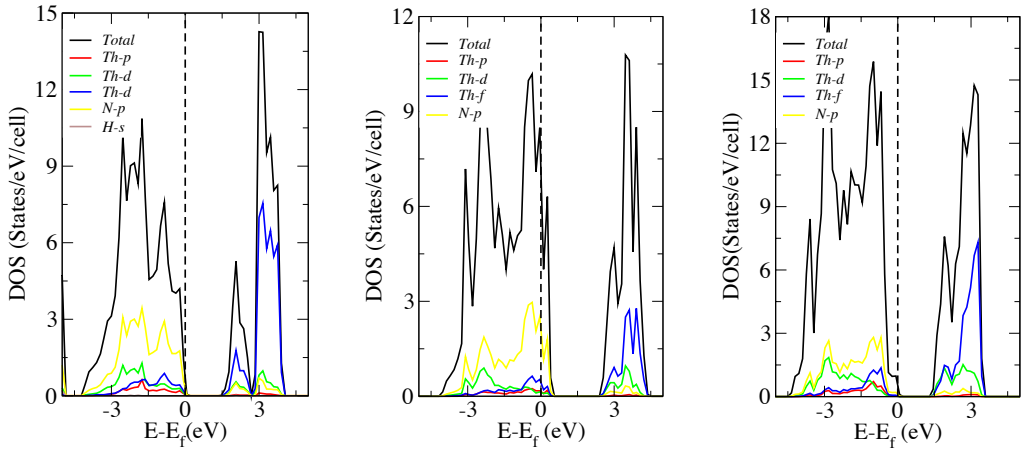

Figure 2: (Color online) The total and projected densities of states (DOS) for (a) $Th_2N_2(NH)$ (b) Th_2N_3 (c) Th_3N_4 within the description of the GGA. The Fermi energy level is set at zero and is represented using dashed line.

Of note in Figure 3a is the distortion in the charge density due to the presence of the -(NH) group that has resulted in a bean-shaped charge distribution compared to Figure 3b. This charge density bridge is attributed to the covalent bonding by this group to the ionic parent structure. [24, 10, 12]

4. Conclusions

In conclusion, the DFT technique has been used to study the structural, elastic and electronic properties of Th-N based compounds. This work is motivated by the physics of the thorium nitrides and the usefulness of various Th-N based compounds in the generation of energy. The inclusion of SP and SOC results in no significant change in the calculated properties of these compounds. We determined that Th-N based compounds are energetically and elastically stable. We observed that Th_3N_4 is the most energetically stable nitride. We found that Th_3N_4 and Th_2N_2NH are insulating, while Th_2N_3 is metallic. The insulating character of $Th_2N_2(NH)$ is attributed to covalent bonding of the -(NH) group to the otherwise ionic parent system. Generally, the calculated DOS show significant thorium d and f states hybridization with the nitrogen $2p$ in the Th-N based compounds.

Acknowledgment

The authors gratefully acknowledge financial support from the University of Pretoria. We thank Dr. Walter Meyer and Dr. Jannie Pretorius for assistance with the computational resources. KO gratefully acknowledges support of Dr. Molepo Mahlaga, Obodo T. Joshua and the members

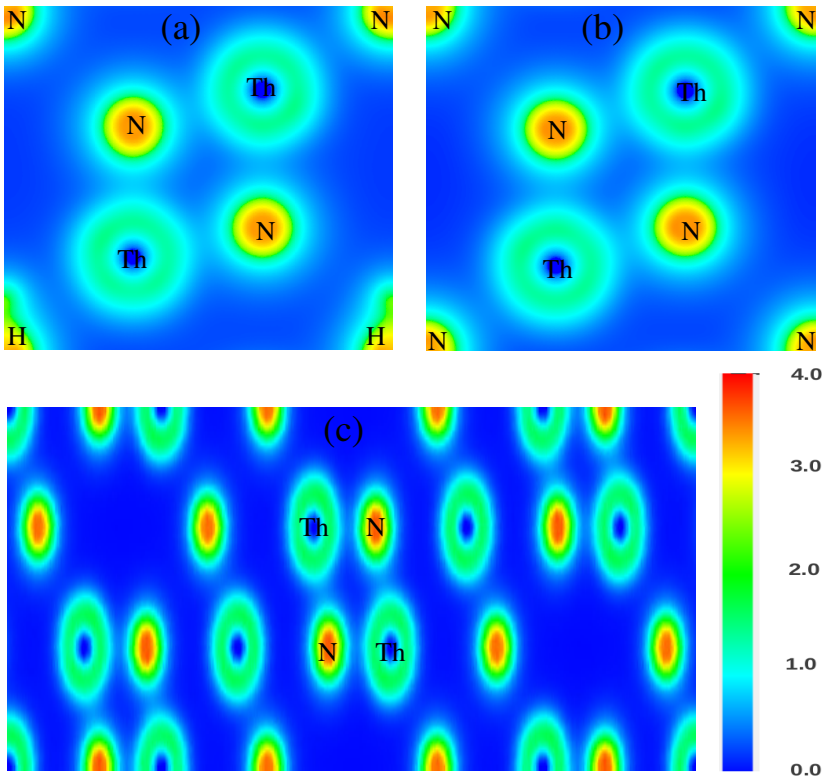

Figure 3: (Color online) Valence charge density distribution plots for (a) $Th_2N_2(NH)$ (b) Th_2N_3 (c) Th_3N_4 computed in the in the (110) plane. Charge density distribution for the atoms are labeled accordingly, and the scale is presented.

of the Theoretical and Computational Solid State Physics Research Group at the University of Pretoria for useful discussions.

References

[1] R Didchenko and F P Gortsema. Magnetic and Electric Properties of Monosulfides and Mononitrides of Thorium and Uranium. *Inorganic chemistry*, 2:1079–1080, 1963.

[2] S Aronson and A B Auskern. Vapor Pressure Measurements. *The Journal of Physical Chemistry*, 70(12):3937–3941, 1966.

[3] T Gouder, L Havela, L Black, F Wastin, J Rebizant, and Boulet P. Synthesis and electronic properties of ThN films. *Journal of Alloys and Compounds*, 336:73–76, April 2002.

[4] Ginger E Sigmon and Peter C Burns. Journal of Solid State Chemistry Crystal chemistry of thorium nitrates and chromates. *Journal of Solid State Chemistry*, 183(7):1604–1608, 2010.

[5] K.O. Obodo and N. Chetty. A theoretical study of thorium titanium-based alloys. *Journal of Nuclear Materials*, 440:229–235, May 2013.

[6] L GERWARD, J STAUN OLSEN, U. BENEDICT, J P ITIE, and J. C. SPIRLET. The Crystal Structure and the Equation of State of Thorium Nitride for Pressures up to 47 GPa. *Journal of Applied Crystallography*, 18:339–341, 1985.

[7] K Kurosaki, J Adachi, M Uno, and S Yamanaka. Molecular dynamics studies of actinide nitrides. *Journal of Nuclear Materials*, 344:45–49, September 2005.

[8] Raymond Atta-Fynn and Asok K. Ray. Density functional study of the actinide nitrides. *Physical Review B*, 76(11):115101(12), September 2007.

[9] I. R. Shein, K. I. Shein, N. I. Medvedeva, and a. L. Ivanovskii. Electronic structure and stability of thorium carbonitrides. *Physica Status Solidi (B)*, 244(9):3198–3205, September 2007.

[10] I.R. Shein and A.L. Ivanovskii. THORIUM COMPOUNDS WITH NON-METALS ELECTRONIC STRUCTURE, CHEMICAL BOND, AND PHYSICOCHEMICAL PROPERTIES. *Journal of Structural Chemistry*, 49(2):348–370, May 2008.

[11] G W Chinthaka Silva, Charles B Yeamans, Philppe F Weck, John D Hunn, Gary S Cerefice, Alfred P Sattelberger, and Ken R Czerwinski. Synthesis and characterization of Th2N2(NH) isomorphous to Th2N3. *Inorganic chemistry*, 51(5):3332–3340, March 2012.

[12] K O Obodo and N Chetty. GGA + U studies of the early actinide mononitrides and dinitrides. *Journal of Nuclear Materials*, 442(1-3), 235244, 2013.

[13] P. Hohenberg and W. Kohn. Inhomogeneous Electron Gas. *Physical Review*, 136(3B):B864–B871, 1964.

[14] G Kresse and J Furthmuller. Efficient iterative schemes for ab initio total-energy calculations using a plane-wave basis set . *Physical Review B*, 54(16):11169 (18), 1996.

[15] John P Perdew, Kieron Burke, and Matthias Ernzerhof. Generalized Gradient Approximation Made Simple. *Physical Review Letters*, 77(18):3865(4), 1996.

[16] Hendrik J Monkhorst and James D Pack. Special points for Brillouin-zone integration*. *Physical Review B*, 13(12):5188–5192, 1976.

[17] M. Methfessel and A. T. Paxton. Methfessel, Paxton - 1989 - High-precision sampling for Brillouin-zone integration in metals.pdf. *Physical Review B*, 40(6):3616–3620, 1989.

[18] Peter E. Blochl, O. Jepsen, and O. K. Andersen. Improved tetrahedron method for Brillouin-zine integrations.pdf. *Physical Review B*, 48(23):16223–16234, 1994.

[19] Yvon Le Page and Paul Saxe. Symmetry-general least-squares extraction of elastic data for strained materials from ab initio calculations of stress. *Physical Review B*, 65(10):104104(14), 2002.

[20] Orson L Anderson. A SIMPLIFIED METHOD FOR CALCULATING THE DEBYE TEPERATURE FROM ELASTIC CONSTANTS. *Journal of Physics and Chemistry of Solids*, 24:909–917, 1963.

[21] M. Uno, M. Katsura, and M. Miyake. Preparation of Th3N4 and its oxidation behaviour. *Journal of the Less Common Metals*, 135(1):25–38, October 1987.

[22] G W Chinthaka Silva, Philippe F Weck, Eunja Kim, Charles B Yeamans, Gary S Cerefice, Alfred P Sattelberger, and Kenneth R Czerwinski. Crystal and Electronic Structures of Neptunium Nitrides Synthesized Using a Fluoride Route. *Journal of The American Chemical Society*, 134:3111–3119, 2012.

[23] V L Moruzzi, J F Janak, and K Schwarz. Calculated thermal properties of metals. *Physical Review B*, 37(2):790–798, 1988.

[24] V. V. Bannikov, I. R. Shein, and a. L. Ivanovskii. Electronic structure, chemical bonding and elastic properties of the first thorium-containing nitride perovskite TaThN3. *physica status solidi (RRL) Rapid Research Letters*, 1(3):89–91, May 2007.

The next chapter presents results for the theoretical studies of thorium titanium alloys. This is motivated by the technological and scientific importance of thorium alloys and titanium alloys as demonstrated by their wide applications and vast scientific publications. Using DFT, the possibility of obtaining an ordered alloy of ThTi based system is investigated. The stability for the systems investigated is validated using arguments based on the bonding characters, enthalpy of formation, charge density distribution, electron localization function, elastic and lattice dynamic properties.

Chapter 4

A theoretical study of thorium titanium-based alloys

This section was published as[26] "Obodo, K. O. and Chetty, N. (2013). *A theoretical study of thorium titanium-based alloys.* Journal of Nuclear Materials, 440, 229 - 235."

A theoretical study of thorium titanium-based alloys

K. O. Obodo[1*] and N. Chetty[1,2†]

[1]*Physics Department, University of Pretoria, Pretoria 0002,*

South Africa; [2]*National Institute for Theoretical Physics, Johannesburg, 2000, South Africa*

Abstract

Using theoretical quantum chemical methods, we investigate the dearth of ordered alloys involving thorium and titanium. Whereas both these elements are known to alloy very readily with various other elements, for example with oxygen, current experimental data suggests that Th and Ti do not alloy very readily with each other. In this work, we consider a variety of ordered alloys at varying stoichiometries involving these elements within the framework of density functional theory using the generalized gradient approximation for the exchange and correlation functional. By probing the energetics, electronic, phonon and elastic properties of these systems, we confirm the scarcity of ordered alloys involving Th and Ti, since for a variety of reasons many of the systems that we considered were found to be unfavorable. However, our investigations resulted in one plausible ordered structure: We propose $ThTi_3$ in the Cr_3Si structure as a metastable ordered alloy.

I. INTRODUCTION

Thorium, a heavy metal, combined with various elements such as boron, carbon, nitrogen and oxygen has been studied both theoretically[1–3] and experimentally[4–6] in relation[2] to a range of physical, chemical, electronic, and thermophysical properties, often exhibiting high density, good thermal conductivity and good mechanical properties. The applications of Th-based alloys are wide-ranging. These include uses in nuclear reactors and in the aerospace industry because of its good corrosion resistant properties and high melting points. Th binary systems exist in various ordered alloys such thorium monocarbide (ThC),[7] mononitride (ThN)[8] and monoxide ThO.[9] ThO crystallizes in the rock salt structure, while ThO_2 crystallizes in the fluorite structure. ThB_4[10] and ThB_6 exist in the ThB_4 and CaB_6 structures.

Titanium, a relatively light metal is strong, has excellent corrosion resistant properties and a high melting point. Given its relatively small atomic size, Ti can be easily impregnated into materials without radically altering the host crystal structure. Therefore, Ti is a versatile element for alloying and modifying the properties - especially the strength properties - of materials. Applications range from additives in paints to metals for aerospace and industry. In this way, Ti is useful for engineering the properties of materials. Ti-based oxides are very well known, for example TiO_2 exists in the equilibrium rutile, and the metastable anatase and brookite structures, and the high pressure monclinic and orthorhombic forms. Ti also combines very readily with other metals, such as Pt in a variety of crystallographic forms and stoichiometries.

It would seem, then, that ordered alloys involving Th and Ti should form readily when in fact this is not the case. Experimental evidence by Carlson *et al.*[11]dating back to 1956 still appears to be the only authoritative view on this subject, although similar results were found by Pedersen *et al.* in 1980.[12] Carlson *et al.* discovered that Th-Ti forms a simple eutectic at 1190^{o}C and at 12 wt % Ti, with no intermediate phases. Pedersen *et al.* found the eutectic composition to be 13.26 wt % Ti. The solid phases at the eutectic are α-Th (cubic) and β-Ti (hexagonal). Carlson *et al.* concluded that solid solubilities at room temperatures are negligible. They argued that since the atomic radii of Th and Ti differ by about 22%, and because the Hume-Rothery rules for alloying suggest that extensive solid solubility should not occur between metals differing in size by more than 15%, the dearth of compounds (ordered or not) should not be surprising. Furthermore, they argued that since there is a marginal difference in the electronegativity of these two elements (the electronegativities are 1.3 for Th and 1.5 for Ti), compound phases should not form readily.

Since the authoritative experimental work done on these systems is more than fifty years old, and given the technological interest in both Th and Ti, and the potential scientific and technological interest in alloys involving these elements, we have investigated these alloy systems using modern theoretical quantum chemical methods, which over the past two decades has proven to be an excellent tool to study such systems for a variety of material properties.

In the next section we present a brief description of our theoretical and computational methodology. In Section III, we present analysis on various ordered alloys of Th-Ti based systems with the aim of investigating their stability. In Section IV, an in-depth analysis of the bonding and electronic character of our proposed stable alloy is presented. Finally, we present our conclusions in Section V.

II. METHODOLOGY

All calculations were performed using density functional theory[13] as implemented in the VASP code.[14] We used the PBE[15] and PBEsol exchange-correlation functional[16] for the generalized gradient approximation (GGA). A kinetic energy cutoff of 500 eV was chosen to ensure adequately converged total energies for the alloy systems under consideration. A Monkhorst-Pack[17] grid of 12×12×12 was used to sample the Brillouin zone (BZ) and Methfessel-Paxton smearing[18] with a width of 0.2 eV was used to integrate the bands to the Fermi level. The total energy, electronic band structure and density of states (DOS) were calculated using the tetrahedron integration method with Blöchl corrections.[19]

We tested our calculations with so-called Hubbard-U corrections of 1 eV for the onsite correlation energy, which for Th could in principle be important since it is an actinide. Our investigations showed that the differences in a range of results involving the physical structure, the electronic structure and the energetics over the conventional GGA approach were negligible. This, in hindsight, is not surprising since Th has a closed *f*-shell of electrons with no highly localized orbital. All results subsequently presented have not included the Hubbard correction.

A method using the least-squares fit,[20] as implemented in the MedeA-MT module, was used to obtain the elastic constants. This method uses the tetrahedron method for the Brillouin zone integrations. The elastic properties are calculated from the Hill value which is a geometric mean of the Voigt and Reuss values. The eigenvalues of the stiffness matrix gives an indication of the mechanical stability of the systems under consideration. The Hill values were used in the

estimation of longitudinal, shear and mean sound velocities, and the Debye temperatures.[21] The phonon dispersion curves and lattice dynamics were determined using linear response theory as implemented in the MedeA-PHONON package.

The heat of formation for each system was calculated by taking the difference between the total energy of the alloy unit cell and the sum of the energies of its constituents in their respective bulk elemental forms. The heat of formation of the system is strongly dependent on the spin-orbit coupling (SOC) due to the presence of relativistic effects in this heavy atomic systems.

Lu *et al.*[22] used the same method based on the elastic, valence charge density distribution and phonon dynamics to study ThN, which has been experimentally synthesized with an experimental lattice constant of 5.154 Å and bulk modulus of 175 GPa. This validates the approach used in this study. Therefore, we applied our methods to studies of pristine cubic Th and hexagonal Ti, and alloys of these elements in the Cr_3Si, Cu_3Au, Al_3Ti, CsCl, CuAu, CuPt, and NiAs crystal forms. For the off-50:50 compounds we considered both the alloy and its dual alloy, e.g. both Th_3Ti and $ThTi_3$ in the Cr_3Si structure.

III. INVESTIGATION OF STABILITY

The calculated elastic properties, phonon dispersion and heat of formation for thorium-titanium alloys is used to determine the elastically, dynamically and energetically stable alloys of Th-Ti based systems.

The GGA (PBEsol) exchange correlation functional is an improved functional that takes into account the interactions present in closely packed structures. Hence, it is largely used in this investigation to understand the properties of Th, Ti and Th-Ti based alloys. The results obtained using the GGA (PBEsol and PBE) for Th and Ti shows that the PBE[23] exchange-correlation functional gives a slightly improved description of the lattice constants for Th and Ti. But, there is no fundamental difference in the description of the electronic properties of Th-Ti based alloys except in the heat of formation were the PBEsol gives consistently lower heat of formation compared to the PBE functional. Hence the results presented for the elastic properties, the electronic properties and the phonon dispersion considers the non-magnetic (NM) structure of Th-Ti based alloys using PBEsol. However, the heat of formation is strongly dependent on the exchange correlation functional along with the presence of relativistic effects. Therefore, these issues are taken into account only for the proposed stable alloy.

The calculated lattice parameter using GGA (PBEsol) with the NM structure for Th (face centered cubic structure) is 4.95 Å, and Ti (hexagonal close pack structure) are a of 2.90 Å and c of 4.59 Å. The inclusion of SOC leads to a slight change in the lattice parameters of these systems. The calculated equilibrium lattice constants (a_0) for Th, Ti and Th-Ti based alloys is given in Table I for the NM cases. The lattice constants for Th-Ti based alloys in the NM phase shows there is an increase in the lattice constant with increase in Th concentration. This is expected because the Th atom is larger compared to Ti atom.

TABLE I. Lattice constant a_0 (Å), c (Å) and heat of formation (eV) of Th-Ti based alloys in various crystal structure using PBEsol in the non-magnetic phase

	a_0 (Å)	c (Å)	E_f (eV)
Th	4.95	4.95	–
$ThTi_3$ (Cr_3Si)	5.32	5.32	0.740
$ThTi_3$ (Cu_3Au)	4.28	4.28	0.683
$ThTi_3$ (Al_3Ti)	4.11	9.19	0.685
ThTi (CsCl)	3.60	3.60	0.433
ThTi (CuAu)	3.21	4.62	0.585
ThTi (CuPt)	3.25	15.54	0.773
ThTi (NiAs)	4.40	6.29	4.196
Th_3Ti (Cr_3Si)	6.05	6.05	2.514
Th_3Ti (Cu_3Au)	4.78	4.78	0.930
Th_3Ti (Al_3Ti)	4.60	10.27	0.336
Ti	2.90	4.59	–

The possibility of a magnetic ground state in Th-Ti based alloys is examined. For this purpose, the spin-polarized (SP) calculations, assuming an initial ferromagnetic ground state are carried out for the Th-Ti based alloys. We found that the ground state of all the Th-Ti based alloys considered is NM, without any localized atomic magnetic moments. The NM and SP calculations yield similar lattice parameters and lead to NM ground state structures for both PBE and PBEsol functionals. Subsequently, the inclusion of relativistic effects leads to a slight (insignificant) change in the lattice constant and a (significant) change in the heat of formation compared to the NM and SP cases for both GGA (PBE and PBEsol) functionals.

A. Elastic properties

The elastic properties of various ordered alloys of Th-Ti based systems are calculated for the NM phase. The elastic constants (c_{ij}) obtained are shown in Table II. The criteria for elastic stability are: positive elastic constants, positive bulk, shear and Young's moduli, positive shear velocity (obtained from the shear sound velocity), positive longitudinal velocity (obtained from the longitudinal sound velocity).[24] The systems that satisfy these criteria are elastically stable. However, this does not imply that such a system is dynamically stable. The negative elastic constant values for Th-Ti based alloy (in CuPt and NiAs structures) shows that these structures might be unstable because stability is related to sum rules.

TABLE II. Elastic constants C_{ij}'s (values in GPa)

	C_{11}	C_{12}	C_{13}	C_{14}	C_{33}	C_{44}	C_{66}
Th	69.55	52.54	52.24	–	69.55	49.32	49.32
$ThTi_3$ (Cr_3Si)	196.1	53.39	53.39	–	196.1	60.55	60.55
$ThTi_3$ (Cu_3Au)	122.2	77.94	77.94	–	122.2	39.64	39.64
$ThTi_3$ (Al_3Ti)	85.33	114.2	68.40	–	135.6	40.48	61.26
ThTi (CsCl)	105.0	67.23	67.23	–	105.0	9.020	9.020
ThTi (CuAu)	146.1	22.40	65.65	–	97.75	17.26	26.05
ThTi (CuPt)	135.9	42.39	57.15	−26.35	84.62	−4.750	–
ThTi (NiAs)	−1078	17.28	−396.8	–	157.4	–	–
Th_3Ti (Cr_3Si)	126.1	36.21	36.21	–	126.1	22.15	–
Th_3Ti (Cu_3Au)	91.85	58.40	58.40	–	91.85	45.24	45.24
Th_3Ti (Al_3Ti)	87.21	59.08	47.46	–	101.2	36.83	59.35
Ti	198.1	69.39	82.04	–	204.3	38.22	38.22

In Table III, we present the calculated bulk modulus of the various Th-Ti based alloys. The calculated bulk modulus for Ti, Th and $ThTi_3$ (in Cr_3Si structure) are 118.48 GPa, 58.21 GPa and 100.98 GPa respectively. Other alloys of Th-Ti based systems have lower bulk modulus compared to $ThTi_3$ (in Cr_3Si structure). $ThTi_3$ (in Al_3Ti structure) has the largest magnitude of shear modulus and Young's modulus compared to the other alloys. The mean velocity calculated from shear (transverse) velocity and longitudinal velocity is used to determine the Debye temperature. The

Debye temperature (θ_D) gives an indication of the stiffness of the material. $ThTi_3$ (Al_3Ti), Ti, $ThTi_3$ (in Cr_3Si structure) has θ_D of 445.0 K, 426.1 K, 346.7 K respectively. This shows that the alloying of Th with Ti leads to considerable improvement in the mechanical properties of Th metal.

TABLE III. The bulk, shear and Young's moduli (Hill values in GPa), acoustic velocities (ms^{-1}), and Debye temperature (K)

	B_H	G_H	Y_H	v_s	v_l	v_m	Θ_D
Th	58.21	24.94	64.72	1401	2684	1568	149.7
$ThTi_3$ (Cr_3Si)	100.9	64.65	159.8	2798	4760	3101	346.7
$ThTi_3$ (Cu_3Au)	92.70	31.38	84.58	1986	4112	2232	246.5
$ThTi_3$ (Al_3Ti)	89.80	108.7	207.7	3697	5432	4030	445.0
ThTi (CsCl)	79.82	12.19	34.79	1106	3106	1257	131.0
ThTi (CuAu)	77.45	24.81	67.16	1592	3360	1791	185.5
ThTi (CuPt)	73.19	−52.86	−430.0	–	–	–	–
ThTi (NiAs)	−484.0	929.3	39630	15670	14130	15090	1138
Th_3Ti (Cr_3Si)	66.17	29.52	77.07	1626	3073	1817	178.9
Th_3Ti (Cu_3Au)	69.55	30.37	79.41	1638	3118	1832	181.1
Th_3Ti (Al_3Ti)	64.84	31.24	80.63	1657	3060	1849	183.2
Ti	118.5	51.44	134.1	3257	6223	3643	426.1

B. Phonon dispersion

The phonon frequency of crystalline structures is one of the basic aspects when considering the phase stability, phase transformations, and the thermodynamics of these materials. The absence of imaginary (negative frequencies in the figures) frequencies in phonon dispersion curve and the phonon density of states give an indication that the structure is dynamically stable or vice versa. The phonon frequency for various Th-Ti based alloys in the NM phase using PBEsol is presented in Fig. 1. The use of PBE or PBEsol exchange correlation functional does not lead to a change in the lattice dynamics of these alloys. In Fig. 1a, 1b and 1c, the phonon plots of Th, Ti and $ThTi_3$ (in Cr_3Si structure) are shown respectively. They possess no imaginary phonon frequencies mode. Hence, they are structurally and thermodynamically stable. While, the other structures considered

have various degree of instabilities due to the presence of imaginary frequencies. The phonon frequencies for the unstable structures are presented for completeness.

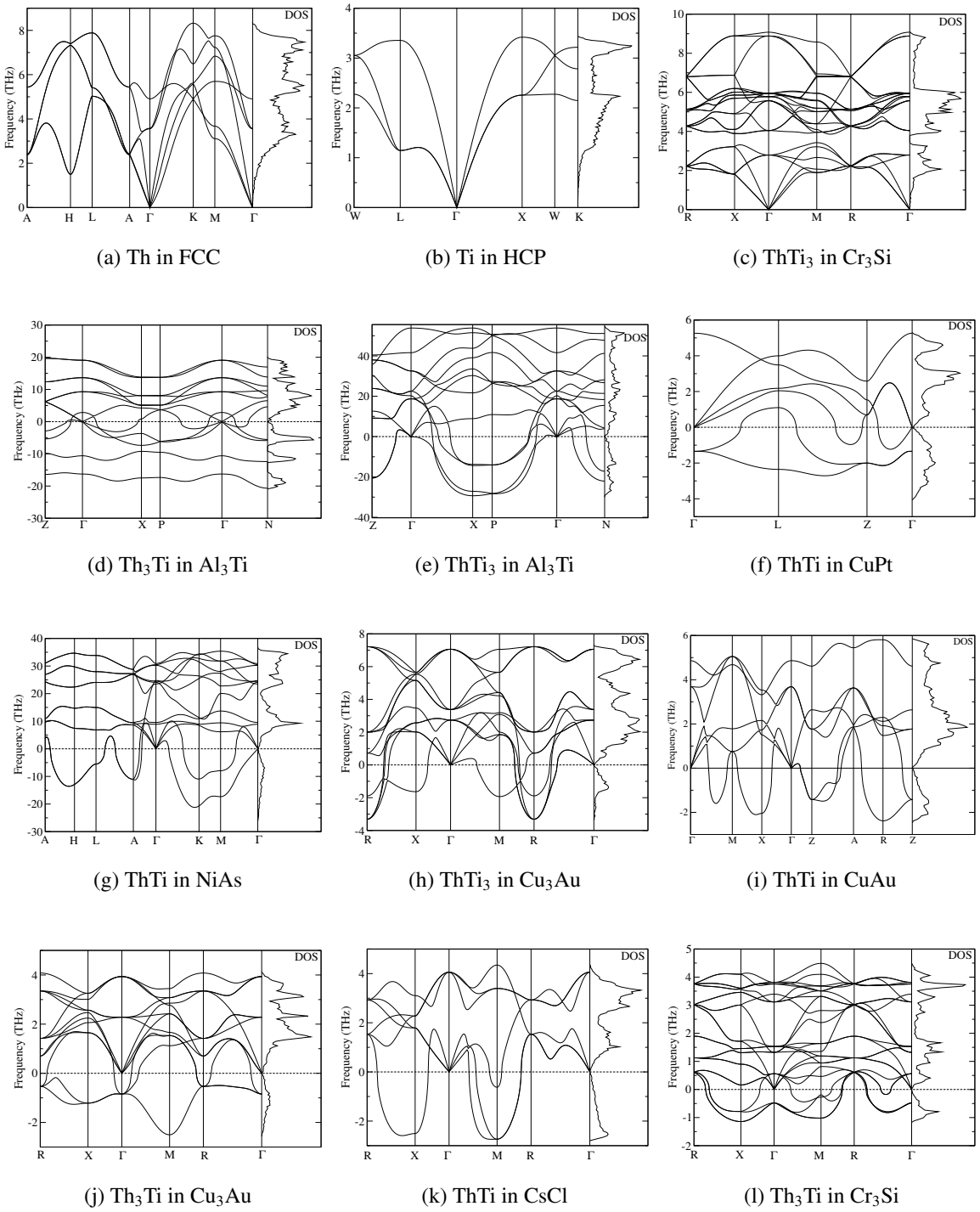

(a) Th in FCC (b) Ti in HCP (c) $ThTi_3$ in Cr_3Si

(d) Th_3Ti in Al_3Ti (e) $ThTi_3$ in Al_3Ti (f) ThTi in CuPt

(g) ThTi in NiAs (h) $ThTi_3$ in Cu_3Au (i) ThTi in CuAu

(j) Th_3Ti in Cu_3Au (k) ThTi in CsCl (l) Th_3Ti in Cr_3Si

FIG. 1. Phonon dispersion and phonon density of state (DOS) plots for Th, Ti and Th-Ti based alloys in various ordered crystalline structures

$ThTi_3$ (in Cu_3Au and in Al_3Ti structures) have the same ratio of atoms as $ThTi_3$ (in Cr_3Si structure). It is interesting to note that $ThTi_3$ (in Cu_3Au and in Al_3Ti structures) is stable at the Γ-point but possess few imaginary frequencies. This implies that the structure might transform to another structure or undergo pressure-induced stabilization. Therefore, these ordered structures with imaginary frequencies do not exist.

Isotropic pressure was applied to $ThTi_3$ (in Cu_3Au and in Al_3Ti structures) with the aim of stabilizing or transforming these structures to its stable form. These structures did not undergo any structural stabilization or phase transformation with change in pressure. This can be attributed to the size of the unit cell and the actual number of atoms.

In the same line, isotropic pressure is applied to the dual alloys of $ThTi_3$ (in Cu_3Au and in Al_3Ti structures) which is Th_3Ti (in Cu_3Au and in Al_3Ti structures). The phonon dispersion is evaluated to determine its stability. Pressure induced stabilization of these structures occurred for Th_3Ti (in Cu_3Au and in Al_3Ti structures) respectively. For Th_3Ti alloy (in Cu_3Au structure), a pressure of about 324.7 GPa is applied to the dynamically unstable structure to achieve a stable structure. Also Th_3Ti alloy (in Al_3Ti structure), a pressure of about -3.574 GPa was applied to the dynamically unstable structure to achieve a stable structure. The energies of formation of these pressure stabilized structures are positive and higher than that of $ThTi_3$ alloy (in Cr_3Si structure). Therefore, Th-Ti based alloys is most likely to be found as $ThTi_3$ (in Cr_3Si structure) rather than the pressure stabilized structures.

The phonon dispersion of $ThTi_3$ alloy (in Cr_3Si structure) has a splitting at Γ-point between the LO-TO, owing to the fact that Th atom is heavier than Ti atom. The low lying frequency modes are governed by the dynamics of heavy Th atoms, whereas the higher frequencies are governed by the dynamics of lighter Ti atoms.

C. Heat of formation

The Gibbs free energy of the various alloys is calculated. These calculations are performed at zero temperature and zero pressure, hence the Gibbs free energy reduces to the heat of formation, ΔH. The calculated heat of formation of the various alloys is investigated to determine its relative stability. Th and Ti metal are used as the reference systems to obtain the heat of formation for the alloys as described in the methodology. This is because they are the basic constituent of the alloy. The heat of formation for all the structures are presented in Table I for the NM phase with PBEsol

pseudopotential. The structure with the lowest heat of formation for the investigated Th-Ti based alloys using the PBEsol (with NM) is ThTi (in CsCl structure). This structure is highly elastically and dynamically unstable.

TABLE IV. The lattice constant a_0 (Å), exchange-correlation functional, method, heat of formation (eV) for Th, Ti and $ThTi_3$ (Cr_3Si) alloy using PBE and PBEsol. where non-magnetic, spin polarization and spin-orbit coupling is represented by NM, SP and SOC respectively

	a_0 (Å)	functional	method	E_f (eV)
$ThTi_3$ (Cr_3Si)	5.409	PBE	SOC	0.851
$ThTi_3$ (Cr_3Si)	5.406	PBE	SP	1.003
$ThTi_3$ (Cr_3Si)	5.406	PBE	NM	1.014
$ThTi_3$ (Cr_3Si)	5.322	PBEsol	SOC	0.591
$ThTi_3$ (Cr_3Si)	5.325	PBEsol	SP	0.727
$ThTi_3$ (Cr_3Si)	5.325	PBEsol	NM	0.740

To accurately determine the total energy and the heat of formation for the stable alloys the inclusion of SOC is essential for these alloys. We calculated the heat of formation for $ThTi_3$ alloy (in Cr_3Si structure) using the PBEsol functional with SOC to be 0.591 eV as listed in Table IV. Our calculated heat of formation for the system using PBEsol with SOC is less than NM and SP methods. In addition, using PBE functional with NM, SP and SOC method this results in a greater heat of formation compared to PBEsol with SOC. Generally, the inclusion of SOC leads to an effective lowering of the heat of formation in the structure for both GGA (PBE and PBEsol) functional.

The positive heat of formation of our system implies that the system will not occur spontaneously rather will require a positive energy input to create this alloy. The low value obtained for the heat of formation gives an indication that the formation of a metastable ordered alloy of Th and Ti is possible.

IV. THE PROPOSED METASTABLE ALLOY

The band structure, density of states, valence charge density distribution and electron localization function (ELF)[25–27] for the metastable system under consideration are presented to analyze

the electronic properties and bonding character.

The metastable alloy obtained from our investigation is $ThTi_3$ alloy (in Cr_3Si structure) as shown in Fig. 2. The alloy has the *Pm*-$\bar{3}$*n* space group (with group number 223). And the Th atoms in the unit cell are located in the (0.0, 0.0, 0.0) and (0.5, 0.5, 0.5) positions. The Ti atoms are located in the (0.5, 0.25, 0) and (0.5, 0.75, 0).

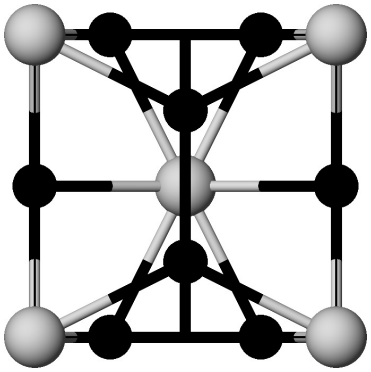

FIG. 2. The Structure of $ThTi_3$ in Cr_3Si where the white atoms represents Th atoms and the black atoms represents Ti atoms.

In Table IV, we present the GGA (PBE and PBEsol) results of the lattice parameter of the proposed metastable alloy. The difference in the lattice parameter obtained using PBE and PBEsol for the metastable system is about 1.6%. It should be mentioned here that $ThTi_3$ alloy (in Cr_3Si structure) irrespective of the initial magnetic configuration gives a NM ground state as previously stated for all Th-Ti based alloys. This is corroborated by the insignificant difference in the lattice parameters between the NM, SP and SOC phase of the structure.

A. Band structure and partial density of states

In Fig. 3, we present the calculated band structures for Th, Ti and $ThTi_3$ (in Cr_3Si structure) along the high symmetry lines of BZ, and this evidently shows that they are all metallic structures. Th and Ti metals are comprised of two groups of bands with a huge difference of about 200% between the Th and Ti valence bands. This difference in the valence bands suggests difficulty in bonding between these two metals. It is no surprise then that only one plausible structure is obtained from our investigation.

The band structure of $ThTi_3$ (in Cr_3Si structure) consists of three isolated groups of valence bands with a slight energy dispersion E(k), which is typical of crystals with a relatively low degree

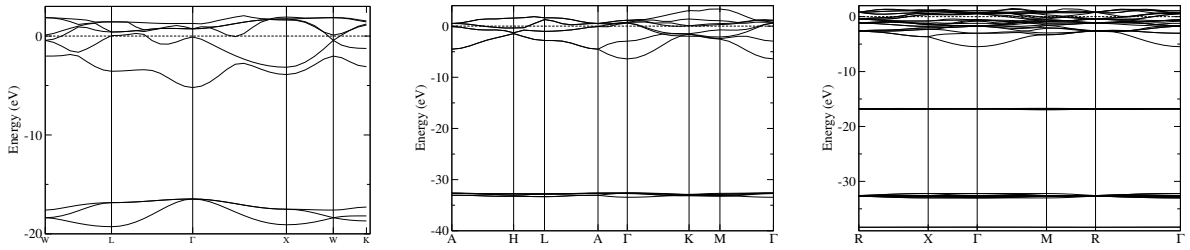

(a) Band Structure of Th (b) Band Structure of Ti (c) Band Structure of $ThTi_3$

FIG. 3. The band structure for Th, Ti and $ThTi_3$ alloy (in Cr_3Si structure) with the Fermi energy level set (dashed line) at zero.

of orbital hybridization.[28] The lowest group of band is from the Th *s*-orbital and is located around -38 eV. The following bands in Fig. 3c are from the Th *p*-orbital and are located around -21 eV and -15 eV with a slight contribution from the Ti *p*-orbital in later bands. These bands have a quasi-core character. The broadest occupied band is in the range of -5.5 eV to 1.5eV.

The PDOS for the metastable alloy is presented to highlight the effect of orbital hybridization around the Fermi level. The Th (*d* and *f*)-orbitals and the Ti (*p* and *d*)-orbitals are presented in PDOS for $ThTi_3$ (in Cr_3Si structure) in Fig 4. The most dominant contribution at the Fermi level is from the Ti *d*-orbital while, the Th (*d* and *f*)-orbitals provide almost equal contribution of states. The effect Ti *p*-orbital is marginal in determining the metallicity of $ThTi_3$ (in Cr_3Si structure). Looking at the contribution from Th, the dominant state in the conduction band is the Th *f*-orbital and in the valence band is the Th *d*-orbital. The system is very sensitive to the concentration of Ti atoms due to its overall contribution in determining the metallicity of the alloy. Hence, the configuration and concentration of Ti atoms will overall determine the electronic nature of this alloy.

B. Valence charge density

The computed valence charge density for $ThTi_3$ alloy (in Cr_3Si structure) is presented to elucidate the bonding character. Fig. 5 shows the computed charge density distribution plot for $ThTi_3$ alloy (in Cr_3Si structure) in the (100) plane. The valence charge density is indicated by the color scale on the side (blue is devoid of electrons and red has a high concentration of electrons). The valence charge densities plotted pertains to the valence states only summed over both spin direc-

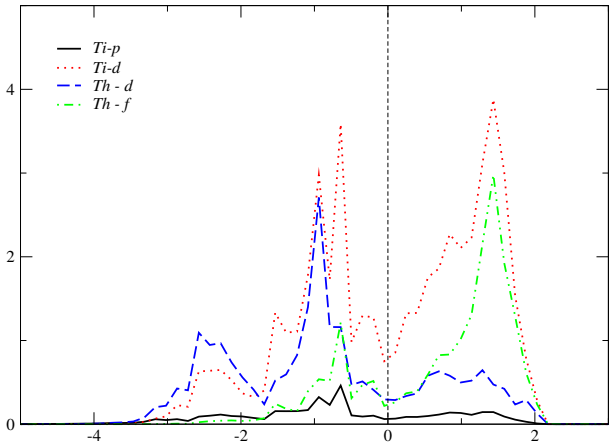

FIG. 4. (Color online) The partial density of states (PDOS) for $ThTi_3$ (in Cr_3Si structure). The DOS are calculated at the optimized geometry for the given density functional and magnetic ordering. The Fermi energy level is set at zero and is represented using dashed line.

tions.

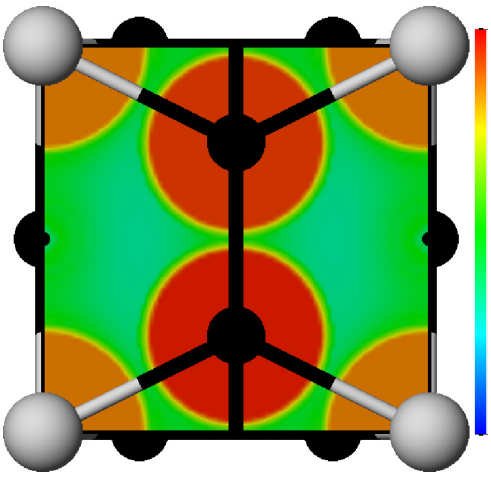

FIG. 5. (Color online) The valence charge density distribution for $ThTi_3$ (in Cr_3Si structure). The color pattern of the calculated valence charge density in the (001) plane, where the Th atom is depicted by the black balls and the Ti atoms by white balls.The color pattern of the valence charge density (scale: no electrons are represented as deep blue (0.0) and large concentration of electrons is represented as deep red (0.8); scale for remaining frames in increasing order of intensity: light blue, green, yellow, orange).

It is clearly seen that $ThTi_3$ alloy (in Cr_3Si structure) is metallic, characterized by a nearly spherical charge density distribution around the Th and Ti ions with very high concentration of

valence charge and an appreciable charge density in all the interstitial regions. Hence, in **k**-space, appreciable band overlap exists between Th and Ti ions. Compared to the charge density in the rest of the interstitial region relatively high charge density bridges are present between the atomic spheres. This indicates ionization in the bridge sites suggestive of the presence of covalency.

In order to ascertain the presence of covalency in all of the bridge sites, we calculated the distribution of the ELF.

C. Electron localization function for $ThTi_3$ (in Cr_3Si structure)

The ELF for the ground state bonding configuration of $ThTi_3$ alloy in (Cr_3Si structure) is evaluated to gain further insight into its bonding character and nature. ELF is given as $[1 + (D/D_h)^2]^{-1}$, D is $\tau - t_W$ represents an excess of the local kinetic energy due to the Pauli principle. Where $\tau = \frac{1}{2}\sum|\nabla\varphi_i|^2$ is the Kohn-Sham local kinetic energy, φ_i are the Kohn-Sham orbitals, and t_W is the value of τ in the absence of the Pauli principle ($\sim |\nabla\rho|^2/\rho$ and ρ being the charge density). D_h being D for the corresponding uniform electron gas ($\sim \rho^{5/3}$). The spatial organization of ELF provides a basis for a proper classification of bonds[27,29]. Based on this definition ELF takes values ranging from 0 and 1, where 1 represents perfect localization. The Th metal has more valence and core electrons than the Ti metal. They both exhibit similar features such as the large concentration of electrons around the atoms and an appreciable density of electrons away from the atoms (non-directional), which is consistent with metallic bonding. In Fig. 6 the ELF is shown for the same plane as considered above for the valence charge-density distribution. Both picture are quite similar, with almost spherical shapes of the ELF around the Th atoms and a lower localization of the electrons on Ti atoms. Remarkably, the concentration of electrons between the Th and Ti bridges has a region of electron depletion compared to the Ti and Ti bridges. This observation gives an insight that the slight covalent character observed is from Ti atoms, which has a shared-electron pair. Hence, this particular crystal structure with more number of Ti atoms is stable compared to the corresponding structure (Th_3Ti alloy in (Cr_3Si structure) with more Th atoms.

Based on these observations, the $ThTi_3$ alloy in (Cr_3Si structure) is predominantly metallic.

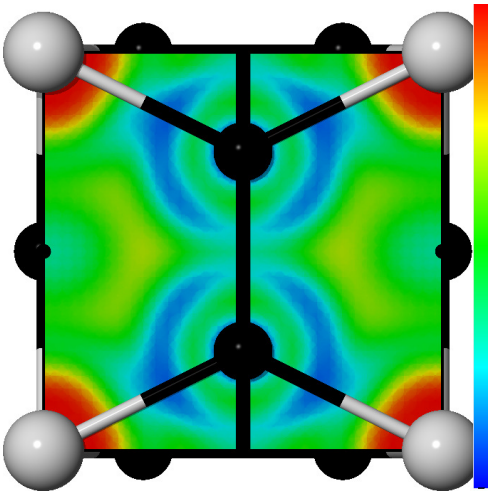

FIG. 6. (Color online) The electron localization function for $ThTi_3$ (in Cr_3Si structure). The color pattern of the calculated electron charge density in the (001) plane, where the Th atom is depicted by the black balls and the Ti atoms by white balls.The color pattern of the ELF (scale: no electrons are represented as deep blue (0.0) and large concentration of electrons is represented as deep red (0.1); scale for remaining frames in increasing order of intensity: light blue, green, yellow, orange).

V. CONCLUSIONS

This work is motivated by the usefulness of various alloys of Th and Ti, hence the search for the possibility of ordered alloys involving Th and Ti. We considered a number of different structures and stoichiometries involving these elements. A predicted metastable structure was established using arguments based on elastic constants, phonon frequencies, electron localization function, valence charge density, band structure, density of states and heat of formation.

The calculated phonon frequencies and elastic constants shows that $ThTi_3$ (in Cr_3Si structure) is dynamically stable at zero Kelvin and zero pressure as indicated by their positive values. This system using PBESol with the inclusion of SOC is energetically more favorable and gives an appropriate description with a heat of formation of 0.591 eV compared with to the other methods. Though stabilization of some systems where achieved via pressure, the heat of formation of these systems are less favorable compared to $ThTi_3$ (in Cr_3Si structure). We propose $ThTi_3$ (in Cr_3Si structure) as a plausible metastable ordered alloy of Th-Ti based systems.

This should stimulate experimental efforts to synthesize this material.

ACKNOWLEDGMENTS

We are grateful to the University of Pretoria for financial support. We thank Dr. Walter Meyer and Dr. Jannie Pretorius for assistance with the computational resources. Also we acknowledge Prof Richard Martin for assistance and the members of Theoretical and Computational Solid State Research Group at the University of Pretoria for useful discussions.

---

* Kingsley.Obodo@up.ac.za, 0027788489678

† Nithaya.Chetty@up.ac.za

[1] I. Shein, K. Shein, and A. Ivanovskii, "First-principle study of B1-like thorium carbide, nitride and oxide," *Journal of Nuclear Materials*, vol. 353, pp. 19–26, July 2006.

[2] I. Shein and A. Ivanovskii, "THORIUM COMPOUNDS WITH NON-METALS ELECTRONIC STRUCTURE, CHEMICAL BOND, AND PHYSICOCHEMICAL PROPERTIES," *Journal of Structural Chemistry*, vol. 49, pp. 348–370, May 2008.

[3] J. Adachi, K. Kurosaki, M. Uno, and S. Yamanaka, "A molecular dynamics study of thorium nitride," *Journal of Alloys and Compounds*, vol. 394, pp. 312–316, May 2005.

[4] W. R. Evans, S. C. Barton, M. Clemens, and D. D. Allred, "Understanding DC-bias sputtered thorium oxide thin films useful in EUV optics," *Proceedings of SPIE*, vol. 5, no. 1, pp. 631711–631711–12, 2006.

[5] T. Gouder, L. Havela, L. Black, F. Wastin, J. Rebizant, and B. P, "Synthesis and electronic properties of ThN films," *Journal of Alloys and Compounds*, vol. 336, pp. 73–76, Apr. 2002.

[6] S. Mahmoud, "Characterization of thorium dioxide thin films prepared by the spray pyrolysis technique," *Solid State Sciences*, vol. 4, pp. 221–228, Feb. 2002.

[7] H. Kleykamp, *Gmelin handbook of inorganic and organometallic chemistry: Th, Thorium. Thorium carbides*. Gmelin handbook of inorganic chemistry, Springer, Berlin, 1992.

[8] R. Benz, A. Naoumidis, L. Gmelin, and D. Brown, *Gmelin handbook of inorganic chemistry, 8th edition: Th : thorium. Compounds with nitrogen*. No. no. 44, v. 3 in Gmelin handbook of inorganic chemistry, Springer-Verlag, 1987.

[9] C. Keller, *Gmelin Handbuch der Anorganischen Chemie, Thorium. Ternare and polynare Oxide des Thotiums*. Gmelin Handbuch der Anorganischen Chemie, Springer, Berlin-Heidelberg-New York, 1976.

[10] D. Brown and H. Wedemayer, *Gmelin handbook of inorganic and organometallic chemistry: Th, Thorium. Compounds with S, Se, Te and B.* Gmelin handbook of inorganic chemistry and Organometallic Chemistry, Springer, Berlin, 1993.

[11] O. N. Carlson, J. M. Dickinson, H. E. Lunt, and H. A. Wilhem, "Thorium-Columbium and Thorium-Titanium Alloys Systems," *Transactions AIME*, vol. 206, pp. 132–136, Feb. 1956.

[12] E. T. Pedersen, M. Noack, and D. J. Verhoeven, "Eutectic alloys of thorium-nobium and thorium-titanium," *Journal of Materials Science*, vol. 15, pp. 2115–2117, Sept. 1980.

[13] P. Hohenberg and W. Kohn, "Inhomogeneous Electron Gas," *Physical Review*, vol. 136, no. 3B, p. 864, 1964.

[14] G. Kresse and J. Furthmüller, "Efficient iterative schemes for ab initio total-energy calculations using a plane-wave basis set," *Physical Review B*, vol. 54, p. 11169, Oct. 1996.

[15] J. P. Perdew, K. Burke, and M. Ernzerhof, "Generalized Gradient Approximation Made Simple.," *Physical review letters*, vol. 77, p. 3865, Oct. 1996.

[16] J. P. Perdew, A. Ruzsinszky, G. I. Csonka, O. A. Vydrov, G. E. Scuseria, L. A. Constantin, X. Zhou, and K. Burke, "Restoring the Density-Gradient Expansion for Exchange in Solids and Surfaces," *Physical Review Letters*, vol. 100, p. 136406, Apr. 2008.

[17] H. J. Monkhorst and J. D. Pack, "Special points for Brillouin-zone integrations," *Physical Review B*, vol. 13, no. 12, p. 5188, 1976.

[18] M. Methfessel and A. T. Paxton, "High-precision sampling for Brillouin-zone integration in metals," *Physical Review B*, vol. 40, no. 6, p. 3616, 1989.

[19] P. E. Blöchl, O. Jepsen, and O. K. Andersen, "Improved tetrahedron method for Brillouin-zine integrations," *Physical Review B*, vol. 49, no. 23, p. 16223, 1994.

[20] Y. Le Page and P. Saxe, "Symmetry-general least-squares extraction of elastic data for strained materials from *ab initio* calculations of stress," *Physical Review B*, vol. 65, p. 104104, Feb. 2002.

[21] O. L. Anderson, "A Smplified Method for Calculating the Debye Temperature from Elastic Constants," *Journal of Physics: Chemucak Solids*, vol. 24, pp. 909–917, 1963.

[22] Yong Lu, Da-Fang Li, Bao-Tian Wang, Rong-Wu Li, and Ping Zhang. Electronic structures, mechanical and thermodynamic properties of ThN from first-principles calculations. *Journal of Nuclear Materials*, 408:136–141, January 2011.

[23] P. Soderlind, O. Eriksson, and B. Johansson, J. M. Wills "Electronic properties of f metals using the generalized gradient approximation," *Physical Review B*, vol. 50, no. 11, pp. 7291–7294, 1994.

[24] V. L. Moruzzi, J. F. Janak, and K. Schwarz, "Calculated thermal properties of metals," *Physical Review B*, vol. 37, no. 2, pp. 790–798, 1988.

[25] A. D. Becke and K. E. Edgecombe, "A simple measure of electron localization in atomic and molecular systems," *The Journal of chemical physics*, vol. 92, no. 9, pp. 5397–5403, 1990. Cited By (since 1996): 1408.

[26] A. Savin, A. D. Becke, J. Flad, R. Nesper, H. Preuss, and H. G. von Schnering, "A New Look at Electron Localization," *Angewandte Chemie International Edition in English*, vol. 30, pp. 409–412, Apr. 1991.

[27] B. Silvi and A. Savin, "Classification of chemical bonds based on topological analysis of electron localization functions," *Nature*, vol. 371, no. 6499, pp. 683–686, 1994. Cited By (since 1996): 998.

[28] K. I. Shein, I. R. Shein, N. I. Medvedeva, V. G. Bamburov, and a. L. Ivanovskii, "Electronic structure of tetragonal thorium silicate in comparison with thorium dioxide," *Doklady Physical Chemistry*, vol. 409, pp. 198–201, July 2006.

[29] N. V. Skorodumova, R. Ahuja, S. I. Simak, I. A. Abrikosov, B. Johansson, and B. I. Lundqvist, "Electronic, bonding, and optical properties of CeO2 and Ce2O3 from first principles," *Physical Review B*, vol. 64, pp.115108, Aug. 2001.

This concludes the studies on actinide compounds with out the inclusion of the Hubbard U parameter. The next chapter explores the significance of the Hubbard U parameter in the proper description of actinide system. A case study of Pa and its oxides is presented.

Chapter 5

First principles LDA + U and GGA + U study of protactinium and protactinium oxides: dependence on the effective U parameter

This section was published as[29] "Obodo, K. O. and Chetty, N. (2013). *First principles LDA + U and GGA + U study of protactinium and protactinium oxides: dependence on the effective U parameter.* Journal of Physics: Condensed Matter, 25, 145603(12)."

First principles LDA + *U* and GGA + *U* study of protactinium and protactinium oxides: dependence on the effective *U* parameter

K. O. Obodo[1*] and N. Chetty[1,2†]

[1]*Physics Department, University of Pretoria, Pretoria 0002, South Africa;* [2]*National Institute for Theoretical Physics,Johannesburg, 2000, South Africa*

(Dated: July 27, 2013)

Abstract

The electronic structure and properties of protactinium and its oxides (PaO and PaO_2) have been studied within the framework of the LDA, GGA(PBE), LDA + *U* and GGA(PBE) + *U* implementations of density functional theory. The dependence of selected observables of these materials on the effective *U* parameter has been investigated in detail. The examined properties include lattice constants, bulk moduli, effect of charge density distributions, the hybridization of the 5*f* orbital and the energy of formation for PaO and PaO_2. The LDA gives better agreement with experiment for the bulk modulus than the GGA for the Pa but GGA give better structural properties. We obtained that PaO is metallic and PaO_2 is a Mott-Hubbard insulator. This is consistent with observations for the other actinide oxides. We discover that GGA and LDA incorrectly give metallic behavior for PaO_2. The GGA(PBE) + *U* calculated indirect band gap of 3.48 eV reported for PaO_2 is a prediction and should stimulate further studies of this material.

PACS numbers: 61.48.Gh, 68.35.bg, 73.22.Pr

I. INTRODUCTION

Protactinium is the first element in the actinide series with a 5*f* electron.[1] In some systems (PaO_2, UO_2, NpO_2, PuO_2), the presence of 5*f* electrons leads to an improper description of the electronic and the structural properties by DFT.[2–7] Several approaches have been developed to overcome these shortcomings of DFT such as the self-interaction correction (SIC), DFT hybrid approach, DFT + *U*, GW etc. The DFT + *U* (LDA + *U* and GGA + *U*) approach has been shown to effectively correct many of the deficiencies observed by this class of materials with regards to the band gap.[8–10] This approach introduces an on-site Hubbard *U* and the Hund's *J*. Dudarev *et al.*[11] combined these two terms in the rotationally invariant formalism to a single term U_{eff}=*U*−*J*, referred to as the simplified LSDA + *U*. The introduction of this *adhoc* parameter leads to a significant improvement in the description of some 5*f* systems where DFT fails but the choice of the value of this parameter is debatable. The U_{eff} parameter can be obtained: (i) from constrained LDA approach,[8] (ii) from constrained RPA,[12] (iii) from a self-consistent approach,[13] and (iv) from fitting the parameter to experimental observables.[14]

Pa and its oxide are used in scintillators for detecting X-rays, for radioactive dating (determination of ancient artifact), in cathode ray tubes with bright green fluorescence, as high temperature dielectrics for ceramic capacitors, in nuclear weapons (used as support in nuclear chain reactions), etc.[15] These materials have downsides which has limited its study, namely (i) the high toxicity and radioactive nature and (ii) the limited availability. These materials are mainly found as a by-product in nuclear reactions. Furthermore, these materials are (iii) strongly correlated, giving rise to failures by conventional DFT methods.

The understanding of the electronic and structural properties is paramount to harness and control these materials optimally. The elements in the 5*f* series with localized electrons possess greater atomic volumes and symmetrical structures compared to those with itinerant electrons.[16,17] Hence, Pa exists in the bct, fcc and orthorhombic (α-U) phase at standard temperature and pressure (STP), high temperature and high pressure respectively. Pa metal possesses itinerant 5*f* electrons with characteristic properties such as superconducting and high vaporization.[15,18,19]

There has been significant interest in the understanding of Pa metal,[20] due to its unique behavior as the first element with a 5*f* electron. The effect of pressure induced phase transitions has been explored theoretically and experimentally. Haire *et al.*[21] experimentally showed that Pa metal undergoes a pressure induced structural phase transition at 77 GPa from the bct structure (space

group *I4/mmm*) to an orthorhombic, α-U structure (space group *Cmcm*) with ~ 30% atomic volume reduction and no subsequent phase transition. This was predicted by theoretical studies,[16,22] which attribute this to the increase in 5*f* electron participation in the bonding.

The studies of protactinium oxides (PaO and PaO_2) have been limited to the mode of synthesis and purification for the production of Pa metal.[15] Prodan *et al.*[23] used the density functional hybrid approach to study actinide dioxides and obtained a band gap of 1.4 eV for PaO_2. To the best of our knowledge, no further studies have been performed to shed more light on the electronic structure of PaO_2. Hence, a proper description of the electronic and structural properties of these oxides within the DFT and DFT + *U* methods is appropriate to understand the physics of these materials.

A systematic first principles study of the dependence of the effective Hubbard-*U* parameter on LDA + *U* and GGA + *U* functionals in Pa and its oxides is lacking. In this work, the DFT methodology is applied to calculate the electronic and structural properties of Pa metal. Using a semi-empirical fit, we then optimize the Hubbard *U* parameter to give a proper description of PaO and PaO_2. The structural and electronic properties of these oxide materials are determined to investigate the role played by the *5f* electrons.

In Section II, a brief description of the theoretical and computational methodologies is presented. In Section III, the results and discussions for Pa and its oxides are presented, followed by the conclusions in Section IV.

II. THEORY AND COMPUTATIONAL DETAILS

All calculations were performed using density functional theory[24] as implemented in the VASP code.[25] The electron wave functions were described using the projector augmented wave (PAW) method of Blöchl in the implementation of Kresse and Joubert.[26] The LDA[27] and PBE[28] form of the GGA exchange-correlation potentials were used together with their LDA + *U* and GGA + *U* variants. An adequately converged kinetic energy cutoff of 500 eV, 500 eV, 550 eV was chosen to ensure fully converged total energies for Pa, PaO and PaO_2 respectively. A spacing of **k**-points of 0.2/Å fine mesh for the Monkhorst-Pack[29] grid is used to sample the Brillouin zone, and Methfessel-Paxton smearing[30] with a width of 0.2 eV was used to integrate the bands at the Fermi level. The total energy, electronic band structure and density of states (DOS) were calculated using the tetrahedron integration method with Blöchl corrections.

Subsequently, we introduce the Hubbard *U* parameter for the onsite interaction strength. The

U parameter was computed by optimizing the lattice parameter with respect to U. This resulted in differences for a range of results involving the physical structure, the electronic structure and the energetics within the GGA and LDA schemes for the oxides. Results presented in this work uses LSDA, GGA, LSDA + U and GGA + U for the oxides but without the U parameter for Pa atom.

TABLE I: Partial $5f$ occupation for Pa, PaO and PaO_2 systems using GGA with SOC.

System	U	$5f$
Pa	0	1.327
PaO	2.5	1.228
PaO_2	2	1.414

A method using the least-squares fit,[31] as implemented in the MedeA-MT module, was used to obtain the elastic constants. This uses the tetrahedron method for the Brillouin zone integrations. The elastic properties were calculated from the Hill values which are a geometric mean of the Voigt and Reuss values. The eigenvalues of the stiffness matrix gives an indication of the mechanical stability of the systems under consideration, which is used to obtain the elastic constants. The Hill values[32] were used in the estimation of longitudinal, shear and mean sound velocities, and the Debye temperatures.[33]

The energy of formation for each structure was calculated by taking the difference between the total energy of the compound (PaO_n) and the energies of its constituents in their corresponding bulk forms:

$$\Delta H_f = E^{tot}_{(PaO_n)} - N_{Pa}\, E^{bulk}_{(Pa)} - N_O\, E^{bulk}_{(O)}\,, \tag{1}$$

where n is either 1 or 2, N_{Pa} and N_O are the number of Pa atoms and O atoms in the PaO_n compound respectively, $E^{bulk}_{(Pa)}$ is the energy per Pa atom in the bct phase, and $E^{bulk}_{(O)}$ is the energy per O atom in the oxygen molecule.

The phonon calculations were done using the general direct approach of lattice dynamics as implemented in the MedeA-PHONON package.[34]

III. RESULTS AND DISCUSSION

A. Preamble

We carried out self consistent calculations to determine the ground states of Pa and its oxides using spin-polarized (SP) and spin-orbit coupling (SOC) within the DFT + U approach. The inclusion of the effective Hubbard U is excluded for Pa metal because DFT gives a reasonable description of the metal.[16] Pa element is a heavy metal with an atomic number of 91, hence relativistic effects are important. In order to account for the relativistic effects in these systems, the inclusion of SOC is important. In this study, we have shown that in order to obtain the correct properties of PaO_2, the effect of SOC has to be taken into account.

The U parameter in this study is optimized with respect to the lattice constant. The U parameter obtained is used to calculate the structural and electronic properties of the systems. This gives a qualitatively and quantitatively better description of the properties of PaO and PaO_2.

The U parameter accounts for the onsite Coulomb interaction which leads to the localization of the 5f electrons in these systems. In contrast, the standard DFT fails to account for the localization of the electrons, but leads to the delocalization which is a consequence of the Pauli-exclusion principle. The localization of the 5f orbitals leads to a non-magnetic (NM) insulating ground state for PaO_2 but does not change PaO from metallic to insulating.

In order to obtain the correct ground state for PaO_2 for a given U parameter, we lifted the symmetry constraints in the calculations of the electronic and the structural properties allowing the systems to evolve and explore all of phase space, i.e. all stable and metastable phases, including magnetic phases. This has an effect of significantly increasing the computational time as all **k**-points in the Brillouin zone are treated independently, i.e. the special **k**-point set is not reduced by symmetry.

Gryaznov *et al.*,[35] studied UN, UO_2 and PuO_2 with the inclusion of SOC and showed that to correctly describe these systems the lifting of symmetry constraints is absolutely essential. There have been various methodologies proposed by different authors on how to achieve the true ground state within the DFT + U formalism including SOC, such as monitoring the occupation matrix,[36] ramping the Hubbard U parameter,[37] etc. In this study, the symmetry constraints are lifted and the correct ground state is obtained for PaO_2 within the SOC scheme for all the values of U considered. In our work, the symmetry constraints are lifted and the correct ground state is obtained for PaO_2

within the SOC. However, the SP does not yield the correct ground state because relativistic effects are unaccounted for.

B. Crystal structures

Fig. 1 shows the conventional unit cells of Pa, PaO and PaO_2.

Pa has three crystallographic forms which are (i) the body centered tetragonal structure (bct) at STP which transforms to (ii) the face centered cubic structure (fcc) at elevated temperature, and which undergoes a pressure-induced structural transformation to the (iii) α-Uranium structure. The Pa (bct) phase is presented in Fig. 1a.

In Fig. 1b, we present the PaO system which crystallizes in the NaCl structure.

PaO_2 contains antiferromagnetically (AFM) ordered Pa atoms with an underlying fluorite structure that leads to a double tetragonal unit cell (with $c = \sqrt{a}$) when the magnetic ordering is taken into account. The AFM ordered structure is shown in Fig. 1c, where the magnetic ordering is in the z-axis.

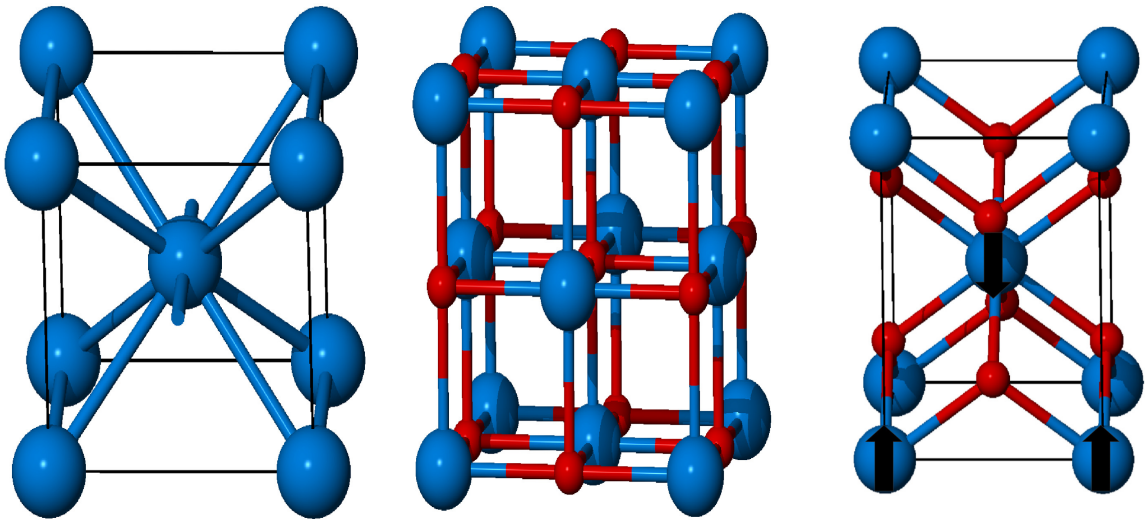

(a) Pa (b) PaO (c) PaO_2

FIG. 1: (Color online) The crystallographic unit cells of (a) Pa, (b) PaO (c) PaO_2. Blue spheres depict Pa and the red spheres depict the oxygen atoms. The black arrows illustrate the AFM ordering in the z-axis

C. Structural properties

As indicated earlier, Pa has been observed to exist in various different phases. The STP phase which is the bct structure has experimental lattice parameters of a_0 = 3.925 Å and c = 3.238 Å.[21] LDA is known to underestimate the lattice parameter while GGA generally overestimates the lattice parameter. However, in the early actinides lattice constants obtained using the GGA are found to be better corroborated with experiment compared with the LDA.[38] In Table II, we show our calculated values of the lattice parameters obtained using the GGA and the LDA within the SOC and the SP schemes. Upon complete optimization, the system evolves to a NM ground state consistent with experiment. The lattice parameter, density and volume obtained within the GGA approximation are more comparable to experiment than LDA. As far as the structural properties are concerned, the extension of our methodology to include the Hubbard U parameter is not necessary in the case of metallic Pa.

In Fig. 2, we present the calculated lattice parameter of PaO as a function of the U parameter, where the dotted line indicates the experimental value of a_0. The variation of the lattice parameter is a monotonically increasing function with respect to the U parameter within the SOC and SP scheme. At U= 2.5 eV, the GGA + U (SOC and SP scheme) yields the experimental lattice parameter for PaO. The corresponding result using the LDA + U (SOC and SP scheme) significantly underestimates the lattice parameter. Increasing U to a value of 5.5 eV still does not give a sufficiently accurate result for the lattice parameter within the LDA + U scheme. This shows that the use of the U parameter is better suited within GGA than LDA in the present case. Since a value for U that is too large pushes the f orbitals too far down into the O$2p$ based levels.[39] At U= 0 eV, PaO (within SOC scheme) results in a magnetic ground state. This system evolves with the increase of the U parameter to a NM metallic ground state. This observation is similar to the SP case for the GGA + U. LDA + U gives a NM metallic ground state at all values of the U parameter.

The PaO_2 structure is fully geometrically optimized using the SP and SP + SOC (hence forth referred to as SOC) within the DFT + U. The inclusion of SOC in the fluorite structure of PaO_2 without SP does not transform the structure to the AFM ordered state similar to UO_2. Rather, the inclusion of SP does yield structures which are AFM ordered leading to the symmetry breaking for the PaO_2. For consistency, the structure used in the study is the tetragonally distorted structure obtained when the PaO_2 is in the AFM ordered state. In Fig. 3, the calculated lattice parameter as a function of the U parameter is presented where the dotted line indicates the experimental value.

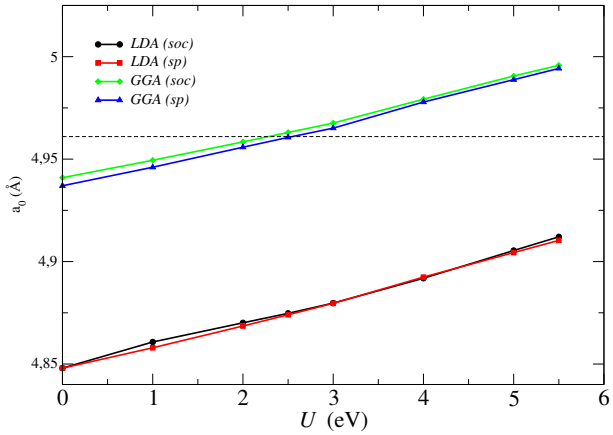

FIG. 2: (Color online) The change in the lattice parameters is plotted within the description of DFT + U (GGA, LDA) approximations for PaO. The U - parameter results in a significant change in the structural parameters.

The variation of the lattice parameter is a monotonically increasing function with respect to the U parameter within the SOC and SP schemes. Fig. 3a and 3b shows the variation of a_0 and c_0 respectively as a function of the U parameter. For U = 4.0 eV, the LDA + U with SOC yields a reasonable lattice parameter (5.501 Å) which is approximately equal to the experimental value (5.509 Å), compared to the LDA + U with SP, which grossly underestimates lattice parameter. On the other hand, for U = 2.0 eV, the GGA + U with SOC gives a slightly higher (about 0.8 %) lattice parameter for PaO_2 and only slightly underestimates (about −1.01 %) the lattice parameter using the SP scheme. With this value for U we go on to evaluate all further properties of interest for this PaO2.

Our conclusions for PaO_2 about the accuracy of GGA over LDA within the DFT + U schemes are similar to those for PaO.

D. Elastic properties

We find Pa to be elastically stable due to the absence of negative elastic constants. In Table II, we present the theoretical and experimental bulk modulus for Pa. There are discrepancies between previously reported theoretical[38] and experimental[40,41] values for the bulk modulus of Pa. In these previous studies, the value of the experimental bulk modulus obtained was found to be high compared to the theoretical value. These discrepancies were suggested to result from (i) the presence of a small amount of hard martensitic phase not detectable using X-rays and/or (ii) the presence of

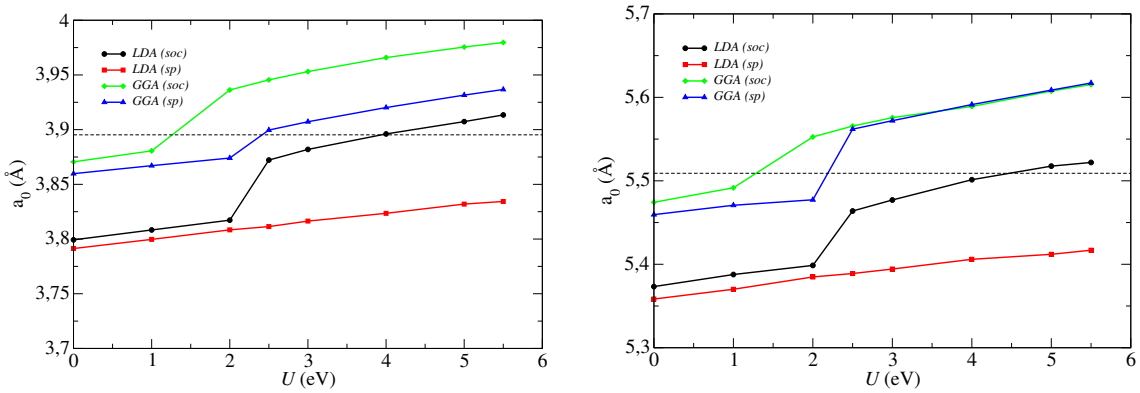

(a) change in a-axis as a function of U - parameter

(b) change in c-axis as a function of U - parameter

FIG. 3: (Color online) The change in the lattice parameters is plotted within the description of DFT + U (GGA, LDA) approximations for PaO_2. It shows that the U-parameter leads to a change in the structural parameters.

large experimental errors in the early diamond anvil cell techniques.[20] Recent experimental studies by Haire *et al.*[21] obtained a bulk modulus of 118.00 GPa. This value is lower than previously reported experimental results. In our study using LDA with SOC, the bulk modulus is found to be 117.93 GPa which compares excellently with the reported experimental value. The bulk modulus obtained using GGA with SOC is 98.18 GPa, which is slightly lower than the experimental value shown in Table II.

TABLE II: Calculated and experimental lattice parameters in Å, density in g/cm^3, volume in $Å^3$ and bulk modulus in GPa for Pa metal.

Type of calculation	a_0	c	ρ	volume	bulk Modulus
Experiment (Ref. 17)	3.925	3.238	15.382	24.99	118.00
LDA (SOC)	3.815	3.104	16.978	22.75	117.93
LDA (SP)	3.833	3.108	16.805	22.83	115.24
GGA (SOC)	3.907	3.185	15.778	24.32	98.18
GGA (SP)	3.930	3.196	15.543	24.68	94.06

The elastic properties of PaO using GGA and GGA + U (SOC scheme) is presented in Table III. The elastic constants obtained for PaO are all positive definite, hence PaO is elastically stable. But

the value of the c_{44} elastic constant for PaO within GGA and GGA + U using the SOC approach is very low compared to the other elastic constants. We calculated the elastic constants for NM and SP cases. The c_{44} elastic constant obtained using NM and SP is also very low compared to the other elastic constants. This is an indication that the material will readily yield to shear stresses. The Debye temperature (Θ_D) is calculated to determine the stiffness of the system. The Θ_D for PaO is 275.4 K.

TABLE III: Elastic constants, bulk and shear in GPa, Debye temperature in K for PaO. PaO results presented are for the SOC case and the U parameter is 2.5 eV.

Type of Calculation	c_{11}	c_{12}	c_{44}	*bulk*	*shear*	Θ_D
GGA	348.61	106.75	9.08	187.37	34.11	216.5
GGA + U	363.98	92.19	27.57	182.79	55.69	275.4

The elastic constants obtained for PaO_2 are all positive definite. Hence, the PaO_2 structure is elastically stable within GGA and GGA + U as presented in Table IV. The elastic properties obtained using GGA are less than those using LDA. This is also consistent with the GGA + U and LDA + U. This is expected because the value of the lattice parameter is higher within the GGA than those obtained using the LDA. The Debye temperature for PaO_2 is 409.5 K. This material is stiff and suggestive of covalent and ionic character. We conclude that PaO_2 is significantly stiffer compared to PaO. The bonding character is fully analyzed in the next subsection.

TABLE IV: Elastic constants, bulk modulus and shear modulus in GPa, Debye temperature in K for PaO_2. The PaO_2 results presented corresponds to the SOC and U = 2.0 eV

Type of Calculation	c_{11}	c_{12}	c_{13}	c_{33}	c_{44}	c_{66}	*bulk*	*shear*	Θ_D
GGA	316.96	156.15	103.69	369.93	80.34	132.98	192.32	98.45	421.9
GGA + U	297.93	141.76	99.41	343.81	73.11	123.83	180.09	91.09	409.5

E. Valence charge densities of PaO and PaO_2

The computed valence charge density using the GGA + U optimized structures (SOC scheme) is presented to elucidate the bonding characteristics and crystal structures of PaO and PaO_2. The

computed charge density distribution plot for PaO and PaO_2 is in the (100) plane. The electron density is indicated by the color scale on the side (blue is devoid of electrons and red indicates a high concentration of electrons). The charge densities plotted pertain to the valence states only, summed over both spin directions.

In the PaO crystal structure, the Pa^{2+} ion is almost devoid of valence electrons and the cloud of electrons around O^{6+} ion is almost the full eight electrons needed to give O^{2-} (conventional oxygen is lacking two electrons). The valence charge density for PaO is calculated at $U = 2.5$ eV, which is determined to be the optimum U parameter for this structure. In Fig 4, it is clearly seen that PaO is characterized by a high spherical charge density distribution around the Pa and O ions and a low charge density in the interstitial region. Compared to the charge density in the interstitial region, relatively high density bridges are present between the atomic spheres. These bridges are an indication of weak covalent bonding between Pa and O atoms due to hybridization of oxygen $2p$ states with partially occupied Pa f and d states. Therefore, PaO is strongly ionic and weakly covalently bonded.

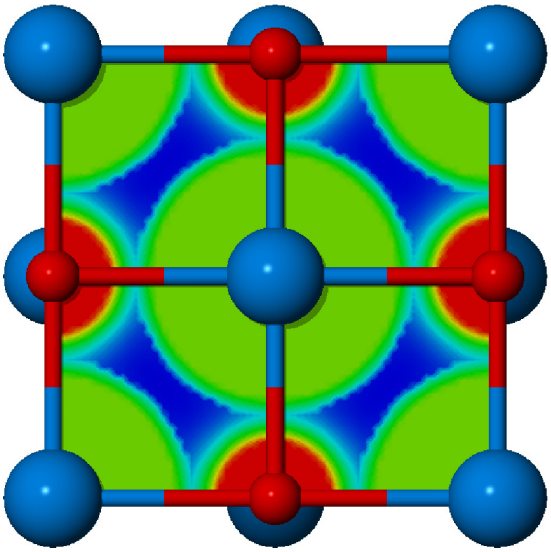

FIG. 4: (Color online) The color pattern of the calculated valence charge density distribution for PaO in the (100) plane, where the blue spheres depict Pa atoms and the red spheres depict the O atoms.

In the AFM PaO_2 crystal structure, the valence charge density is calculated at $U = 2.0$ eV, which is determined to be the optimum U parameter for this structure. In Fig. 5, it is clearly seen that PaO_2 is characterized by high spherical charge density distribution around the Pa and O ions

with a low charge density in the interstitial region. Compared to the charge density in the rest of the interstitial region there is a low presence of charge density bridges present between the atomic spheres. These bridges are an indication of weak covalent bonding between Pa and O atoms due to hybridization of oxygen 2*p* states with partially occupied Pa *f* and *d* states. The charge density around the Pa atom in PaO_2 structure is low compared to the PaO structure. This is an indication of stronger ionic character in AFM PaO_2 and weak covalent character compared to PaO system. Therefore, PaO_2 is predominantly ionic with significant insulating behavior.

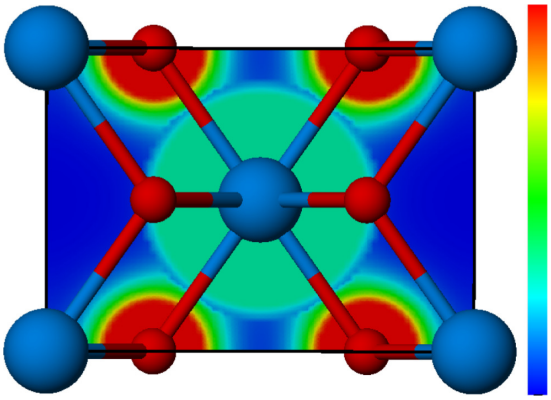

FIG. 5: (Color online) The color pattern of the calculated valence charge density distribution for PaO_2 in the (001) plane, where the blue spheres depict Pa atoms and the red spheres depict the O atoms. The color scale: deep blue color represents low valence charge while the red color represents high concentration valence charge.

Also, in Table I, the *f* occupation for PaO_2 compared to PaO gives credence to the notion that PaO_2 is more ionic.

F. Band structure and density of states

The computed band structure and density of states (DOS) presented below is within GGA + *U*. The result obtained using LDA + *U* (with a large value of *U*) gives qualitatively similar results to GGA + *U*.

In Fig. 6, we present the band structure and density of states of Pa metal calculated using GGA within the SOC scheme. The band structure and DOS clearly shows that Pa is metallic. The metallicity is largely determined by the Pa-*f* electrons and a slight contribution from Pa-*d* electrons, while the Pa-*s* and Pa-*p* electrons contribute to the deep lying states.

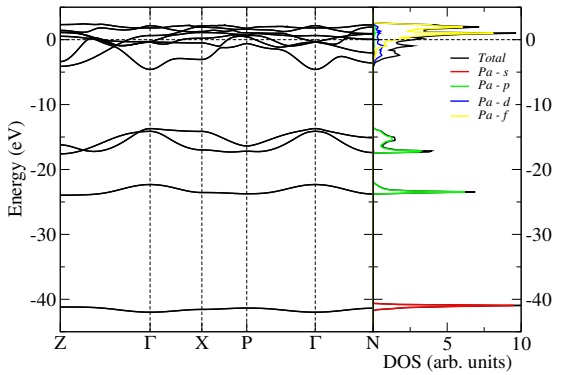

FIG. 6: (Color online) The calculated band structure and DOS plot of Pa in the full Brillouin zone.

Fig. 7 shows the band structure of PaO_2 with an indirect band gap of 3.48 eV which is calculated using GGA + U within the SOC scheme at U = 2.0 eV. The LDA + U within the SOC scheme at U = 2.0 eV underestimates the band gap, while the SP scheme within the DFT + U results in a metallic system. The valence band maximum for PaO_2 using GGA + U within the SOC scheme at U = 2.0 eV is located in between the Z-point (0.0 0.0 0.5) and the A-point (0.5 0.5 0.5). While, the conduction band minimum is located at the R-point (0.0 0.5 0.5). In Table V, the effect of tuning the U parameter on the band gap is tabulated. Increasing the U parameter leads to opening of the band gap at U = 2.0 eV. Subsequently, increasing the U parameter leads to a decrease in the band gap, which is accompanied by a change in the position of the conduction band minimum and valence band maximum.

The DOS for the PaO system using GGA + U is presented in Fig. 8.We find that PaO using various exchange correlation functionals (GGA and LDA) and inclusion of the U parameter is a metallic system. The states around the Fermi level is dominated by the 5f-electrons, which effectively determine the metallicity of the PaO system as shown in Fig. 8. The partial density of states as a function of change in the effective U parameter for the SOC and SP schemes provides an insight on the hybridization and magnetic nature of the system. In the SOC scheme, the PaO system undergoes hybridization and evolves from a magnetic ground state at U = 0 eV with total magnetization of 0.47 μ_B to a NM metallic ground state as a function of U. In the SP scheme, the PaO system undergoes hybridization and evolves from a magnetic ground state at U= 0 eV with total magnetization of 0.51 μ_B to a NM metallic ground state as a function of the U. This is consistent with its neighboring oxides ThO and UO. This observation for PaO with respect to

TABLE V: The optimum U parameter as a function of band gap (null band gap indicates a metal) for PaO_2. Where Z (0.0 0.0 0.5), A (0.5 0.5 0.5), R(0.0 0.5 0.5), X (0.0 0.5 0.0), and Γ (0.0 0.0 0.0)

U	Band gap	Position of Band gap	
		Valence Band	Conduction Band
0.0	0.00	–	–
1.0	0.00	–	–
2.0	3.48	in between Z and A	R
2.5	3.40	in between Z and A	in between R and X
3.0	3.30	in between Z and A	in between X and Γ
4.0	3.01	in between Z and A	Γ
5.0	2.72	in between Z and A	Γ
5.5	2.55	in between Z and A	Γ

GGA is consistent with LDA, hence the figures and data on LDA are not presented.

The electronic structure of the early actinides dioxides (AO_2, where A=Th, Pa, U, Np) all show insulating character.[23] The ground state of UO_2 and NpO_2 show varying degrees of magnetism,

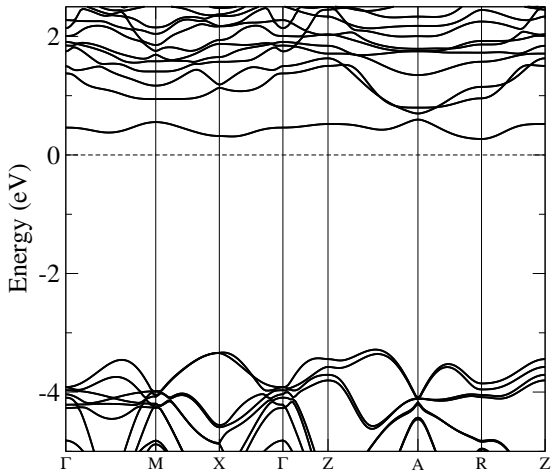

FIG. 7: (Color online) The calculated band structure plot of PaO_2 using DFT + U (U = 2.0 eV) in the full Brillouin zone with an AFM structure. The system contains two unique Pa atoms due to the spin configuration and the O atoms are same.

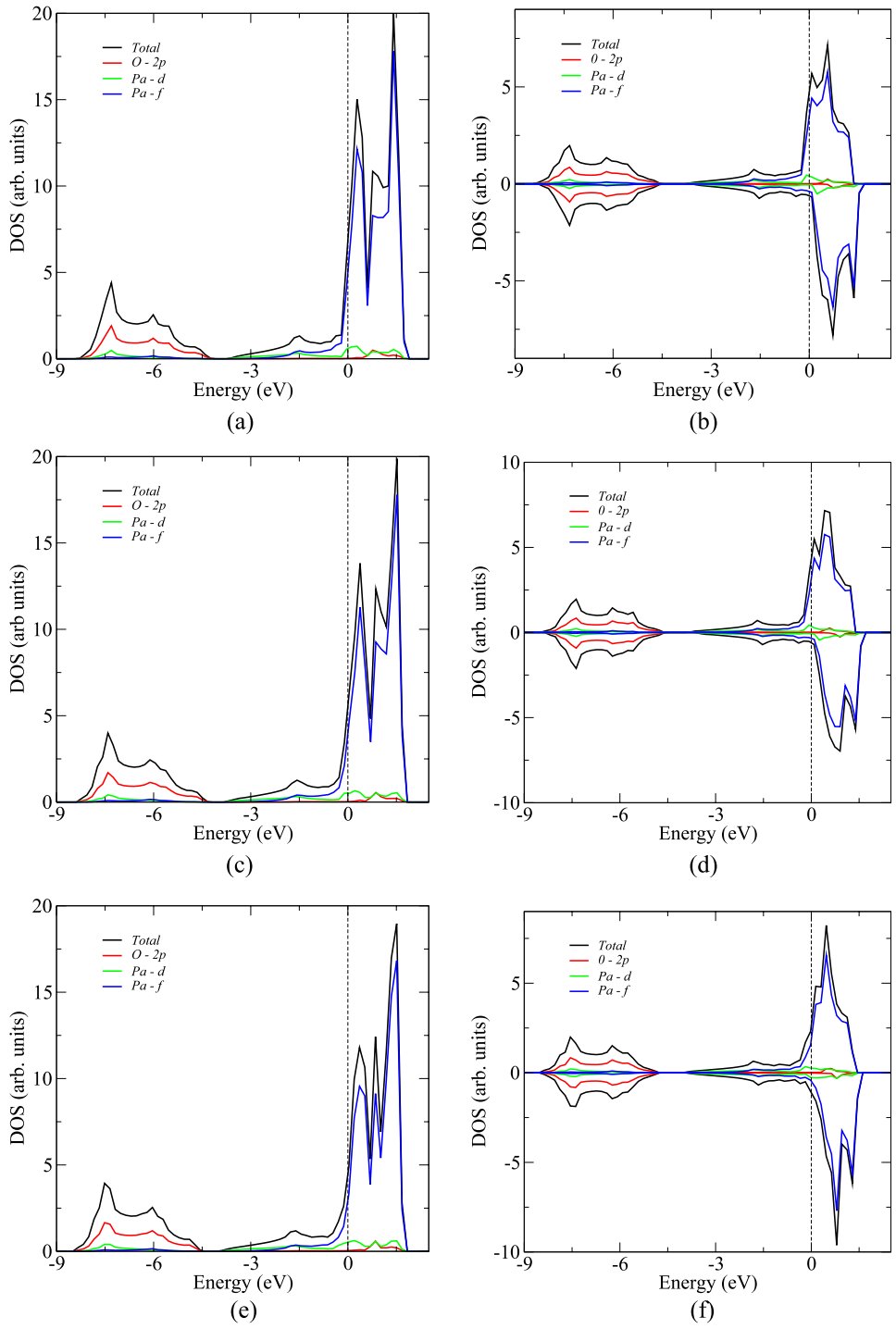

FIG. 8: (Color online) The total and projected densities of states (DOS) for the spin polarized and spin-orbit coupling of PaO within the descriptions of GGA and GGA + U approximations . All the DOS are calculated at the optimized geometry for the given density functional and magnetic ordering. The Fermi energy level is set at zero and is represented using dashed line. It contains one Pa atoms and the O atoms are same.

while ThO_2 is NM. These characteristics of U and Np are attributed to the partially occupied 5*f* electrons, which favors itinerancy for the early actinides. The PaO_2 system within the standard LDA and GGA approach (with SP or/and SOC scheme) is a metallic NM ground state. The inclusion of the Hubbard U parameter leads to band gap opening for the system using the SOC scheme (for GGA and LDA). Because the SOC splits the orbitals, thus allowing for a U induced orbital polarization that opens a gap. However, the U parameter does not lead to band gap opening using the SP scheme due to the negligence of relativistic effects. In the SOC and SP schemes, the coupling between the Pa (5*f* and 6*d*) electrons and the O (2*p*) electrons is important as presented in Fig. 9.

As mentioned in the preamble, PaO_2 is a difficult system to study computationally due to the subtle nature of the electron correlation for this system. The DOS for an energy cutoff of 400 eV and 550 eV is shown in Fig. 10 and 9 to buttress this point. The lattice parameter of PaO_2 is fully converged as a function of the energy cutoff at 500 eV. Hence, a less converged energy cutoff (400 eV) and a fully converged energy cutoff (550 eV) are used to show the sensitivity of the U parameter. At an energy cutoff of 400 eV, tuning the U parameter leads to significant change in the band gap from 0.3 eV at U = 3.0 eV to 1.37 eV at U = 5.5 eV. At an energy cutoff of 550 eV, the converged U = 2 eV results in a band gap of 3.48 eV. Further tuning of the U parameter leads to a decrease in the band gap, which is shown in Table V. The band gap obtained for U= 5.5 eV at an energy cutoff of 400 eV is consistent with the study by Prodan *et al.* and recently by Wen *et al.*[39] using the HSE hybrid exchange-correlation functional. Using U = 2.0 eV at a converged energy cutoff of 550 eV, the band gap obtained is 3.48 eV. This value is intermediate to that of ThO_2 (6.2 eV) and UO_2 (2.0 eV) which is consistent with the trend because it shows the onset of 5*f* electron occupation. The Pa 5*f* electrons determine the conduction band maximum and play a significant role in the electronic properties of these systems. The Pa *f* electrons are localized and result in insulating behavior. This corroborates other results where the crystal structure and the volume of actinides exhibit different bonding configurations.[17]

G. Energy of formation of PaO and PaO_2

The energy of formation for the oxides is calculated using equation 1. The total energy of the constituent elements is deducted from the total energy for the system (PaO or PaO_2). In Table VI, we present the energy of formation for the oxides using the LDA + U and GGA + U within the

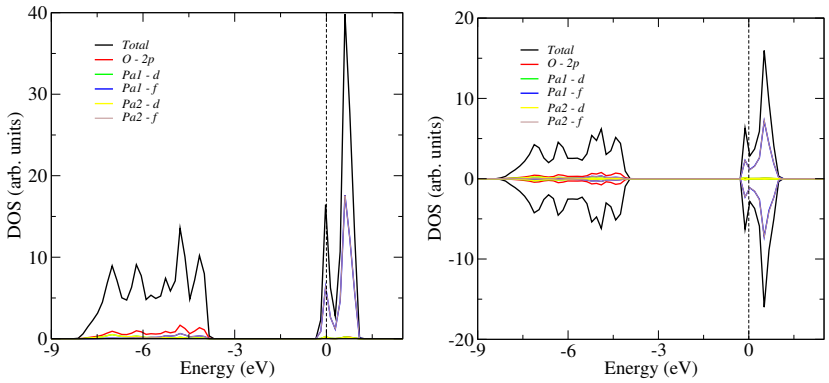

(a) SP + SOC U = 0 (b) SP U = 0

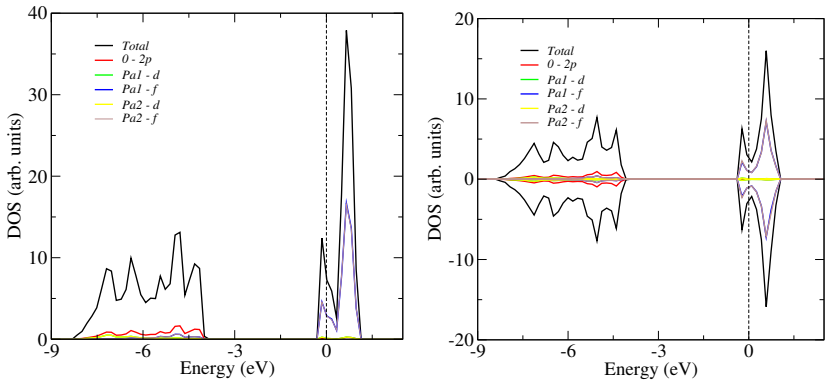

(c) SP + SOC U = 1 (d) SP U = 1

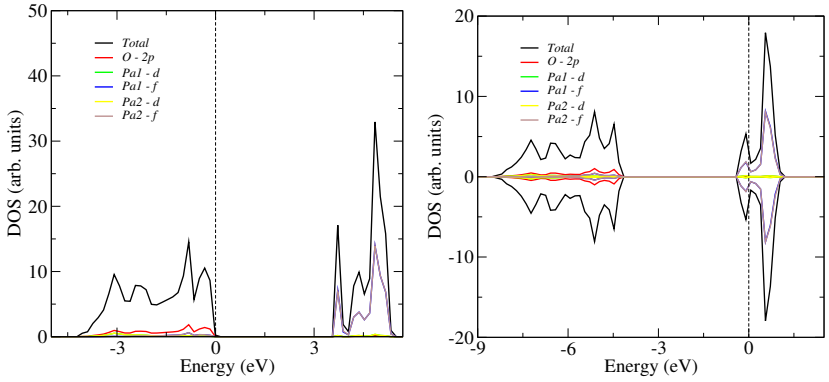

(e) SP + SOC U = 2 (f) SP U = 2

FIG. 9: (Color online) The total and projected densities of states (DOS) for the SP and SP + SOC of PaO_2 in the AFM ordered phase within the descriptions of GGA and GGA + U approximations at an energy cutoff of 550 eV. All the DOS are calculated at the optimized geometry for the given density functional and magnetic ordering. The Fermi energy level is set at zero and is represented by the dashed line. It contains two unique Pa atoms (label Pa_1 and Pa_2) due to the spin configuration and the O atoms are same.

SOC and SP schemes. The calculated energy of formation for PaO and PaO_2 using SOC is lower than that obtained with SP within the DFT + U (LDA and GGA). This implies that the SOC case is more energetically favorable than the SP case. The formation for PaO and PaO_2 is exothermic. This indicates that metallic Pa will oxidize in the presence of oxygen. The energy of formation of PaO_2 is lower than that of the PaO. The implication is that PaO readily oxidizes in the presence of oxygen to form the more energetically favorable di-oxide. Our theoretical results is in line with experimental observation, that the oxides are more favorable than the parent metal and that PaO_2 is more stable than PaO in the presence of oxygen.[15]

TABLE VI: The calculated Energy of formation (eV) for PaO and PaO_2 using LDA + U and GGA + U within the SOC and SP scheme.

Compound	U_{eff}	LDA(SOC)	LDA(SP)	GGA(SOC)	GGA(SP)
PaO	2.5	−6.19	−3.89	−5.43	−3.19
PaO_2	2.0	−12.60	−10.30	−11.62	−8.93

H. Phonon studies of PaO and PaO_2

The phonon dispersion for Pa, PaO and PaO_2 is calculated within the GGA (PBE) scheme. The lattice dynamics studies is not carried out for both the LDA and DFT + U scheme. This is because, the inclusion of U parameter does not lead to significant changes in the phonon frequency of these systems. The phonon dispersion calculated exploits the linearity relationship between the induced forces on the atoms in the crystal and the displacement of the atoms from their equilibrium position, which holds within the harmonic regime.

In Fig. 11a, no negative phonon modes for Pa are observed in the phonon dispersion plot, hence this structure is dynamically stable. The maximum frequency for the acoustic modes is about 4.5 THz due to the large mass of Pa atom which does not undergo significant perturbation.

In Fig. 11b, no negative phonon modes for PaO are observed in the phonon dispersion plot, hence this structure is dynamically stable. The low lying frequency modes are governed by the dynamics of heavy Pa atoms. The higher frequencies, on the other hand, are governed by the dynamics of the oxygen atoms which are much lighter compared to Pa atoms. The difference

in the frequency of oxygen atoms compared to the Pa atoms is rather large. This suggests that instability in the system can arise from a small perturbation of the crystal structure.

In Fig. 11c, no negative phonon modes for PaO_2 are observed in the phonon dispersion plot, hence this structure is dynamically stable. The low lying frequency modes are governed by the dynamics of heavy Pa atoms, whereas the higher frequencies are governed by the dynamics of lighter oxygen atoms. The difference in the frequency of oxygen atoms compared to the Pa atoms is lower compared with PaO. This implies that the extra oxygen atom has led to the stabilization of the structure.

IV. CONCLUSIONS

The structural, mechanical and electronic properties of Pa have been studied within the DFT method. Inclusion of SP and SOC give an adequate description of this system. As far as the structural properties are concerned, the inclusion of the Hubbard U parameter is not relevant here. We determined that Pa is elastically and dynamically stable.

The structural, mechanical and electronic properties of PaO have been studied within the DFT + U approximation. The inclusion of SP and SOC gives an adequate description of this system. Our calculations show that the properties of this system can be described accurately with an effective U parameter of 2.5 eV within the GGA + U. The results using LDA + U were unsatisfactory. PaO is dynamically stable as shown by the phonon dispersion data. PaO is also stable to isotropic stress because of its positive bulk modulus. However, PaO has a low shear modulus. The charge density plot shows the presence of strong ionic bonding in this system. We conclude that PaO structure will readily oxidize to PaO_2 structure, which is the more stable form. This is in line with observed experimental results.

The SOC inclusion together with the Hubbard U parameter is essential for the accurate determination of the total energy, electronic and magnetic properties of PaO_2. Within the LDA + U (SOC scheme) at U = 4.0 eV, the lattice parameter is 5.501 Å, which is approximately equal to the experimental result. However, the results for the band gap and the energy of formation are found to be unsatisfactory within this scheme. On the other hand, within the GGA + U (SOC scheme) at U = 2.0 eV, the lattice parameter is 5.553 eV, which is approximately 0.78 % above the experimental value. Within this scheme we derive accurate results for the electronic, elastic and mechanical properties of the system. This method predicts PaO_2 as an insulator with a band gap

of 3.48 eV.

Hence, to obtain an accurate description of the PaO and PaO_2, we have shown that the inclusion of the Hubbard U parameter is paramount. In general, the GGA is better suited for the incorporation of the Hubbard U parameter for these systems.

ACKNOWLEDGMENTS

This work is supported by the University of Pretoria. We gratefully acknowledge Material Design Inc. support in particular Rene Windiks, Walter Wolf, Paul Saxe and the members of the Computational and Theoretical Physics group at the University of Pretoria. Also, we are thankful to Dr. Jannie Pretorius for help with the use of the computational resources. NC is grateful to the National Institute for Theoretical Physics for support.

---

* Kingsley.Obodo@up.ac.za

† Nithaya.Chetty@up.ac.za

[1] Moore Kevin T., van der Laan Gerrit. Nature of the $5f$ states in actinide metals. *Rev. Mod. Phys.*, 81(1):235–295, 2009.

[2] M.S.S.S. Brook, G. Calestani, J.C. Spirlet, J. Rebizant, W. Muller, J. M. Fournier, and A. Blaise. f-Electron Contribution to Bonding in Protactinium Compounds. *Physica B*, 102B:84–87, 1980.

[3] Alexander B. Shick, Vaclav Janis, and Peter M. Oppeneer. Effect of Coulomb Correlations on the Electronic Structure of PuCoGa5. *Physical Review Letters*, 016401(January):1–4, 2005.

[4] Christoph Loschen, Javier Carrasco, Konstantin Neyman, and Francesc Illas. First-principles LDA+U and GGA+U study of cerium oxides: Dependence on the effective U parameter. *Physical Review B*, 75(3):1–8, January 2007.

[5] Bao-tian Wang, Hongliang Shi, Weidong Li, and Ping Zhang. First-principles LDA + U and GGA + U study of neptunium dioxide. *Physical Review B*, 81:3–8, 2010.

[6] M. Fhokrul Islam and Asok K. Ray. A LDA + U study of the photoemission spectra of the double hexagonal close packed phases of Am and Cm. *Solid State Communications*, 150(19-20):938–942, 2010.

[7] Per Söderlind, G. Kotliar, K. Haule, P. M. Oppeneer, and D. Guillaumont. Computational modeling of

actinide materials and complexes. *MRS Bulletin*, 35(November):883–889, 2010.

[8] Vladimir I. Anisimov, Jan Zaanen, and Ole K. Andersen. Band theory and Mott insulators: Hubbard U instead of Stoner I. *Physical Review B*, 44(3):943–954, 1991.

[9] A. I. Liechtenstein, V. I. Anisimov, and J. Zaanen. Density-functional theoy and strong interactions: Orbital ordering in Mott-Hubbard insulators. *Physical Review B*, 52(8):5467–5471, 1995.

[10] V. I. Anisimov, F. Aryasctiawan, and A. I. Lichtenstein. First-principles calculations of the electronic structure and spectra of strongly correlated First-principles calculations of the electronic structure and spectra of strongly correlated systems : the LDA + U method. *Journal of Physics: Condensed Matter*, 767:767–808, 1997.

[11] S. L. Dudarev, G. A. Botton, S. Y. Savrasov, C. J. Humphreys, and A. P. Sutton. Electron-energy-loss spectra and the structural stability of nickel oxide: An LSDA + U study. *Physical Review B*, 57(3):1505–1509, 1998.

[12] F. Aryasetiawan, M. Imada, A. Georges, G. Kotliar, S. Biermann, and A. I. Lichtenstein. Frequency-dependent local interactions and low-energy effective models from electronic structure calculations. *Physical Review B*, 70(19):195104, 2004.

[13] Matteo Cococcioni and Stefano De Gironcoli. Linear response approach to the calculation of the effective interaction parameters in the LDA+ U method. *Physical Review B*, 71:1–16, 2005.

[14] G. W. Chinthaka Silva, Philippe F. Weck, Eunja Kim, Charles B. Yeamans, Gary S. Cerefice, Alfred P. Sattelberger, and Kenneth R. Czerwinski. Crystal and Electronic Structures of Neptunium Nitrides Synthesized Using a Fluoride Route. *Journal of The American Chemical Society*, 134:3111–3119, 2012.

[15] Lester R. Morss, Norman M. Edelstein, and Jean Fuger. *The Chemistry of the Actinide and Transcatinide Elements*. 2010.

[16] P. Soderlind. Theory of the crystal structures of cerium and the light actinides. *Advances in Physics*, 47(6):959–998, 1998.

[17] R. G. Haire. Insights into the bonding and electronic nature of heavy element materials. *Journal of Alloys and Compounds*, 445(2007):63–71, 2008.

[18] R. D. Fowler, B. T. Matthias, L. B. Asprey, H. H. Hill, J. D. G. Lindsay, C. E. Olsen, and R. W. White. SUPERCONDUCTIVITY OF PROTACTINIUM *Physical Review Letters*15(22): 860862, 1965.

[19] J. E.Gordon, H. Montgomery, R. J. Noer, G. R. Pickett, and R. Tobon. Superconductivity of Thorium and Uranium *Physical Review*152(1): 432437, 1966.

[20] Hubert Blank. Experimental results on properties of Pa revisited. *Journal of Alloys and Compounds*,

343:108–115, 2002.

[21] R. Haire, S. Heathman, M. Idiri, T. Le Bihan, A. Lindbaum, and J. Rebizant. Pressure-induced changes in protactinium metal: Importance to actinide-metal bonding concepts. *Physical Review B*, 67(13):1–10, April 2003.

[22] Per Soderlind and Olle Eriksson. Pressure-induced phase transitions in Pa metal from first-principles theory. *Physical Review B*, 56(17):10719–10721, 1997.

[23] Ionut D. Prodan, Gustavo E. Scuseria, and Richard L. Martin. Covalency in the actinide dioxides: Systematic study of the electronic properties using screened hybrid density functional theory. *Physical Review B*, 76(033101):1–4, 2007.

[24] P. Hohenberg and W. Kohn. Inhomogeneous Electron Gas. *Physical Review*, 136(3B):864, 1964.

[25] G. Kresse and J. Furthmüller. Efficient iterative schemes for ab initio total-energy calculations using a plane-wave basis set. *Physical Review B*, 54(16):11169, October 1996.

[26] G. Kresse and D. Joubert. From ultrasoft pseudopotentials to the projector augmented-wave method. *Physical Review B*, 59(3):11–19, 1999.

[27] J. P. Perdew and Alex Zunger. Self-interaction correction to density-functional approximations for many-electron systems. *Physical Review B*, 23(10):5048–5079, 1981.

[28] John P. Perdew, Kieron Burke, and Matthias Ernzerhof. Generalized Gradient Approximation Made Simple. *Physical review letters*, 77(18):3865, October 1996.

[29] Hendrik J. Monkhorst and James D. Pack. Special points for Brillouin-zone integrations. *Physical Review B*, 13(12):5188, 1976.

[30] M. Methfessel and A. T. Paxton. High-precision sampling for Brillouin-zone integration in metals. *Physical Review B*, 40(6):3616, 1989.

[31] Yvon Le Page and Paul Saxe. Symmetry-general least-squares extraction of elastic data for strained materials from ab initio calculations of stress. *Physical Review B*, 65:104104, February 2002.

[32] R. Hill. The elastic behaviour of a crystalline aggregate. *Proceedings of the Physical Society, Section A*, 65(5):349, 1952.

[33] Orson L. Anderson. A Simplified method for calculating the Debye temperature from elastic Constants. *Journal of Physics: Chemucak Solids*, 24:909–917, 1963.

[34] K. Parlinski, Z. Q. Li, and Y. Kawazoe. First-Principles Determination of the Soft Mode in Cubic ZrO 2. *Physical Review Letters*, 78(21):4063–4066, 1997.

[35] Denis Gryaznov, Eugene Heifets, and David Sedmidubsky. Density functional theory calculations

on magnetic properties of actinide compounds. *Physical chemistry chemical physics : PCCP*, 12(38):12273–8, October 2010.

[36] Boris Dorado, Bernard Amadon, Michel Freyss, and Marjorie Bertolus. DFT + U calculations of the ground state and metastable states of uranium dioxide. *Physical Review B*, 235125(79):1–8, 2009.

[37] B. Meredig, A. Thompson, H. A. Hansen, and C. Wolverton. Method for locating low-energy solutions within DFT+U. *Physical Review B*, 82:2–6, 2010.

[38] P. Soderlind, O. Eriksson, and B. Johansson. Electronic properties of f metals using the generalized gradient approximation. *Physical Review B*, 50(11):7291–7294, 1994.

[39] Wen X.-D. , Martin, R. L., Roy L. E., Scuseria G. E., Rudin S. P., Batista E. R., McCleskey T. M., Scott B. L.,Bauer E. , Joyce J. J., and Durakiewicz T. Effect of spin-orbit coupling on the actinide dioxides AnO2 (An=Th, Pa, U, Np, Pu, and Am): a screened hybrid density functional study. *The Journal of chemical physics*, 137 (15):154707.

[40] Borje Johansson and Hans L. Skriver. Electronics Structure of the Actinide Metals. *Journal of Magnetism and Magnetic Materials*, 29:217–229, 1982.

[41] U. Benedict, J. C. Spirlet, C. Dufour, I. Birkel, W. B. Holzapfel, and J. R. Peterson. X-RAY DIFFRACTION STUDY OF PROTACTINIUM METAL TO 53 GPa. *Journal of Magnetism and Magnetic Materials*, 29:287–290, 1982.

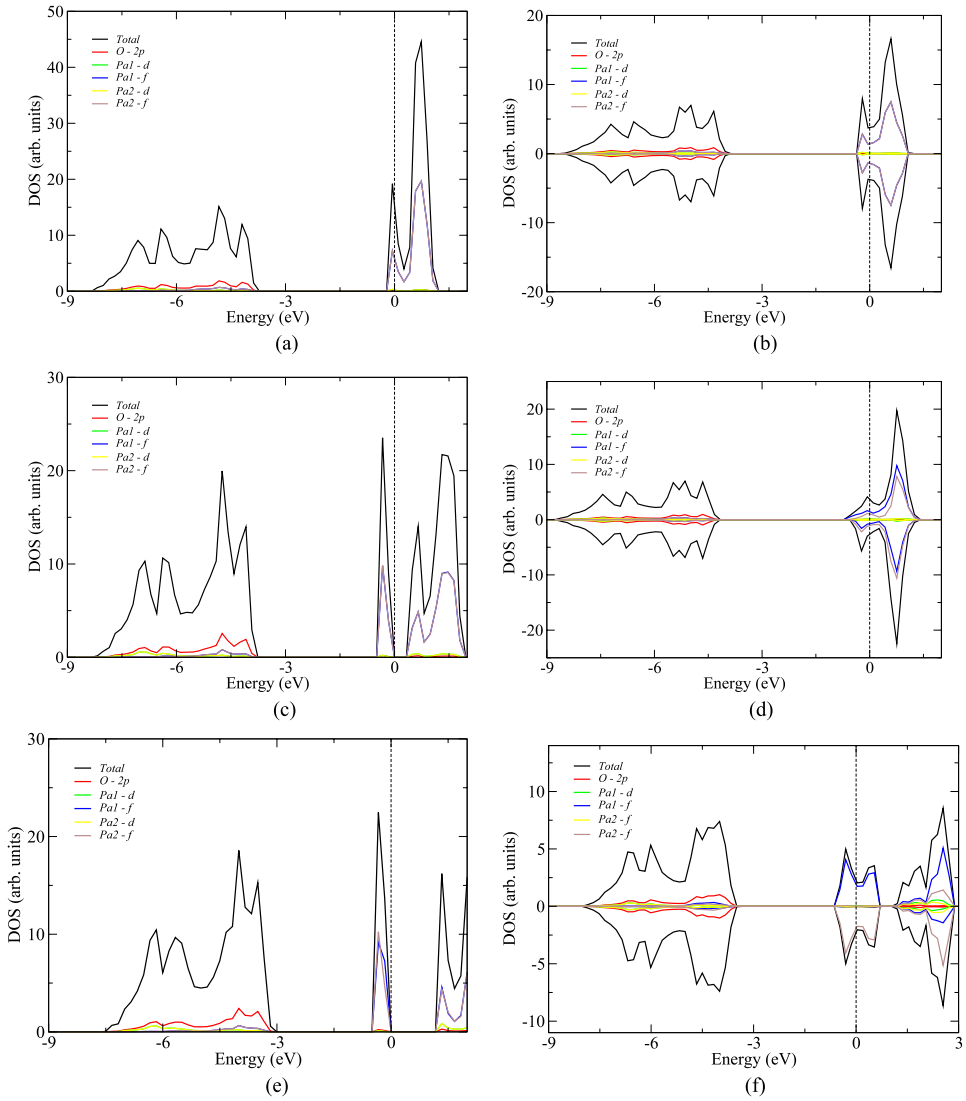

FIG. 10: (Color online) The total and projected densities of states (DOS) for the SP and SP + SOC of PaO_2 in the AFM ordered phase within the descriptions of GGA and GGA + U approximations at an energy cutoff of 400 eV. All the DOS are calculated at the optimized geometry for the given density functional and magnetic ordering. The Fermi energy level is set at zero and is represented by the dashed line. It contains two unique Pa atoms (label Pa_1 and Pa_2) due to the spin configuration and the O atoms are same.

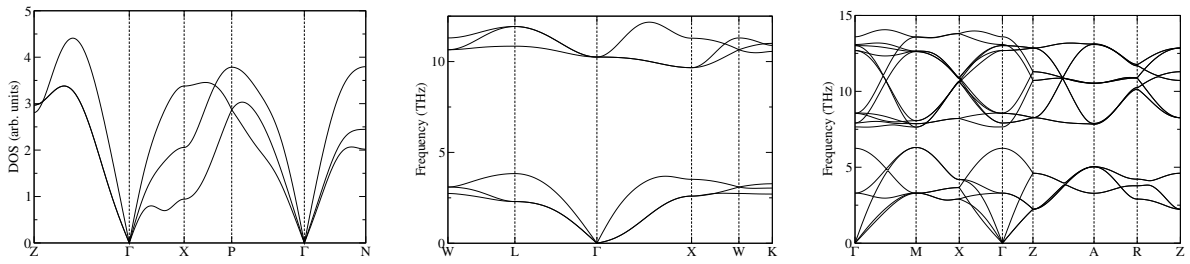

(a) Phonon dispersion of Pa (b) Phonon dispersion of PaO (c) Phonon dispersion of PaO_2

FIG. 11: (Color online) The phonon dispersion plot of PaO and PaO_2, showing the lattice dynamics of Pa and O atoms.

This concludes the studies on Pa and its oxides. The next chapter presents a comparative study of various actinide mononitride and dinitride compounds. It shows the significance of the Hubbard U parameter in the proper description of these actinide systems with $5f$ electrons. These material have important technological application in nuclear energy generation (considered as possible nuclear fuel material).

Chapter 6

GGA + U studies of the early actinide mononitrides and dinitrides

This section was published as[10] "Obodo, K. O. and Chetty, N. (2013). *GGA + U studies of the early actinide mononitrides and dinitrides*. Journal of Nuclear Materials, 442(1-3), 235244."

GGA + *U* studies of the early actinide mononitrides and dinitrides

K. O. Obodo[1]

E-mail: Kingsley.Obodo@up.ac.za
[1]Physics Department, University of Pretoria, Pretoria 0002, South Africa; [2]National Institute for Theoretical Physics,Johannesburg, 2000, South Africa

N. Chetty[1,2]

E-mail: Nithaya.Chetty@up.ac.za
[1]Physics Department, University of Pretoria, Pretoria 0002, South Africa; [2]National Institute for Theoretical Physics,Johannesburg, 2000, South Africa

Abstract. We present a detailed comparative study of the electronic and mechanical properties of the early actinide mononitrides and dinitrides within the framework of the Perdew-Burke-Ernzerhof generalized gradient approximation (GGA [PBE]) and GGA + *U* implementations of density functional theory with the inclusion of spin-orbit coupling. The dependence of selected observables of these materials on the effective *U*-parameter is investigated in detail. The properties include the lattice constant, bulk modulus, charge density distribution, hybridization of the atomic orbitals, energy of formation and the lattice dynamics. The inclusion of the Hubbard *U* parameter results in a proper description of the 5*f* electrons, and is subsequently used in the determination of the structural and electronic properties of these compounds. The mononitrides and dinitrides of the early actinides are metallic except for UN_2, which is a semiconductor. These actinide nitrides are non-magnetic with the exception of UN, NpN, PuN, NpN_2 and PuN_2 that are magnetic systems with orbital-dependent magnetic moments oriented in the z-axis. We observed that ThN_2 is elastically unstable to isotropic pressure. We discovered that UN_2 is thermodynamically unstable, but may be stabilized by N vacancy formation.

Submitted to: *J. Phys.: Condens. Matter*

PACS numbers: 62.20.D-, 63.20.D-, 71.15.Mb, 71.20.-b, 71.27.+a

1. Introduction

The investigation of actinide-based materials is an area of active research. [1, 2, 3, 4, 5, 6, 7, 8, 9, 10, 11] The effects of *5f*-electrons in the actinide nitrides are of significant interest to both theorists and experimentalists, [12, 13, 14] because exotic properties often arise from the strong electron-electron interactions paving the way for interesting physics and novel applications. The actinide metals exhibit increased 5*f* electronic localization with increasing atomic number which has a direct bearing on the orbital overlap and electronic band structure of these systems.

Actinide nitrides are set to become a major component in large-scale energy generation devices in nuclear power stations as an alternative to the current fuel sources that are being used. [15, 16] The Generation-IV nuclear reactors (fast neutron fission reactors) are developed to use the actinide nitrides as the primary fuel source. [17] Actinide nitrides release a larger amount of fissile products (neutrons) compared to its consumption, and the long-lived fission products have a higher probability to transmute leading to higher usable energy densities.

Based on the importance of the actinide nitrides from both a scientific and technological point of view, the understanding of the electronic and structural properties is important to harness, control, and effectively use these materials. The presence of 5*f* electrons poses a considerable challenge in the theoretical description of the actinide compounds. This is mainly due to the improper account of the electron-electron interactions by the local spin density approximation (LSDA) and the generalized gradient approximation (GGA) approaches implemented in density functional theory (DFT). The DFT + U [18, 19, 20] (LDA + U and GGA + U) approach has been shown to overcome some of the shortcomings and shows a lot of promise in the studies of the 5*f* electron systems.

In this work, the actinide nitrides of interest are the early actinide mononitrides (AcN) and dinitrides (AcN_2) where (Ac = Th, Pa, Np, U and Pu). At low temperatures, the AcN crystallizes in the NaCl crystal structure, while the AcN_2 mainly exists in the fluorite structure. There also exist other actinide compounds that crystallize in the NaCl crystal structure such as the mono-carbides, mono-pnictides, mono-chalcogenides, etc.

To the best of our knowledge, a detailed analysis of these systems within the DFT + U approach is lacking. [21, 22, 9, 23] Petit *et al.* [9] investigated some actinide mono-carbides and mononitrides using the self-interaction corrected (SIC) local spin-density approximation. These authors observed ionic character in the mononitrides, increased localization in PuN, and an itinerant picture for UN. Silva *et al.*, [4] recently synthesized NpN and confirmed the existence of other phases of neptunium nitrides using both experimental and computational techniques. These authors showed the importance of the Hubbard U-parameter (accounting for onsite interactions) along with relativistic effects to accurately describe these compounds.

Atta-Fynn *et al.* [21] treated all the nitrides on equal footing at different magnetic configurations with and without spin orbit coupling (SOC). They showed that the type-I anti-ferromagnetic (AFM) configuration gives similar results to the type-II AFM configuration and results in a more energetically favorable configuration with the inclusion of SOC.

In our work, we have therefore considered the type-I AFM structure within the projector augmented wave (PAW) method to analyze the mononitride systems. We compare our results with available experimental data as well as with other theoretical results. All calculations are based on density functional theory with and without the inclusion of the Hubbard U-parameter (DFT + U). We evaluate the heat of formation, the structural, electronic, elastic, and mechanical properties of the various actinide nitrides. Of interest is how well our zero temperature DFT + U computations predict these properties. Previous studies proposed that PaN has a more covalent character compared to UN, NpN, PuN that are predominantly ionic.

Therefore, by scrutinizing the valence charge density distributions, we examine the AcN and AcN_2 compounds to give an account of the bonding character of these systems. The Hubbard U-parameter is shown to be important in the prediction of the structural properties of the actinide nitrides. The lattice dynamics of these systems gives an indication of the mechanical stability.

The rest of this paper is organized as follows: in Section 2, we present a description of the computational methodology. The calculated ground state properties of AcN and AcN_2 compounds, and the effect of the Hubbard U-parameter are given in Section 3 and 4 respectively. Finally, we make our concluding remarks in Section 5.

2. Computational Details

The calculations are performed using density functional theory [24] as implemented in the VASP code [25]. The PAW approach of Blöchl in the implementation of Kresse and Joubert is used to describe the electron wave functions. [26] The semi-core electrons and the valence electrons of the actinides are represented by plane waves. The PBE [27] form for the GGA and the GGA + U is used in the description of the exchange-correlation potential.

The unit cell parameters and atomic positions are optimized with an energy tolerance of 10^{-7} eV. The calculations are performed with an energy cut-off of 500 eV and 550 eV for AcN and AcN_2 respectively. The Brillouin zone (BZ) integrations are performed using a spacing of 0.2 $Å^{-1}$ for the Monkhorst-Pack [28] grid. Fractional electron occupancies and integration of the bands at the Fermi level are determined using the Methfessel-Paxton smearing method with a smearing parameter of 0.2 eV. The AcN and AcN_2 with SOC (spin-orbit coupling) calculations are performed within the constraints of symmetry. The lifting of the symmetry constraints lead to no significant change in the total energy and electronic properties, with an exception of PuN and UN_2 were the calculation is performed with the symmetry constraints lifted [3]. The total energy, electronic band structure and density of states (DOS) were calculated using the tetrahedron integration method with Blöchl corrections.

We use the Dudarev *et al.* [29] simplified rotationally-invariant form for the Hubbard correction to account for the on-site Coulomb interactions. This approach combines the Hubbard U and Hund's J to give the $U_{eff} = U - J$. The rotational invariance is preserved within this formalism because the U parameter depends on the trace of the occupation matrices and their products. The generic expression for the energy functional in the DFT + U formalism is represented by

$$E_{DFT+U} = E_{DFT} + E_{Hub} - E_{dc}, \tag{1}$$

where E_{DFT} is the DFT (LDA or GGA) contribution to the total energy and E_{Hub} is the electron-electron interaction from the Hubbard term. E_{dc} is a double counting term, introduced because part of the electron-electron interaction is taken into account in E_{DFT}. The last two terms depend on the occupation matrix of the correlated orbitals of the system under consideration. In this study, the calculated Hubbard U_{eff} parameter (henceforth referred to as the Hubbard U) is optimized with respect to the experimentally determined lattice constant for each of the actinide nitrides that we considered. The optimized U parameter is used to determine the structural, electronic, elastic and mechanical properties of the compounds. This results in a better qualitative and quantitative description of the various properties.

Relativistic effects are important for the actinides. This leads to lower calculated ground state total energies compared to non-relativistic calculations. In this study, we present results using the GGA and the GGA + U forms for the exchange correlation potential together with spin-polarization (SP) and spin orbit coupling (SOC).

A method using the least squares fit, [30] as implemented in the MedeA-MT module, was used to obtain the elastic constants. The elastic properties are calculated from the Hill values, which are a geometric mean of the Voigt and Reuss values. The eigenvalues of the stiffness matrix give an indication of the mechanical stability of the systems under consideration. The Hill values [31] were used in the estimation of longitudinal, shear and mean sound velocities and the Debye temperatures. [32]

The energy of formation for each structure was calculated by taking the difference between the total energy of the actinide compound and the energies of its constituents in their corresponding bulk elemental forms:

$$\Delta E_f = E^{tot}_{(AcN_n)} - N_{Ac}\, E^{bulk}_{(Ac)} - N_N\, E^{bulk}_{(N)}\,, \tag{2}$$

where n is either 1 or 2 for the mononitride and dinitride, respectively, and N_{Ac} and N_N are the number of Ac atoms and N atoms in the calculational unit cell of the compound, respectively. $E^{bulk}_{(Ac)}$ is the energy per Ac atom in its ground state structure, and $E^{bulk}_{(Ac)}$ is the energy per N atom in the nitrogen molecule.

The phonon frequencies are calculated using the direct approach of lattice dynamics based on linear response theory, as implemented in the MedeA-PHONON package. [33] This exploits the fact that within the harmonic regime, there is a linear relationship between the induced forces on the atoms and the displacement of the atoms from their equilibrium positions. We discovered that using GGA + U only has a marginal effect on the quantitative description of the phonon frequencies. Therefore, we have only presented results for the phonon frequencies within the GGA approximation.

We applied our methods to the study of the ferromagnetic (FM) and the antiferromagnetic (AFM) configurations for the actinide mononitrides and dinitrides. The non-magnetic (NM) systems consistently resulted in higher energies of formation for all the structures considered. Therefore NM results are not presented in this study.

3. AcN

The AcN crystal structures are presented in Fig. 1. The ferromagnetic phase is the cubic NaCl structure with the *Fm-3m* space group, and the antiferromagnetic phase is cubic NaCl with the *Pm3m* space group.

3.1. Energy of Formation

In Table 1, the calculated equilibrium lattice constant, energy of formation, magnetic moment, bulk and shear moduli, and Debye temperature are presented. The energy of formation for all the AcN investigated, calculated using equation 2, is negative. This implies that the formation of these structures is energetically favorable.

Also, in Table 1 we observe that ThN and PaN evolve to their non-magnetic ground states with the AFM structure being slightly more energetically favorable than the FM structure. UN to PuN give various degrees of magnetization due to the 5*f* orbitals, with the magnetic orientation along the z-axis in both the AFM and FM ordering. This is attributed to strong electron-electron correlations of the 5*f* electrons at each atomic site resulting in net local magnetic moments. We observe that the degree of magnetization is over-estimated using the PAW (GGA + U) approach compared to all-electron (AE) calculations and experimental data. For the UN to PuN compounds, the total energy with PAW (with and without the Hubbard U) results in the FM structure having the lowest energy of formation.

Table 1: The Hubbard U (eV), optimize lattice parameters a (in Å), calculated energy of formation ΔE_f (eV), total magnetic moment μ_B (Bohr magnetons), bulk and shear moduli (GPa), and the Debye temperature θ_D (K) using GGA + U within the SOC scheme. Where AE results is from Ref [21] and the PAW results is our data.

Compound	Method	Theory	U	a_0	ΔE_f	μ_B	bulk	shear	θ_D
ThN	PAW	AFM+SOC	0	5.172	-3.048	0	178	83	340.7
		FM+SOC	0	5.171	-3.040	0	178	82	338.4
	AE	AFM+SOC	0	5.175	–	0	170	–	–
		FM+SOC	0	5.175	–	0	162	–	–
PaN	PAW	AFM+SOC	0	4.952	-3.225	0	219	95	358
		FM+SOC	0	4.951	-3.228	0	220	88	345.8
		AFM+SOC	1	4.965	-2.636	0	223	102	371.1
		FM+SOC	1	4.965	-2.639	0	224	94	357.3
	AE	AFM+SOC	0	4.947	–	0	200	–	–
		FM+SOC	0	4.953	–	0	210	–	–
UN	PAW	AFM+SOC	0	4.871	-2.643	0	201	72	305.2
		FM+SOC	0	4.872	-2.663	1.0976	206	85	316.2
		AFM+SOC	1	4.903	-1.685	0	196	63	288.5
		FM+SOC	1	4.889	-1.713	1.3713	198	52	262.9
	AE	AFM+SOC	0	4.873	–	0	221	–	–
		FM+SOC	0	4.873	–	0.96	219	–	–
NpN	PAW	AFM+SOC	0	4.863	-2.299	0	178	78	317.3
		FM+SOC	0	4.859	-2.341	2.4658	178	79	320.4
		AFM+SOC	1	4.897	-1.268	0	167	71	303.5
		FM+SOC	1	4.909	-1.299	3.0399	145	49	253.1
	AE	AFM+SOC	0	4.863	–	0	195	–	–
		FM+SOC	0	4.863	–	2.45	183	–	–
PuN	PAW	AFM+SOC	0	4.907	-6.580	0	159	86	328.1
		FM+SOC	0	4.916	-6.404	4.2438	147	89	335
	AE	AFM+SOC	0	4.9531	–	0	141	–	–
		FM+SOC	0	4.9740	–	4.26	145	–	–

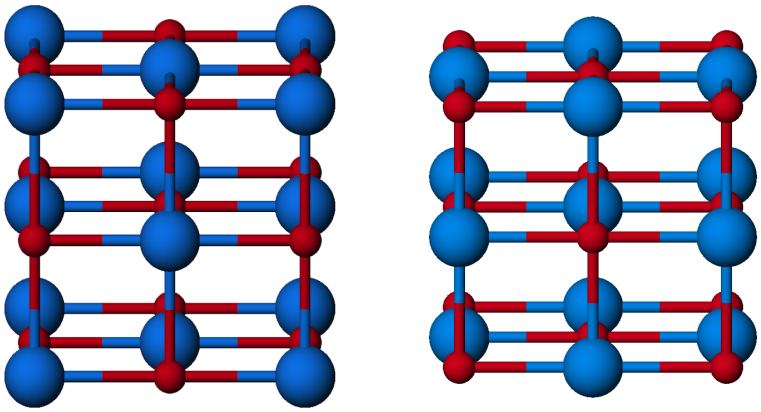

(a) AcN-fm (b) AcN-afm

Figure 1: Crystal Structure for AcN compounds in the FM and AFM phase

3.2. Structural Properties

We present the lattice constants calculated using the PAW method (GGA with and without the inclusion of Hubbard U-parameter) in Table 1. We find a favorable comparison with the AE [21] results for the various AcN compounds considered. For ThN, we obtain reasonable results without the inclusion of the Hubbard U parameter. This is understandable since Th lacks 5*f* electrons. Also for PuN, the lattice constant is not affected much by the inclusion of the U. This is understood in terms of its relative position in the actinide series.

The inclusion of the Hubbard U parameter of 1 eV in UN and NpN results in lattice constants that compare very well with experiment. The experimentally determined lattice constant [34, 35] and the calculated result of our lowest energy structure in parenthesis for ThN, UN, NpN and PuN are 5.154 Å (5.172 Å), 4.889 Å (4.889 Å), 4.894 Å (4.909 Å) and 4.905 Å (4.907 Å) respectively.

3.3. Elastic Properties

The calculated bulk modulus, shear modulus and Debye temperature for the AcN compounds are presented in Table 1. They are all positive, which indicates that the compounds are all elastically stable. The inclusion of the U parameter leads to an overall better agreement of the calculated elastic properties with other available theoretical and experimental data [35, 36, 21, 7]. For instance, the experimentally determined bulk modulus and the calculated result of our lowest energy structure in parenthesis for ThN and UN are 175 GPa [37] (178 GPa) and 193 GPa [35] (198 GPa) respectively.

PaN has the highest Debye temperature θ_D of 358 K of the systems that we considered. This is associated with complex covalent bonding behavior in this system that will be further explored in our discussion on the valence charge density. PaN, followed by UN, have the highest calculated bulk modulus that also points to the inherent covalent bonding in these systems.

3.4. Density of States

The partial density of states (PDOS) for the 5*f* and 6*d* states for the actinides and the 2*p* states of the nitrogen are presented for the ground state AcN compounds. All the compounds studied within GGA and GGA + *U* are found to be metallic. There is a systematic increase in the 5*f* electron density of states at the Fermi level with increasing atomic number, and there is a contribution from the N 2p states below the Fermi level.

As shown in Fig. 2 for the AFM structure of ThN, the metallicity of ThN is determined mainly by the hybridization of the 5*f* and 6*d* states from the actinide with a very minute contribution from 2*p* states of the nitrogen at the Fermi level.

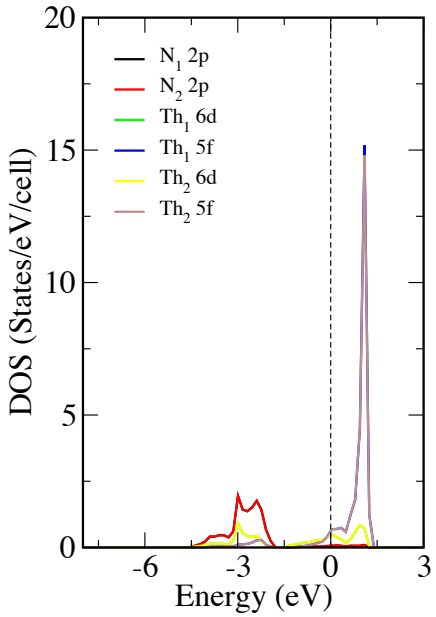

Figure 2: (Color online) Partial density of states for ThN in the AFM structure. The Fermi level is the vertical line through E = 0

From PaN to PuN, we have a higher 5*f* electron contribution at the Fermi level compared to the other orbitals in both the GGA and GGA + *U* descriptions shown in figures 3. This is attributed to increased localization of the 5*f* electrons in the actinides. However, other experimental and theoretical studies [13, 14, 6] of UN have confirmed that the U 5*f* states have some itinerant character that is attributed to the presence of U 5*f* states at the Fermi-level therefore preserving some band character. [14]

In Fig 4, we present the partial DOS for PuN in the AFM structure. There is a significant difference in the peaks of the two actinide atoms of the 5*f* states (minority and majority spin) compared to the AFM PDOS of ThN that has no difference in the peaks. This is an indication of AF magnetic ordering in this system. Similar features are observed in the AFM structure of UN to PuN.

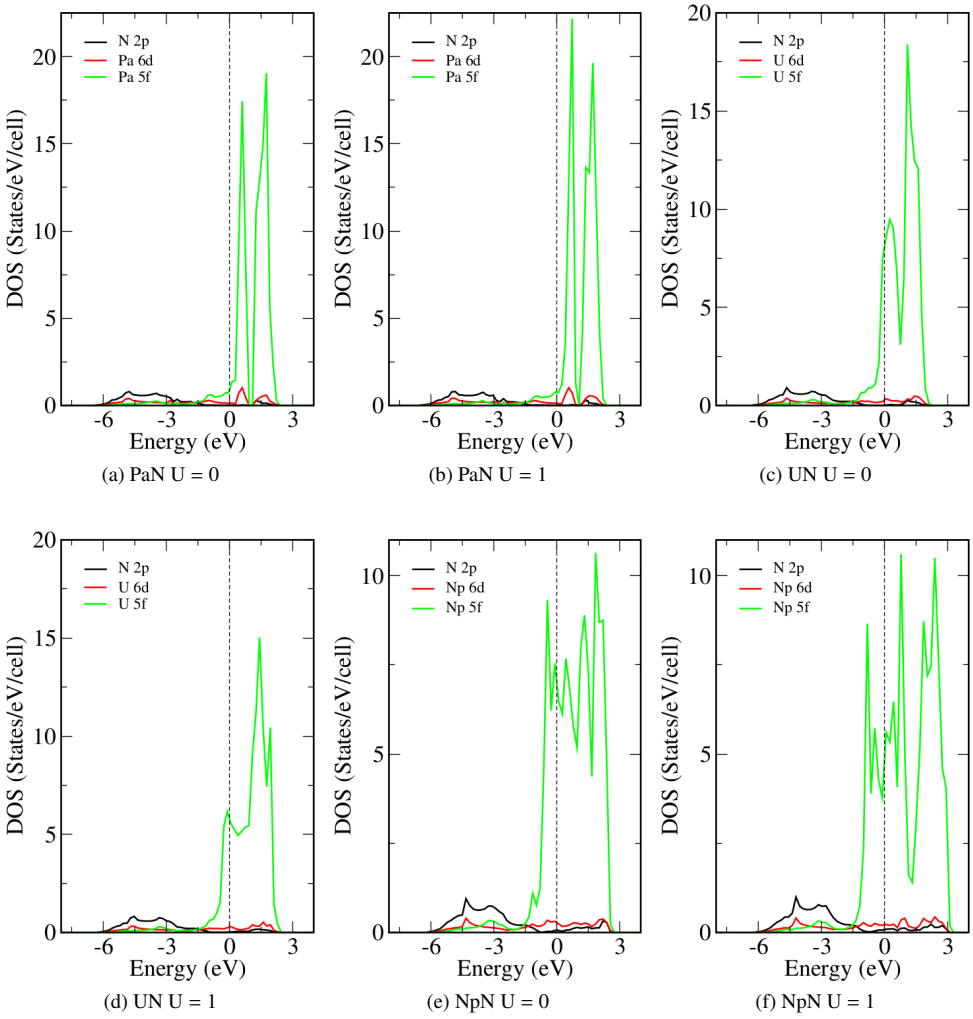

Figure 3: (Color online) Partial density of states for PaN, UN and NpN in the FM structure. The Fermi level is the vertical line through E = 0

3.5. Valence charge densities

In Fig. 5, we show the valence charge density plots for the compounds that we investigated. This gives us an indication of the character of the bonding. The charge density distribution is computed in the (001) plane for the AFM configuration. The scale in Fig. 5f is such that blue is devoid of electrons and red indicates a high concentration of electrons. The charge densities plotted are for the valence states summed over both spin orientations.

In general, we observe near-spherical charge density distributions around the actinide and nitrogen atoms with significant charge depletion between the atoms, which is characteristic of the rock-salt structure with predominant ionic bonding. Between the actinide and nitrogen

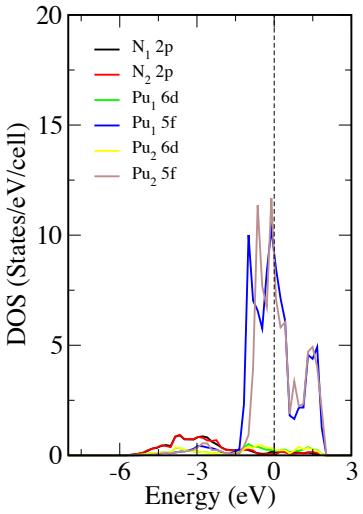

Figure 4: (Color online) Partial density of states for PuN in the AFM structure. The Fermi level is the vertical line through E = 0

atoms there is a subtle charge density bridge, attributed to the slight covalent character in the actinide nitrides. There is charge transfer from the actinide metals to the non-metallic nitrogen atoms. As the atomic number increases (Th to Pu) resulting in higher valence localized 5*f* electrons, there is a noticeable increase in the charge accumulation at the actinide site.

3.6. Phonon Studies

In Fig. 6, no negative phonon modes for the various AcN structures are observed in the phonon dispersion plot. Therefore, these compounds are dynamically stable. The low-lying frequency modes are governed by the dynamics of the heavy Ac atoms, and the higher frequencies by the lighter N atoms. There is a significant difference in the frequency of N atoms compared to the Ac atoms due to the large mass differences. This suggests that instability in the system can arise from a small perturbation of the crystal structure.

PuN has the lowest acoustic velocity corresponding to the lowest bulk modulus and overall strength of all the AcN systems that we studied. There are ”flatish” sections of the optical branches in all systems that suggest low group velocities for these modes involving N.

4. AcN_2

In Fig. 7, we present the AcN_2 crystal structures. The ferromagnetic (FM) phase is the cubic fluorite structure with space group *Fm-3m*, while the antiferromagnetic phase (AFM) is a double tetragonal unit cell with space group *P4/mmm*, and the magnetic ordering is in the z-axis.

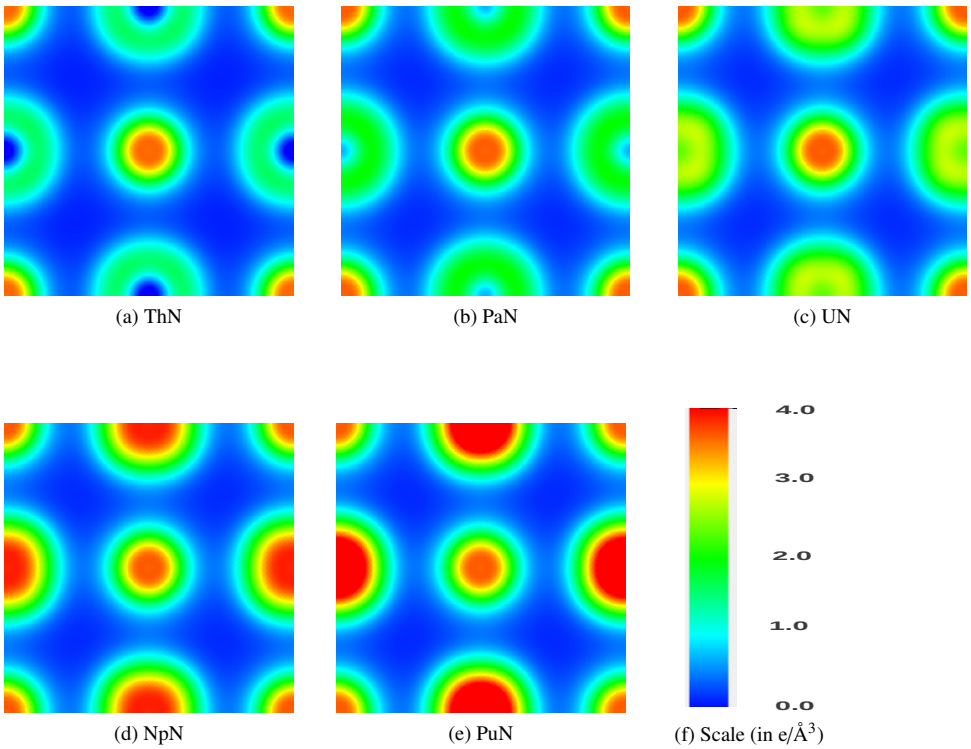

(a) ThN (b) PaN (c) UN

(d) NpN (e) PuN (f) Scale (in e/Å^3)

Figure 5: Valence charge density in the (001) direction of the AFM structure for AcN crystalline structures, where the charge distribution at the center and corner of the slice is from N atom, and that at face of the slice is from the Ac atom. Color scale: deep blue represents low valence charge while red represents a high concentration of valence charge.

4.1. Energy of Formation

In Table 2, the calculated equilibrium lattice constant, energy of formation, magnetic moment, bulk and shear moduli, and Debye temperature are presented. The calculated energy of formation for the AcN_2, using equation 2, is negative, which implies that the structures are energetically favorable. The difference in the energy of formation of the AcN_2 within the GGA approach using the AFM and FM structures is about one-hundredth of an eV. The introduction of the Hubbard *U* parameter results in a difference of about one-tenth of an eV in the energy of formation between the AFM and the FM structures. We conclude that the AFM structures are slightly more energetically favorable with the exception of ThN_2 for which the FM is more energetically favorable.

ThN_2 to UN_2 compounds evolve to the non-magnetic ground state irrespective of the starting magnetic configuration. We observe that the magnetic orientation has little effect on the structural, elastic and mechanical properties. For NpN_2 and PuN_2, the AFM structure results in zero net magnetization. But, the FM structure for NpN_2 gives a net magnetic

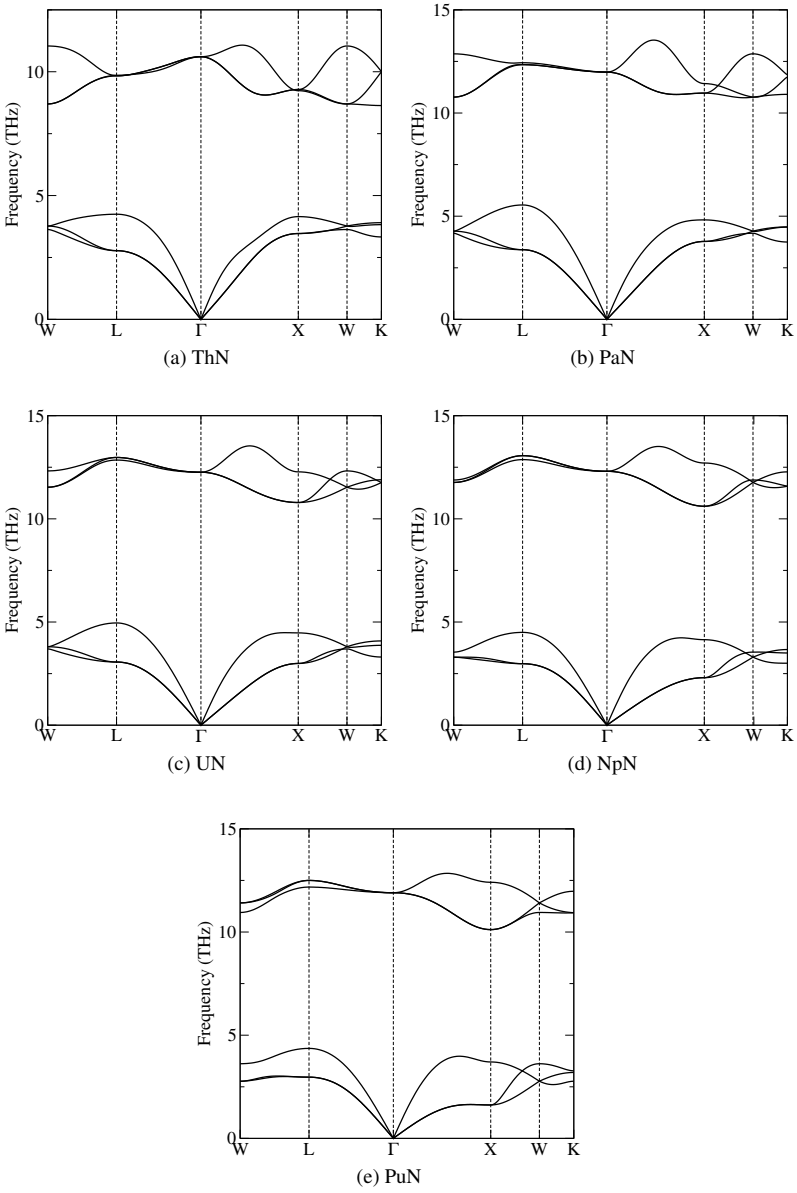

Figure 6: Phonon dispersion for AcN crystalline structures

moment of 0.19 μ_B and 0.95 μ_B for GGA and GGA + U respectively. The FM structure for PuN_2 gives a net magnetic moment of 1.74 μ_B for GGA and 2.04 μ_B for GGA + U. The magnetic orientation in these compounds is along the z-axis.

Comparing the energy of formation for the actinide mononitrides and dinitrides, we observe that the dinitrides are more energetically stable with the exception of ThN_2 that is later shown to be elastically unstable. PuN_2 has a slightly lower energy of formation than

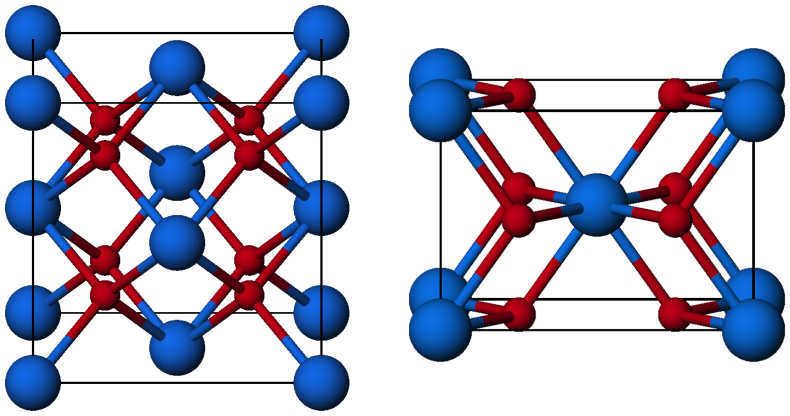

(a) AcN_2-fm (b) AcN_2-afm

Figure 7: Crystal Structure for AcN_2 compounds in the FM and AFM phase

PuN.

4.2. Structural Properties

In Table 2, we present the calculated equilibrium lattice constant, magnetic moment, bulk and shear moduli and Debye temperature. The lattice constant using the PAW approach obtained for the various AcN_2 compounds considered is calculated using GGA and GGA + U. The experimentally determined lattice constant and the calculated result with the Hubbard U parameter of our lowest energy structure in parenthesis for UN_2 [34, 38] and NpN_2 [4] are 5.308 Å (5.302 Å) and 5.3236 Å (5.32 Å) respectively. To the best of our knowledge, no experimental data on the lattice parameters of ThN_2, PaN_2 and PuN_2 is available.

4.3. Elastic properties

The AcN_2 considered are all elastically stable except for ThN_2, which is elastically unstable to shear stress due to the negative shear modulus. The Debye temperature therefore cannot be calculated for this system. This is consistent with experimental findings that suggest the existence of two stable alloys of thorium and nitrogen, namely ThN and Th_3N_4. [39]

The bulk and shear moduli increases from ThN_2 to UN_2, then subsequently decreases to PuN_2. The calculated bulk modulus, shear modulus and Debye temperature with and without the U parameter for PaN_2 and UN_2 are consistent for the AFM and the FM phases as shown in Table 2. Also, for NpN_2 without the U parameter, the elastic properties are consistent for the AFM and FM phase. However, we discovered that the FM phase for both NpN_2 and PuN_2 are highly sensitive to structural optimization, which leads to significant structural distortion.

4.4. Density of States

The partial density of states (PDOS) for the 5*f* and 6*d* states for the actinide atom and the 2*p* states of the nitrogen atom is presented for AcN_2 in the ground state structures. We observe

Table 2: The Hubbard U (eV), optimize lattice parameters a (in Å), calculated energy of formation ΔE_f (eV), total magnetic moment (scalar norm) μ_B (Bohr magnetons), bulk and shear moduli (GPa), and the Debye temperature θ_D (K) using GGA + U within the SOC scheme.

Compound	Theory	U	a_0	ΔE_f	μ_B	bulk	shear	θ_D
ThN2	AFM+SOC	0	5.660	-1.590	0.00	145.6	-9.4	–
	FM+SOC	0	5.664	-1.636	0.00	150.0	-4.3	–
PaN2	AFM+SOC	0	5.429	-3.777	0.00	214.3	89.8	405.7
	FM+SOC	0	5.418	-3.762	0.00	217.3	89.2	404.5
	AFM+SOC	2	5.460	-2.551	0.00	216.9	87.1	401.1
	FM+SOC	2	5.451	-2.532	0.00	217.3	81.5	388.5
UN2	AFM+SOC	0	5.275	-4.094	0.00	249.8	98.1	413.3
	FM+SOC	0	5.271	-4.072	0.00	250.0	98.5	414.1
	AFM+SOC	2	5.302	-2.135	0.00	249.2	89.1	395.7
	FM+SOC	2	5.297	-2.088	0.00	251.7	89.3	396.0
NpN2	AFM+SOC	0	5.223	-3.089	0.00	235.2	93.7	402.4
	FM+SOC	0	5.219	-3.015	0.19	237.4	94.3	403.7
	AFM+SOC	3	5.320	0.086	0.00	198.6	68.4	347.5
	FM+SOC	3	5.307	0.518	0.95	193.3	86.5	408.6
PuN2	AFM+SOC	0	5.215	-6.217	0.00	203.9	56.2	309.5
	FM+SOC	0	5.222	-6.209	1.74	209.6	74.4	354.7
	AFM+SOC	3	5.321	-3.303	0.00	149.3	39.6	263.8
	FM+SOC	3	5.351	-2.854	2.04	163.2	68.1	342.6

that AcN_2 within the GGA and GGA + U are metallic with the exception of UN_2 which has a band gap.

In Fig. 10, an insulating character is observed for UN_2 with a GGA band gap of 0.56 eV and an increase in the band gap to 0.64 eV on the inclusion of the Hubbard U of 2 eV. This is comparable to the band gap obtained by Weck *et al.* [22] of 0.94 eV using the AE approach and by Lu *et al.* [7] of 0.75 eV using a Hubbard U of 4 eV. If we consider the FM structure, which is less energetically favorable, a GGA band gap of 0.73 eV and a band gap of 0.83 eV on inclusion of the Hubbard U of 2 eV (figure not presented) is obtained. The top of the valence band is determined mainly by the hybridization of the U 5*f* and N 2*p* states, while the electronic properties of UN_2 is governed mainly by the 5*f* states because they dominate the conduction band minimum and valence band maximum.

The metallicity of ThN_2 is determined mainly by the 2*p* states as shown in Fig. 8. There is significant hybridization of the 5*f* and 6*d* states for the thorium atom and the 2*p* states of the nitrogen atom at the Fermi level.

While in PaN_2 as shown in Fig. 9, there is approximately equal participation of the 5*f* and 6*d* states around the Fermi level compared to the other orbitals in both the GGA and GGA + U. The inclusion of the Hubbard U of 2 eV leads to an increase in the 5*f* states in the conduction band but no noticeable change at the Fermi level.

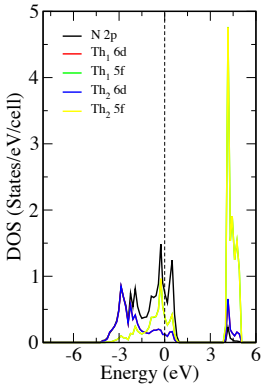

Figure 8: (Color online) Partial density of states for ThN_2. The Fermi level is the vertical line through E = 0

The NpN_2 and PuN_2 compounds results in metallic behavior as presented in Fig. 11 and 12 with the Fermi level dominated by the 5*f* states. There is weak hybridization of the actinide 5*f* and 6*d* states at the Fermi-level in NpN_2 and a significant hybridization of the actinide 5*f* and 6*d* states with the nitrogen 2*p* state in PuN_2 compound.

4.5. Valence charge densities

In Fig. 13, we show the valence charge density plots for all the compounds considered to investigate the bonding character. The density distribution is computed in the (100) plane for the AFM configuration. We observe that the bonding character is not dependent on the magnetic configuration of the systems that we investigated. The scale in Fig. 13f is such that blue is devoid of electrons and red indicates a high concentration of electrons. The charge densities plotted are for the valence states summed over both spin orientations.

We observe significant distortion in the spherical charge distribution around the actinide compared to the nitrogen atoms. Between the actinide and nitrogen atom there is a subtle charge density bridge, attributed to the slight covalent character in the actinide nitrides. This charge density bridge along with the actinide charge density increases with increase in the atomic number of the actinide metal (Th to Pu) compared to the rest of the interstitial region. This results in increased covalent bonding character of the actinide nitride with increase in the atomic number. However, the AcN_2 studied are all predominantly ionic compounds.

4.6. Phonon Studies

The calculated phonon dispersion curves along the W-L-Γ-X-W-K directions for AcN_2 are presented in Fig. 14 within the GGA approach. Generally, the phonon frequencies for all the compounds considered are split roughly into two halves, where the lower frequencies are governed by the dynamics of the heavy Ac atoms and the higher frequencies by the dynamics of the N atoms.

The AcN_2 are dynamically stable with no negative phonon modes in the dispersion plot with the important exception for UN_2, which has a small fraction of imaginary phonon frequencies. This is due to the transverse modes of the nitrogen atoms.

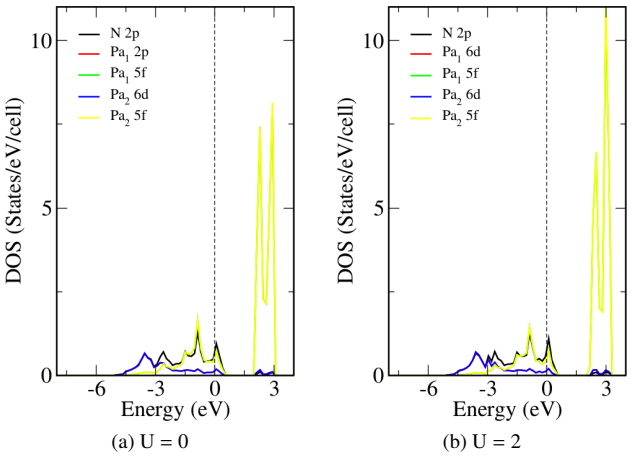

Figure 9: (Color online) Partial density of states for PaN_2. The Fermi level is the vertical line through E = 0

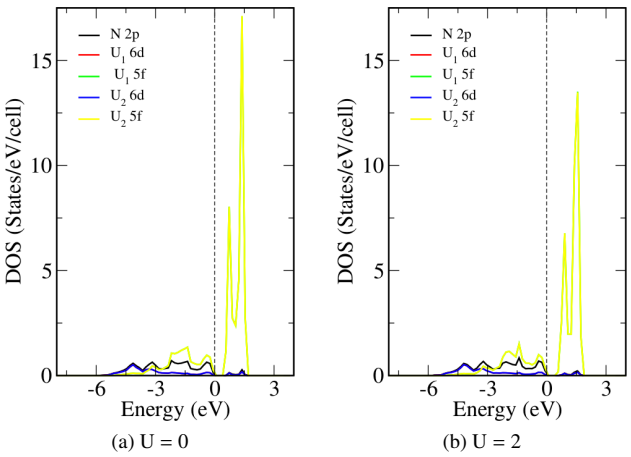

Figure 10: (Color online) Partial density of states for UN_2. The Fermi level is the vertical line through E = 0

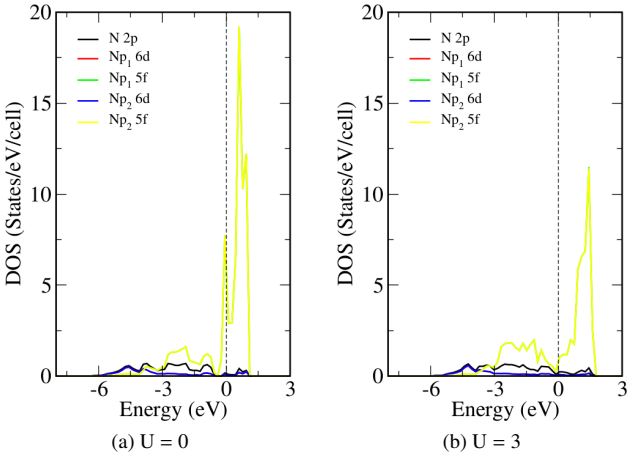

Figure 11: (Color online) Partial density of states for NpN_2. The Fermi level is the vertical line through E = 0

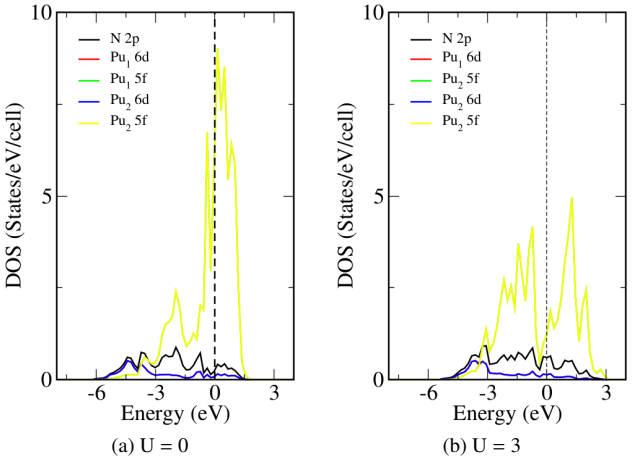

Figure 12: (Color online) Partial density of states for PuN_2. The Fermi level is the vertical line through E = 0

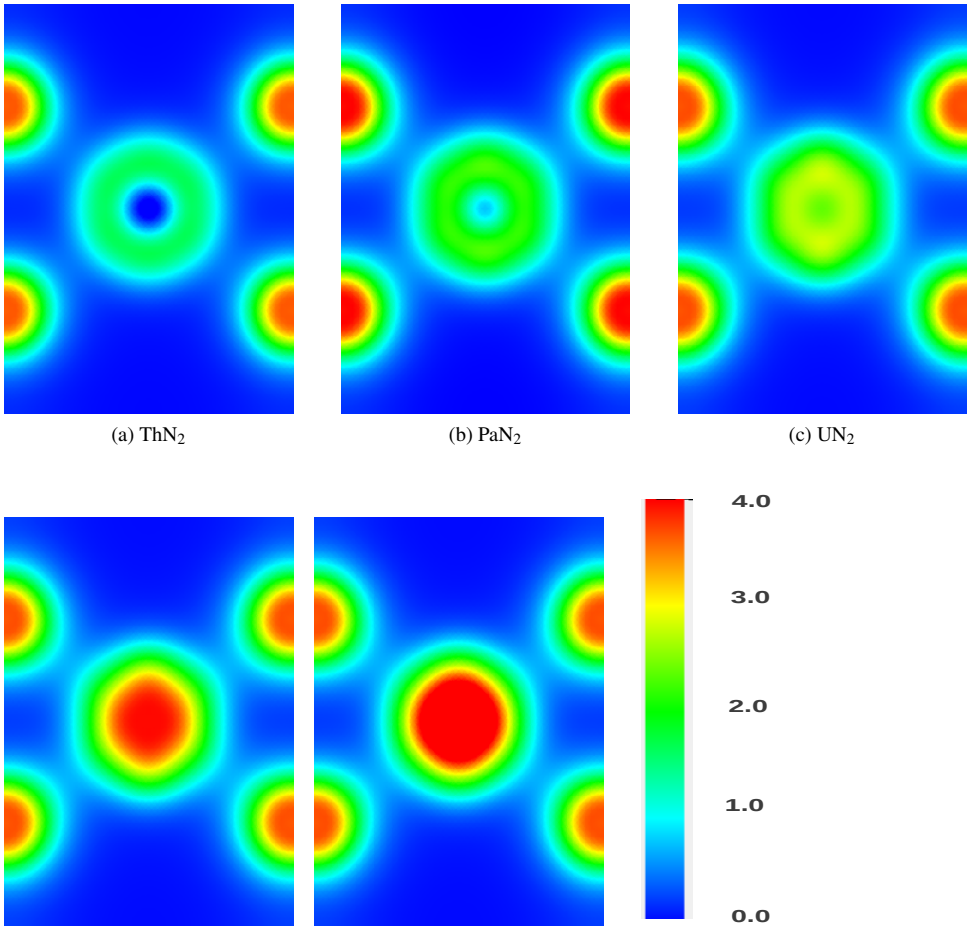

(a) ThN_2 (b) PaN_2 (c) UN_2

(d) NpN_2 (e) PuN_2 (f) Scale (in e/Å^3)

Figure 13: Valence charge density in the (100) direction of the AFM structure for AcN_2 crystalline structures, where the charge distribution at the center of the slice is from Ac atom and that at face of the slice is from the N atom. Color scale: deep blue represents low valence charge while red represents a high concentration of valence charge.

This result contradicts the theoretical observation by Lu *et al.*[40] that predicts a thermodynamically stable structure for UN_2. Our result corroborates experimental evidence by Rundle *et al.* [34], Tagawa *et al.* [15, 16] and more recent studies [41, 42] that suggests UN_2 has never been prepared as a stoichiometric compound. Experimentally, it has been concluded that the correct stoichiometry may be $UN_{1.75}$. UN_2 is nonstoichiometric and was assigned a hypothetical CaF structure on the basis of the experimental data for the actinide dinitrides with N/U= 1.75 – 1.78 with the understanding that the non-stoichiometry arises from the presence of nitrogen vacancies in UN_2. This is consistent with our theoretical observation that the nitrogen atom is the source of the instability.

A trend of reduced gap in the phonon frequency between the modes of the heavy actinide

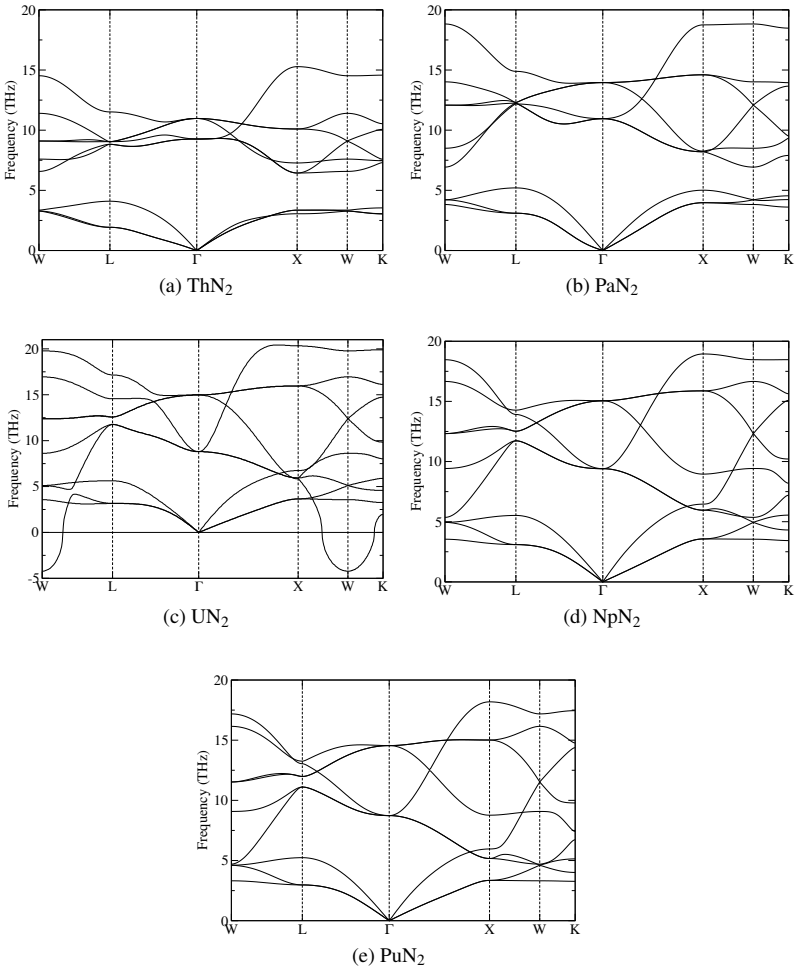

Figure 14: Phonon dispersion for AcN_2 crystalline structures

metal and the light nitrogen atom is observed with increasing atomic number. Also, the difference in the frequency of nitrogen atoms compared to the actinide atoms is low compared to their AcN analogue. This implies that the addition of the extra nitrogen atom to the structure has led to the further stabilization of the structure.

5. Concluding remarks

We studied the ground state electronic, structural and mechanical properties of the AcN and AcN_2 early actinide nitrides. The calculated lattice parameters with the inclusion of the Hubbard U parameter agree well with available experimental data where that data exists. There is the exception of ThN, PuN and ThN_2 compounds where GGA gives agreeable results for the actinide mononitrides and dinitrides. In general, all the actinide nitrides studied are energetically favorable, and are elastically and mechanically stable with the exception of ThN_2

that is unstable to isotropic pressure. Notably UN_2 is thermodynamically unstable and has been speculated to stabilize under N-vacancy formation. This will be investigated in a future study.

Comparison of the calculated and experimental magnetic properties of these systems shows that the GGA + U with and without SOC gives a good qualitative account of the properties compared with experiment, but not an accurate quantitative account. Therefore, going beyond DFT + U is important to quantitatively determine the magnetic moments.

An analysis of the valence charge density distribution of the actinide nitrides shows the presence of ionic bonding predominantly, with the dinitrides having higher covalent character compared to the mononitrides. Also, we observe a consistent increase in the charge density distribution at the actinide sites for the actinide mononitrides and dinitrides with increasing atomic number.

All the actinide nitrides considered are metallic in nature with the exception of UN_2.

Acknowledgments

We thank the University of Pretoria for financial support. KO gratefully acknowledges the support of Obodo T. Joshua and the members of the Computational and Theoretical Physics group at the University of Pretoria for useful discussions. Also, we thank Dr Jannie Pretorius and Prof. Walter Meyer for assistance with the computational hardware and software resources. Finally, NC is grateful to the National Institute for Theoretical Physics for support.

References

[1] V G Baranov, Yu N Devyatko, A V Tenishev, A V Khlunov, and O V Khomyakov. A physical model for evaluating uranium nitride specific heat. *Journal of Nuclear Materials*, 434:248–251, 2013.

[2] Kezhao Liu, Ren Bin, Hong Xiao, Zhong Long, Zhanglian Hong, Hui Yang, and Sheng Wu. Applied Surface Science Structural analysis of nitride layer formed on uranium metal by glow plasma surface nitriding. *Applied Surface Science*, 265:389–392, 2013.

[3] K O Obodo and N Chetty. First principles LDA + U and GGA + U study of protactinium and protactinium oxides: dependence on the effective U parameter. *Journal of Physics: Condensed Matter*, 25(145603):1–12, April 2013.

[4] G W Chinthaka Silva, Philippe F Weck, Eunja Kim, Charles B Yeamans, Gary S Cerefice, Alfred P Sattelberger, and Kenneth R Czerwinski. Crystal and Electronic Structures of Neptunium Nitrides Synthesized Using a Fluoride Route. *Journal of The American Chemical Society*, 134:3111–3119, 2012.

[5] Hiroki Shibata, Tomohito Tsuru, Tsuyoshi Nishi, Masaru Hirata, and Yoshiyuki Kaji. Thermodynamic properties of neptunium nitride : a first principles study. *Journal of Nuclear Science and Technology*, 49(3):328–333, 2012.

[6] Shin-ichi Fujimori, Takuo Ohkochi, Tetsuo Okane, Yuji Saitoh, Atsushi Fujimori, Hiroshi Yamagami, Yoshinori Haga, Etsuji Yamamoto, and Yoshichika Onuki. Itinerant nature of U 5f states in uranium mononitride revealed by angle-resolved photoelectron spectroscopy. *Physical Review B*, 86(23):235108, 2012.

[7] Yong Lu, Da-Fang Li, Bao-Tian Wang, Rong-Wu Li, and Ping Zhang. Electronic structures, mechanical and thermodynamic properties of ThN from first-principles calculations. *Journal of Nuclear Materials*, 408:136–141, January 2011.

[8] Hiroki Shibata, Tomohito Tsuru, Masaru Hirata, and Yoshiyuki Kaji. First principles study on elastic properties and phase transition of NpN. *Journal of Nuclear Materials*, 401(1-3):113–117, June 2010.

[9] L. Petit, A. Svane, Z. Szotek, W. M. Temmerman, and G. M. Stocks. Ground-state electronic structure of actinide monocarbides and mononitrides. *Physical Review B*, 80(04):045124(8), July 2009.

[10] A. O. Shorikov, A. V. Lukoyanov, M. A. Korotin, and V. I. Anisimov. Magnetic state and electronic structure of the δ and α phases of metallic Pu and its compounds. *Physical Review B*, 72(02):024458(18), July 2005.

[11] K Kurosaki, J Adachi, M Uno, and S Yamanaka. Molecular dynamics studies of actinide nitrides. *Journal of Nuclear Materials*, 344:45–49, September 2005.

[12] L Black, F Miserque, T Gouder, L Havela, J Rebizant, and F Wastin. Preparation and photoelectron spectroscopy study of UNx thin films. *Journal of Alloys and Compounds*, 315:36–41, 2001.

[13] T Gouder, L Havela, L Black, F Wastin, J Rebizant, and Boulet P. Synthesis and electronic properties of ThN films. *Journal of Alloys and Compounds*, 336:73–76, April 2002.
[14] M Samsel-Czekala, E Talik, P. de V. Du Plessis, R Troć, H Misiorek, and C SuÅkowski. Electronic structure and magnetic and transport properties of single-crystalline UN. *Physical Review B*, 76(14):144426, 2007.
[15] Hiroaki Tagawa. Phase Relations and Thermodynamic Properties of the Uranium-Nitrogen system. *Journal of Nuclear Materials*, 51:78–89, 1974.
[16] Hiroaki Tagawa and Norio Masaki. X-ray and Density studies of nonstoichiometric Uranium sesquinitride. *Journal of Inorganic and Nuclear Chemistry*, 36:1099–1103, 1974.
[17] D Sedmidubsky and P Nova. Calculation of enthalpies of formation of actinide nitrides. *Journal of Nuclear Materials*, 344:40–44, 2005.
[18] Vladimir I. Anisimov, Jan Zaanen, and Ole K. Andersen. Band theory and Mott insulators: Hubbard U instead of Stoner I. *Physical Review B*, 44(3):943–954, 1991.
[19] A. I. Liechtenstein, V. I. Anisimov, and J. Zaanen. Density-functional theoy and strong interactions: Orbital ordering in Mott-Hubbard insulators. *Physical Review B*, 52(8):R5467–R5471, 1995.
[20] V I Anisimov, F Aryasctiawan, and A I Lichtenstein. First-principles calculations of the electronic structure and spectra of strongly correlated systems : the LDA + U method. *Journal of Physics: Condensed Matter*, 767:767–808, 1997.
[21] Raymond Atta-Fynn and Asok K. Ray. Density functional study of the actinide nitrides. *Physical Review B*, 76(11):115101(12), September 2007.
[22] Philippe F Weck, Eunja Kim, Naduvalath Balakrishnan, Charles B Yeamans, and Kenneth R Czerwinski. First-principles study of single-crystal uranium mono- and dinitride. *Chemical Physics Letters*, 443:82–86, 2007.
[23] Denis Gryaznov, Eugene Heifets, and David Sedmidubsky. Density functional theory calculations on magnetic properties of actinide compounds. *Physical chemistry chemical physics : PCCP*, 12:12273–12278, October 2010.
[24] P. Hohenberg and W. Kohn. Inhomogeneous Electron Gas. *Physical Review*, 136(3B):B864–B871, 1964.
[25] G Kresse and J Furthmuller. Efficient iterative schemes for ab initio total-energy calculations using a plane-wave basis set . *Physical Review B*, 54(16):11169–11186, 1996.
[26] G Kresse and D Joubert. From ultrasoft pseudopotentials to the projector augmented-wave method. *Physical Review B*, 59(3):1758–1775, 1999.
[27] John P Perdew, Kieron Burke, and Matthias Ernzerhof. Generalized Gradient Approximation Made Simple. *Physical Review Letters*, 77(18):3865–3868, 1996.
[28] Hendrik J Monkhorst and James D Pack. Special points for Brillouin-zone integration*. *Physical Review B*, 13(12):5188–5192, 1976.
[29] S L Dudarev, G A Botton, S Y Savrasov, C J Humphreys, and A P Sutton. Electron-energy-loss spectra and the structural stability of nickel oxide: An LSDA + U study. *Physical Review B*, 57(3):1505–1509, 1998.
[30] Yvon Le Page and Paul Saxe. Symmetry-general least-squares extraction of elastic data for strained materials from ab initio calculations of stress. *Physical Review B*, 65(10):104104(14), 2002.
[31] R Hill. The Elastic Behaviour of a Crystalline Aggregate. *Proceedings of the Physicsal Society. Section A*, 65(5):349–354, 1952.
[32] Orson L Anderson. A SIMPLIFIED METHOD FOR CALCULATING THE DEBYE TEPERATURE FROM ELASTIC CONSTANTS. *Journal of Physics and Chemistry of Solids*, 24:909–917, 1963.
[33] K Parlinski, Z. Q. Li, and Y Kawazoe. First-Principles Determination of the Soft Mode in Cubic ZrO 2. *Physical Review Letters*, 78(21):4063(4), 1997.
[34] R E Rundle, N C Baenziger, A S Wilson, and R A McDonald. The Structures of the Carbides, Nitrides and Oxides of Uranium. *Journal of American Chemical Society*, 70(1):99–105, 1948.
[35] M S S Brooks and P J Kelly. Large Oribtal-Moment COntribution to 5f Band Magnetism. *Physical Review Letters*, 51(18):1708–1711, 1983.
[36] I Shein, K Shein, and A Ivanovskii. First-principle study of B1-like thorium carbide, nitride and oxide. *Journal of Nuclear Materials*, 353:19–26, July 2006.
[37] L GERWARD, J STAUN OLSEN, U. BENEDICT, J P ITIE, and J. C. SPIRLET. The Crystal Structure and the Equation of State of Thorium Nitride for Pressures up to 47 GPa. *Journal of Applied Crystallography*, 18:339–341, 1985.
[38] R Didchenko and F P Gortsema. Magnetic and Electric Properties of Monosulfides and Mononitrides of Thorium and Uranium. *Inorganic chemistry*, 2:1079–1080, 1963.
[39] I.R. Shein and A.L. Ivanovskii. THORIUM COMPOUNDS WITH NON-METALS ELECTRONIC STRUCTURE, CHEMICAL BOND, AND PHYSICOCHEMICAL PROPERTIES. *Journal of Structural Chemistry2*, 49(2):348–370, May 2008.
[40] Yong Lu, Bao-tian Wang, Rong-wu Li, Hong-liang Shi, and Ping Zhang. Structural, electronic, mechanical, and thermodynamic properties of UN2: Systematic density functional calculations. *Journal of Nuclear Materials*, 410:46–51, 2011.
[41] G W Chinthaka Silva, Charles B Yeamans, Alfred P Sattelberger, Thomas Hartmann, Gary S Cerefice, and

Kenneth R Czerwinski. Reaction Sequence and Kinetics of Uranium Nitride Decomposition. *Inorganic chemistry*, 48(22):10635–10642, 2009.

[42] Frederic Poineau and Charles B Yeamans. X-ray absorption fine structure spectroscopic study of uranium nitrides. *Journal of Radioanalytical Nuclear Chemistry*, 292(3):989–994, 2012.

Based on the discussion from the last four chapters, the general conclusions are drawn about the various actinide systems investigated. These are given in the next chapter.

Chapter 7

General conclusions

In this study, we use first principle pseudopotential-based approach within the DFT and DFT+U based approaches to determine the total energy for various actinide systems. The fully converged total energy with respect to the kinetic energy cutoff and **k**-points sampling is used to determine the structural, mechanical, elastic and electronic properties. The following motivated the study: (i) the search for ordered alloys of Th-Ti systems, (ii) the understanding of Th-N based compounds and (iii) the effect of 5*f* electrons on the actinide systems.

Conclusions drawn from these studies are given at the end of each chapter focused on the results and discussion. This chapter presents the highlights of the study, which are divided are into two broad headings: (i) Thorium and its alloys, (ii) Other actinide compounds.

7.1 Thorium and its alloys

In this section the inclusion of the effective Hubbard U parameter for the accurate determination of the systems under investigation was found to be insignificant. This is due to the absence of an 5*f* electron in the thorium system.

This work is motivated by the usefulness of various compounds of Th and N in the generation of energy. Also, it validates the *ab initio* technique used in the study. Th_3N_4, Th_2N_3 and Th_2N_2NH systems were investigated to determine the structural, elastic, and electronic properties and the formation energy of these Th-N based compounds. The inclusion of SP and SOC results in no significant change in the calculated properties of these compounds. Therefore, the non-magnetic case was used in this investigation. We determined that Th-N based compounds are elastically stable, with a negative heat of formation. Th_3N_4 has the lowest

value of a_0, followed by Th_2N_3, then Th_2N_2NH. Th_3N_4 is the most energetically stable nitride of thorium considered. Using the valence charge density distribution, the bonding properties were accurately determined, which shows the presence of a predominantly ionic bonding character. Th_3N_4 and Th_2N_2NH are insulating, while Th_2N_3 is metallic. The insulating character of Th_2N_2NH, which is crystallographically similar to the metallic sesquinitride is attributed to the effect of the -(NH) group on the electronic structure. There is significant hybridization of the thorium 6*d* and 5*f* states with the nitrogen 2*p* in the Th-N based compounds

Next, the elemental, 50:50 and off 50:50 Th-Ti systems were investigated in order to determine the possibility of formation of an ordered alloy involving a ThTi system. This work is motivated by the usefulness of various alloys of Th and Ti. The structural stability was established using arguments based on elastic constants, phonon frequencies, electron localization function, valence charge density, band structure, density of states and heat of formation. Using the valence charge density and electron localization function plots, the bonding properties were accurately determined. The bonding character is described further from the electronic properties. From the MT-module, the elastic properties were determined. The calculation of elastic properties and phonon dispersions correctly determined the elastic stability and dynamic stability for $ThTi_3$ (in the Cr_3Si structure). $ThTi_3$ (in the Cr_3Si structure) was found to be metallic. Using arguments based on the calculated heat of formation, the investigated structure is predicted to be meta-stable.

7.2 Other actinide compounds

In this section the inclusion of the effective Hubbard *U* parameter for the accurate determination of the systems under investigation was found to be essential. This is due to the presence of a partially filled 5*f* orbital in the early actinide system.

The structural, mechanical and electronic properties of Pa, PaO and PaO_2 have been studied within the DFT and DFT+U approach. As far as the structural properties for Pa are concerned, the inclusion of the Hubbard *U* parameter is not relevant here, but has been found relevant to describe PaO and PaO_2 accurately. Pa, PaO and PaO_2 are elastically and dynamically stable. They are all metallic within the DFT approach. The inclusion of the effective Hubbard *U* parameter results in a band gap of 3.48 eV for the PaO_2 system using PBE (GGA). To accurately describe PaO and PaO_2, the inclusion of the effective Hubbard *U* parameter is essential.

Next, the ground state electronic, structural and mechanical properties of the early actinide mononitrides and dinitrides were studied using DFT+U. The calculated lattice parameters with the inclusion of the Hubbard U parameter agree well with available experimental data where that data exists. There is the exception of ThN, PuN and ThN_2 compounds where GGA gives acceptable results for the actinide mononitrides and dinitrides. In general, all the actinide nitrides studied are energetically favorable, and are elastically and mechanically stable, with the exception of ThN_2 that is unstable to isotropic pressure. Notably, UN_2 is thermodynamically unstable and has been speculated to stabilize under N-vacancy formation. This will be investigated in a future study. Comparison of the calculated and experimental magnetic properties of the actinide nitrides indicates that the GGA + U with and without SOC gives a good qualitative account of the properties compared with experiment, but not an accurate quantitative account. Looking at the valence charge density distribution of the actinide nitrides, the presence of ionic bonding is predominant with the dinitrides having higher covalent character compared to the mononitrides. Also, there is a consistent increase in the charge density distribution at the actinide sites for the actinide mononitrides and dinitrides with increasing atomic number. All the actinide nitrides considered are metallic in nature, with the exception of UN_2.

7.3 Conclusions

Firstly, the electronic and elastic properties of Th-N based alloys have been studied in detail. We established that $Th_2N_2(NH)$ is insulating, unlike the crystallographically equivalent Th_2N_3, which is metallic. Next, we have demonstrated that the formation of an ordered alloy of a Th-Ti based compound is plausible. This provided information on the electronic, elastic and mechanical properties of this ordered alloy. This has furnished more information on the bulk systems of these compounds.

Thereafter, we investigated the effect of the Hubbard U parameter on the Protactinium and its oxides, and various actinide nitrides. We find that to accurately describe these systems the inclusion of the U parameter is essential. Finally, a comparative study was presented on the early actinide mononitrides and dinitrides.

7.4 Future investigations

The various studies undertaken open up an avenue for further investigations. Future work involves searching for other candidate stoichiometry structure of various actinide elements and other alloying elements. The stability of the ordered alloys would be investigated using the method presented in chapter 4.

The investigation of various actinide systems will be carried out. This will involve studying how the Hubbard U parameter describes the various actinide carbides. An in-depth analysis of UN_2, looking at the effect of pressure, temperature on the stabilization of the UN_2 structure will be undertaken. Use of other available techniques such as dynamic mean field theory, GW approach, etc. to investigate the electronic and magnetic properties of actinide compounds that fails using the DFT+U approach will be considered.

References

[1] Kevin T Moore and Gerrit van der Laan. Nature of the $5f$ states in actinide metals. *Rev. Mod. Phys.*, 81:235–298, Feb 2009. doi: 10.1103/RevModPhys.81.235. URL http://link.aps.org/doi/10.1103/RevModPhys.81.235. [1]

[2] L Black, F Miserque, T Gouder, L Havela, J Rebizant, and F Wastin. Preparation and photoelectron spectroscopy study of UNx thin films. *Journal of Alloys and Compounds*, 315:36–41, 2001. [1]

[3] Yong Lu, Da-Fang Li, Bao-Tian Wang, Rong-Wu Li, and Ping Zhang. Electronic structures, mechanical and thermodynamic properties of ThN from first-principles calculations. *Journal of Nuclear Materials*, 408:136–141, January 2011. ISSN 00223115. doi: 10.1016/j.jnucmat.2010.11.007. URL http://linkinghub.elsevier.com/retrieve/pii/S0022311510006847. [1]

[4] D Sedmidubsky and P Nova. Calculation of enthalpies of formation of actinide nitrides. *Journal of Nuclear Materials*, 344:40–44, 2005. doi: 10.1016/j.jnucmat.2005.04.013. [1]

[5] K Kurosaki, J Adachi, M Uno, and S Yamanaka. Molecular dynamics studies of actinide nitrides. *Journal of Nuclear Materials*, 344(1-3):45–49, September 2005. ISSN 00223115. doi: 10.1016/j.jnucmat.2005.04.014. URL http://linkinghub.elsevier.com/retrieve/pii/S0022311505001972. [1]

[6] Raymond Atta-Fynn and Asok Ray. Density functional study of the actinide nitrides. *Physical Review B*, 76(11):1–12, September 2007. ISSN 1098-0121. doi: 10.1103/PhysRevB.76.115101. URL http://link.aps.org/doi/10.1103/PhysRevB.76.115101. [1, 4]

[7] G W Chinthaka Silva, Charles B Yeamans, Alfred P Sattelberger, Thomas Hartmann, Gary S

Cerefice, and Kenneth R Czerwinski. Reaction Sequence and Kinetics of Uranium Nitride Decomposition. *Inorganic chemistry*, 48(22):10635–10642, 2009. doi: 10.1021/ic901165j. [1]

[8] Hiroki Shibata, Tomohito Tsuru, Tsuyoshi Nishi, Masaru Hirata, and Yoshiyuki Kaji. Thermodynamic properties of neptunium nitride : a first principles study. *Journal of Nuclear Science and Technology*, 49(3):328–333, 2012. [1]

[9] Saurabh Bajaj, Cem Sevik, Tahir Cagin, Andres Garay, P E A Turchi, and Raymundo Arróyave. On the limitations of the DFT + U approach to energetics of actinides. *Computational Materials Science*, 59:48–56, 2012. ISSN 0927-0256. doi: 10.1016/j.commatsci.2012.02.023. URL http://dx.doi.org/10.1016/j.commatsci.2012.02.023. [1, 4]

[10] K O Obodo and N Chetty. GGA + U studies of the early actinide mononitrides and dinitrides. *Submitted to Journal of Nuclear Materials*, 2013. [1, 4, 99]

[11] H H Hill. *In Plutonium 1970 and Other Actinides*. AIME, New York, 1970. [1, 2]

[12] J J Katz, G T Seaborg, and Morss L R. *The Chemistry of the Actinide Elements*. Chapman and Hall, London, 1986. [1]

[13] D A Young. *Phase Diagrams of the Elements*. University of California Press, Berkeley, 1991. [1]

[14] L R Morss and J Fuger. *Transuranium Elements: A Half Century*. American Chemical Society, Washington, D.C., 1992. [1]

[15] L R Morss, N M Edelstein, J Fuger, and Katz J J. *The Chemistry of the Actinide and Transactinide Elements*, volume 1–5. Springer, New York, 2006. [1]

[16] L Soderholm, J J Joyce, M F Nicol, D K Shuh, and J G Tobin, editors. *Actinides-Basic Science, Applications, and Technology*, volume MRS Symposia Proceedings No. 802. Materials Research Society, Pittsburgh, 2004. [1]

[17] J L Sarrao, A J Schwartz, M R Antonio, P C Burns, R G Haire, and H Nitsche, editors. *Actinides 2005: Basic Science, Applications, and Technology*, volume MRS Symposia Proceedings No. 893. Materials Research Society, Pittsburgh, 2005. [1]

[18] J Bouchet, B Siberchicot, F Jollet, and A Pasturel. Equilibrium properties of δ -Pu : LDA + U calculations (LDA local density approximation). *Journal of physics. Condensed matter : an Institute of Physics journal*, 12:1723–1733, 2000. [2, 32]

[19] M B Brodsky. Magnetic properties of the actinide elements and their metallic compounds. *Reports on Progress in Physics*, 47(10):1547, 1978. [2]

[20] Vladimir I Anisimov, Jan Zaanen, and Ole K Andersen. Band theory and Mott insulators: Hubbard U instead of Stoner I. *Physical Review B*, 44(3):943–954, 1991. [2]

[21] A I Liechtenstein, V I Anisimov, and Zaanen J. Density-functional theory and strong interactions: Orbital ordering in Mott-Hubbard insulators. *Physical Review B*, 52(8):5467–5471, 1995. [2, 35, 36]

[22] V I Anisimov, F Aryasctiawan, and A I Lichtenstein. First-principles calculations of the electronic structure and spectra of strongly correlated systems : the LDA + U method. *Journal of Physics: Condensed Matter*, 767:767–808, 1997. [2]

[23] F Aryasetiawan, M Imada, A Georges, G Kotliar, S Biermann, and A I Lichtenstein. Frequency-dependent local interactions and low-energy effective models from electronic structure calculations. *Phys. Rev. B*, 70:195104, Nov 2004. doi: 10.1103/PhysRevB.70.195104. URL http://link.aps.org/doi/10.1103/PhysRevB.70.195104. [2, 34]

[24] Matteo Cococcioni and Stefano De Gironcoli. Linear response approach to the calculation of the effective interaction parameters in the LDA+ U method. *Physical Review B*, 71:1–16, 2005. doi: 10.1103/PhysRevB.71.035105. [2, 34]

[25] K O Obodo and N Chetty. *Ab initio studies* of Th_3N_4, Th_2N_3 and $Th_2N_2(NH)$. *To be submitted*, 2013. [3, 41]

[26] K O Obodo and N Chetty. A theoretical study of thorium titanium-based alloys. *Journal of Nuclear Materials*, 440:229–235, May 2013. ISSN 00223115. doi: 10.1016/j.jnucmat.2013.05.011. URL http://linkinghub.elsevier.com/retrieve/pii/S0022311513007186. [3, 51]

[27] Mott insulator. http://en.wikipedia.org/wiki/Mott_insulator, 2013. [Online; accessed 26-July-2013]. [4]

[28] Xiao-Dong Wen, Richard L Martin, Lindsay E Roy, Gustavo E Scuseria, Sven P Rudin, Enrique R Batista, Thomas M McCleskey, Brian L Scott, Eve Bauer, John J Joyce, and Tomasz Durakiewicz. Effect of spin-orbit coupling on the actinide dioxides AnO2 (An=Th, Pa, U, Np, Pu, and Am): a screened hybrid density functional study. *The Journal of chemical physics*, 137(15):154707, October 2012. ISSN 1089-7690. doi: 10.1063/1.4757615. URL http://www.ncbi.nlm.nih.gov/pubmed/23083184. [4]

[29] K O Obodo and N Chetty. First principles LDA + U and GGA + U study of protactinium and protactinium oxides: dependence on the effective U parameter. *Journal of Physics: Condensed Matter*, 25:145603(12), April 2013. ISSN 0953-8984. doi: 10.1088/0953-8984/25/14/145603. URL http://stacks.iop.org/0953-8984/25/i=14/a=145603?key=crossref.dd414eb18d75ba69b9406297d2590ff2. [4, 34, 71]

[30] B Dorado, M Freyss, and G Martin. GGA + U study of the incorporation of iodine in uranium dioxide. *The European Physical Journal B*, 69:203–209, 2009. doi: 10.1140/epjb/e2009-00145-0. [4]

[31] Y Yun, J Rusz, M Suzuki, and P M Oppeneer. First-principles investigation of higher oxides of uranium and neptunium : U_3O_8 and Np_2O_5. *Physical Review B*, 075109(September 2010):1–10, 2011. doi: 10.1103/PhysRevB.83.075109. [4]

[32] Boris Dorado, Philippe Garcia, Carine Davoisne, Mathieu Fraczkiewicz, Bertrand Pasquet, Michel Freyss, Carole Valot, Guido Baldinozzi, David Sim, and Marjorie Bertolus. First-principles calculation and experimental study of oxygen diffusion in uranium dioxide. *Physical Review Letters*, 83:035126(1–10), 2011. doi: 10.1103/PhysRevB.83.035126. [4]

[33] Boris Dorado, Bernard Amadon, Michel Freyss, and Marjorie Bertolus. DFT + U calculations of the ground state and metastable states of uranium dioxide. *Physical Review B*, 235125(79):1–8, 2009. doi: 10.1103/PhysRevB.79.235125. [4, 32]

[34] Hiroaki Tagawa. Phase Relations and Thermodynamic Properties of the Uranium-Nitrogen system. *Journal of Nuclear Materials*, 51:78–89, 1974. [4]

[35] Daniel Joubert. *African School on Electronic Structure Methods: Density Functional Theory Basics*, pages 3–45. July 2008. lecture notes. [7]

[36] M Born and J R Oppenheimer. Zur Quantentheorie der Molekeln. *Annalen Physik (Leipzig)*, 84 (457), 1927. [8]

[37] D R Hartree. The wave mechanics of an atom with non-Coulombic central I, II, III,. *Proc.Cambridge Phil.Soc*, 24:89,111,426, 1928. [9]

[38] V Fock. *Z.Phys*, 65:209, 1930. [9]

[39] J. C. Slater. Note on Hartree's Method. *Physical*, 35:210, 1930. [9]

[40] Richard M Martin. *Electronic Structure: Basic Theory and Practical Methods*. Cambridge University Press, New York, 2004. [9, 10, 11, 13, 14, 16, 22, 23, 26, 30, 31]

[41] P Hohenberg and W Kohn. Inhomogeneous Electron Gas. *Physical Review*, 136(3B):864, 1964. [11]

[42] W Kohn and L J Sham. Self-Consistent Equations Including Exchange and Correlation Effects. *Physical Review B*, 140(4A):A1133, 1965. [13, 15]

[43] Paolo Giannozzi. *Metodi Numerici in Struttura Elettronica*. 2010. lecture notes. [14]

[44] D M Ceperley and B J Alder. Ground State of the Electron Gas by a Stochastic Method f. *Physical Review Letters*, 45(7):566–569, 1980. [15]

[45] J. P. Perdew and Alex Zunger. Self-interaction correction to density-functional approximations for many-electron systems. *Physical Review B*, 23(10):5048–5079, 1981. [15]

[46] J F Dobson, G Vignale, and M P Das. *Electronic density functional theory: Recent progress and new directions, Eds.* Plenum Press, New York, 1997. [16]

[47] John P Perdew, Kieron Burke, and Matthias Ernzerhof. Generalized Gradient Approximation Made Simple. *Physical Review Letters*, 77(18):3865–3868, 1996. [17]

[48] A D Becke. Becke - 1988 - Density-functional exchange-energy approximation with correct asymptotic behavior.pdf. *Physical Review A*, 38(6):3098–3100, 1988. [17]

[49] John P Perdew and Yue Wang. Accurate and simple analytic representation of the electron-gas correlation energy.pdf. *Physical Review B*, 45(23), 1992. [17]

[50] John P. Perdew, Adrienn Ruzsinszky, Gabor I. Csonka, Oleg A. Vydrov, Gustavo E. Scuseria, Lucian A. Constantin, Xiaolan Zhou, and Kieron Burke. Restoring the Density-Gradient Expansion for Exchange in Solids and Surfaces. *Physical Review Letters*, 100(136406):1–4, 2008. doi: 10.1103/PhysRevLett.100.136406. [17]

[51] J Korringa. On the calculation of the energy of a bloch wave in a metal. *Physica*, 13(6¢7): 392 – 400, 1947. ISSN 0031-8914. doi: 10.1016/0031-8914(47)90013-X. URL http://www.sciencedirect.com/science/article/pii/003189144790013X. [17]

[52] W. Kohn and N. Rostoker. Solution of the schrödinger equation in periodic lattices with an application to metallic lithium. *Phys. Rev.*, 94:1111–1120, Jun 1954. doi: 10.1103/PhysRev.94.1111. URL http://link.aps.org/doi/10.1103/PhysRev.94.1111. [17]

[53] M C Payne, M P Teter, D C Allan, T A Arias, and J D Joannopoulos. Iterative minimization techniques for ab initio total-energy molecular dynamics and conjugate gradients calculations :. *Reviews of Modern Physics*, 64(4):1045–1097, 1992. [17, 19]

[54] Richard M Martin. *Electronic Structure: Basic Theory and Practical Methods*, chapter 9, page 173. Cambridge University Press, 2004. [18]

[55] H M Krutter. Energy bands in copper. *Physical Review*, 48:664, 1935. [20]

[56] F Hermann. Theoretical investigation of the electronic energy band structure of solids. *Review of Modern Physics*, 102:102, 1940. [20]

[57] James C Phillips. Energy-Band Interpolation Scheme Based on a Pseudopotential. *Physical Review*, 112(3):685, 1958. [20]

[58] M L Cohen and V Heine. *The fitting of pseudopotentials to experimental data and their subsequent application "," in Solid State Physics*, volume 24, page 37. Academic Press, New York, 1970. [20]

[59] M. T. Yin and Marvin L. Cohen. Theory of static structural properties, crystal stability, and phase transformations Applications to Si and Ge. *Physical Review B*, 26(10), 1982. [20, 32]

[60] Conyers Herring. A new method for calculating wave functions in crystals. *Phys. Rev.*, 57:1169–1177, Jun 1940. doi: 10.1103/PhysRev.57.1169. URL http://link.aps.org/doi/10.1103/PhysRev.57.1169. [20]

[61] Stewart Clark. Pseudopotentials, August 2008. URL http://portellen.phycmt.dur.ac.uk/sjc/thesis_dlg/node21.html. [Online; accessed 25-July-2013]. [20]

[62] P. E. Blochl. Unknown - Unknown - Blöchl - 994 - Projector augmented-wave method. *Physical Review B*, 50(24):17953–17979, 1994. [22]

[63] G Kresse and D Joubert. From ultrasoft pseudopotentials to the projector augmented-wave method. *Physical Review B*, 59(3):1758 – 1775, 1999. [22]

[64] Tackett A R Holzwarth N A W, Matthews G E and Dunning R B. Comparision of the projector augumented-wave, pseudopotential transferability. *Physical Review B*, 55:2005–2017, 1997. [22]

[65] David Vanderbilt. Soft self-consistent pseudopotentials in a generalized eigenvalue formalism. *Physical Review B*, 41(11):7892–7895, 1990. [22]

[66] D R Hamann, M Schluter, and C Chiang. Norm-Conserving Pseudopotentials. *Physical Review Letters*, 43(20):1494–1497, 1979. [22]

[67] G Kresse and J Furthmuller. Efficient iterative schemes for ab initio total-energy calculations using a plane-wave basis set . *Physical Review B*, 54(16), 1996. [24]

[68] X Gonze, B Amadon, P M Anglade, J M Beuken, F Bottin, P Boulanger, F Bruneval, D Caliste, R Caracas, M Cote, T Deutsch, L Genovese, Ph Ghosez, M Giantomassi, S Goedecker, D R Hamann, P Hermet, F Jollet, G Jomard, S Leroux, M Mancini, S Mazevet, M J T Oliveira, G Onida, Y Pouillon, T Rangel, G M Rignanese, D Sangalli, R Shaltaf, M Torrent, M J Verstraete, G Zerah, and J W Zwanziger. Abinit: first-principles approach to material and nanosystem properties. *Computer Physics Communications*, 180(12):2582–2615, 2009. URL www.scopus.com. Cited By (since 1996): 320. [24]

[69] Paolo Giannozzi, Stefano Baroni, Nicola Bonini, Matteo Calandra, Roberto Car, Carlo Cavazzoni, Davide Ceresoli, Guido L Chiarotti, Matteo Cococcioni, Ismaila Dabo, Andrea Dal Corso,

Stefano De Gironcoli, Stefano Fabris, Guido Fratesi, Ralph Gebauer, Uwe Gerstmann, Christos Gougoussis, Anton Kokalj, Michele Lazzeri, Layla Martin-samos, Nicola Marzari, Francesco Mauri, Riccardo Mazzarello, Stefano Paolini, Alfredo Pasquarello, Lorenzo Paulatto, Carlo Sbraccia, Alexander Smogunov, Paolo Umari, and Renata M Wentzcovitch. Q UANTUM ESPRESSO : a modular and open-source software project for quantum simulations of materials. *Journal of physics. Condensed matter*, 21(395502):1–19, 2009. doi: 10.1088/0953-8984/21/39/395502. [24]

[70] Brillouin zone integration. http://www.physics.metu.edu.tr/~hande/teaching/741-lectures/lecture-09.pdf. Online; accessed 28-January-2013. [24]

[71] Lehmann G and Taut M. On the numerical calculation of the density of states and related properties. *Physica Status Solidi B*, 54(2):469–477, 1972. [24]

[72] Peter E. Blöchl, O. Jepsen, and O. K. Andersen. Improved tetrahedron method for Brillouin-zine integrations.pdf. *Physical Review B*, 48(23):16223–16234, 1994. [24]

[73] C Pickard and M Payne. Extrapolative approaches to Brillouin-zone integration. *Physical Review B*, 59(7):4685–4693, February 1999. ISSN 0163-1829. doi: 10.1103/PhysRevB.59.4685. URL http://link.aps.org/doi/10.1103/PhysRevB.59.4685. [24]

[74] A Baldereschi. Mean-Value Point in the Brillouin Zone. *Physical Review*, 7(12):5212–5215, 1973. [24]

[75] D J Chadi and M L Cohen. Special Points in the Brillouin Zone. *Physical Review B*, 8(12):5747, 1973. [24]

[76] Hendrik J Monkhorst and James D Pack. Special points for Brillouin-zone integrations. *Physical Review B*, 13(12):5188, 1976. [24, 25]

[77] James D Pack and Hendrik J Monkhorst. ”Special points for Brillouin-zone integrations”a reply. *Physical Review B*, 16(4):1748–1749, 1977. [24]

[78] Materials Design Inc. *MEDEA Users Guide*. Materials Design Inc., medea 2.4 edition, 2008. [25, 28, 32]

[79] H Hellmann. Einfuhrung in die Quantumchemie. Franz Duetsche Leipzig, 1939. [26]

[80] R P Feynmann. Forces in molecules. *Physical Review*, 56(360), 1939. [26]

[81] D F Shanno. *Math. Oper. Res.*, 3(244), 1978. [27]

[82] Neil W Ashcroft and N David Mermin. *Solid State Physics*. Brooks/Cole Cengage Learning, 1976. [27]

[83] J F Nye. *Physical Properties of Crystals*. Clarendon: Oxford, 1957. [28]

[84] Orson L Anderson. A SIMPLIFIED METHOD FOR CALCULATING THE DEBYE TEPERATURE FROM ELASTIC CONSTANTS. *Journal of Physics and Chemistry of Solids*, 24:909–917, 1963. [29, 30]

[85] R Hill. The Elastic Behaviour of a Crystalline Aggregate. *Proceedings of the Royal Society A*, 65 (5):349–354, 1952. [29]

[86] R Pick, M H Cohen, and R M Martin. Miscroscopic theory of force constants in the adiabatic approximation. *Physical Review B*, 1:910–920, 1970. [30]

[87] M Born and K Huang. *Dynamical Theory of Crystal Lattices*. Oxford University Press, Oxford, 1954. [31]

[88] Stefano Baroni, Stefano De Gironcoli, Andrea Dal Corso, and Paolo Giannozzi. Phonons and related crystal properties from density-functional perturbation theory. *Reviews of Modern Physics*, 73(2):515–662, 2001. [32]

[89] A Rahman. Correlations in the Motion of Atoms in Liquid Argon. *Physical Review*, 136(2A): A405–A411, 1964. [32]

[90] K Terakura, T Oguchi, A R Williams, and J Kubler. Band theory of insulating transition-metal monoxides: band-structure calculations. *Physical Review B*, 30(8):4734–4747, 1984. [32]

[91] T Oguchi, K Terakura, and A R Williams. Band theory of the magnetic interaction in MnO, MnS, and NiO. *Physical Review B*, 28(6443):6443, 1983. [32]

[92] Matteo Cococcioni. *A LDA + U study of selected iron compounds*. Number October. 2002. [33, 34, 37, 38]

[93] Alexander Lichtenstein, David Singh, Ole Andersen, Matteo Cococcioni, Jörg Bünemann, Eva Pavarini, Erik Koch, Robert Eder, Olle Gunnarsson, Rudolf Zeller, Frithjof Anders, Ralf Bulla, Mark Jarrell, Andrey Mishchenko, David DiVincenzo, and Norbert Schuch. *Correlated Electrons : From Models to Materials*. Forschungszentrum Jülich GmbH Institute for Advanced Simulation, Jülich, 2 edition, 2012. ISBN 9783893367962. [33, 34, 35, 37, 38, 39]

[94] Michel Côté. Introduction to DFT + U. Technical report, Universitye de Montreal, Montreal, 2008. URL pitp.physics.ubc.ca/.../pitpcifar_sherbrooke2008_dft_u_cote. [33, 35]

[95] V I Anisimov and O Gunnarsson. Density-functional calculation of effective Coulomb interactions in metals. *Physical Review B*, 43(10):7570–7574, 1991. [34, 37]

[96] G W Chinthaka Silva, Philippe F Weck, Eunja Kim, Charles B Yeamans, Gary S Cerefice, Alfred P Sattelberger, and Kenneth R Czerwinski. Crystal and Electronic Structures of Neptunium Nitrides Synthesized Using a Fluoride Route. *Journal of The American Chemical Society*, 134:3111–3119, 2012. [34]

[97] O Gunnarsson, O K Andersen, O Jepsen, and J Zaanen. Density-functional calculation of the parameters in the Anderson model: Application to Mn in CdTe. *Physical Review B*, 39(3):1708, 1989. [37]

[98] M T Czyzyk and A Sawatzky. Local-density functional and on-site correlations: The electronic structure of La2Cu04 and LaCuO3. *Physical Review B*, 49(20):14211–14228, 1994. [37]

[99] S L Dudarev, G A Botton, S Y Savrasov, C J Humphreys, and A P Sutton. Electron-energy-loss spectra and the structural stability of nickel oxide: An LSDA + U study. *Physical Review B*, 57 (3):1505–1509, 1998. [38]